T.R.
GEBZE TECHNICAL UNIVERSITY
GRADUATE SCHOOL OF NATURAL AND APPLIED SCIENCES

PHYSICAL BASED MODELING OF THE ELECTROCHEMICAL IMPEDANCE OF LITHIUM-ION BATTERIES

ONGUN BORA SABAN
A THESIS SUBMITTED FOR THE DEGREE OF
MASTER OF SCIENCE
DEPARTMENT OF MECHANICAL ENGINEERING

GEBZE
2020

T.R.

GEBZE TECHNICAL UNIVERSITY

GRADUATE SCHOOL OF NATURAL AND APPLIED SCIENCES

PHYSICAL BASED MODELING OF THE ELECTROCHEMICAL IMPEDANCE OF LITHIUM-ION BATTERIES

ONGUN BORA SABAN

A THESIS SUBMITTED FOR THE DEGREE OF

MASTER OF SCIENCE

DEPARTMENT OF MECHANICAL ENGINEERING

THESIS ADVISOR

PROF. MEHMET ALI ARSLAN

THESIS CO-ADVISOR

ASSOC. PROF. MUSTAFA FAZIL SERINCAN

GEBZE

2020

T.C.
GEBZE TEKNİK ÜNİVERSİTESİ
FEN BİLİMLERİ ENSTİTÜSÜ

LİTYUM-İYON BATARYALARIN ELEKTROKİMYASAL EMPEDANSININ FİZİKSEL MODELİ

ONGUN BORA SABAN
YÜKSEK LİSANS TEZİ
MAKİNE MÜHENDİSLİĞİ ANABİLİM DALI

DANIŞMANI
PROF. DR. MEHMET ALİ ARSLAN
EŞ DANIŞMANI
DOÇ. DR. MUSTAFA FAZIL SERİNCAN

GEBZE
2020

GEBZE TEKNİK ÜNİVERSİTESİ	YÜKSEK LİSANS JÜRİ ONAY FORMU

GTÜ Fen Bilimleri Enstitüsü Yönetim Kurulu'nun 24/07/2020 tarih ve 2020/36 sayılı kararıyla oluşturulan jüri tarafından 07/08/2020 tarihinde tez savunma sınavı yapılan Ongun Bora SABAN'ın tez çalışması Makine Mühendisliği Anabilim Dalında YÜKSEK LİSANS tezi olarak kabul edilmiştir.

JÜRİ

ÜYE

(TEZ DANIŞMANI) : PROF. DR. MEHMET ALİ ARSLAN

ÜYE : PROF. DR. İLYAS KANDEMİR

ÜYE : PROF. DR. MUSTAFA SABRİ GÖK

ONAY

Gebze Teknik Üniversitesi Fen Bilimleri Enstitüsü Yönetim Kurulu'nun
…..…/…..…/..…..… tarih ve ……/…….. sayılı kararı.

İMZA/MÜHÜR

SUMMARY

In parallel with the technological developments and increased world population demand on energy had significantly increased. Although, this demand was supplied by fossil fuels for many years, new researches and improvements about high efficiency renewable energy sources had been studied due to decrease the carbon footprint and as well as to overcome to effects of global warming. Electrochemical energy storage systems such as fuel cells and batteries have considered as the promising solution than the conventional energy systems.

It is critical issue to analyze the dynamic behavior, charge transfer kinetics and characterize the system response of an electrochemical system for making technological developments on the materials and components. For this reason, many studies on system characterization with different methods held in many years. In order to characterize the behavior of an electrochemical system accurately, time-domain and frequency-domain analyzes have been studied by different research groups. Hence, electrochemical impedance spectroscopy has been used as one of the most considered application for characterizing the response of a system.

Comparing to other modeling methods like equivalent circuit modeling, a novel method had been represented based on porous electrode theory on a lithium-ion battery system in this study. In order to obtain comprehensive investigation of the physico-chemical properties of discharge mechanism and impedance behavior a lithium-ion battery has modeled, also the temperature and current flow rate dependency on charge transfer kinetics has been demonstrated. Furthermore, the sensitivity analysis of the parameters and the optimization of the system response had been practiced in order to increase the model accuracy.

As a result of this study, a new system model methodology and three-domain electrode modeling approach had been developed.

Key Words: Energy, Renewable Energy Systems, Electrochemical Impedance Spectroscopy, Battery Characterization, System Dynamics, CFD Modeling.

ÖZET

Teknolojik gelişmelerin ve dünya nüfusunun artmasıyla birlikte enerji talebi de büyük ölçüde artmıştır. Bu talep uzun yıllardır fosil yakıtlar tarafından sağlansa da, karbon ayak izinin azaltılması ve küresel ısınmanın etkilerinin üstesinden gelmek için yüksek verimli yenilenebilir enerji kaynaklarıyla ilgili yeni araştırmalar ve iyileştirmeler yapıldı. Yakıt pilleri ve bataryalar gibi elektrokimyasal enerji depolama sistemleri, geleneksel enerji sistemlerinden daha umut verici bir çözüm olarak kabul edilmektedir.

Malzemeler ve bileşenler üzerinde teknolojik gelişmeler yapmak için bir elektrokimyasal sistemin dinamik davranışını ve yüklü parçacık aktarım kinetiğini analiz etmek, aynı zamanda sistem cevabını karakterize etmek kritik bir konudur. Bu nedenle, yıllarca farklı yöntemlerle sistem karakterizasyonu üzerine birçok çalışma yapılmıştır. Bir elektrokimyasal sistemin davranışını doğru bir şekilde karakterize etmek için farklı araştırma grupları tarafından zaman ve frekans alan temelli çalışmalar yürütülmüştür. Bu nedenle, bir sistemin yanıtını detaylı bir şekilde karakterize etmek için en çok üzerinde durulan uygulamalardan biri olarak elektrokimyasal empedans spektroskopisi kullanılmıştır.

Bu çalışmada, bataryaların eşdeğer devre modeli gibi diğer modelleme yöntemlerinin haricinde, gözenekli elektrot teorisi temelli yeni bir yöntem tanıtılmıştır. Deşarj mekanizmasının fiziko-kimyasal özellikleri ve empedans davranışının kapsamlı bir şekilde araştırılması için bir lityum-iyon batarya modellenmiştir, ayrıca şarj transfer kinetiklerine sıcaklık ve akım debisinin etkileri incelenmiştir. Bunların yanında parametrelerin hassasiyet analizi ve sistem cevabının optimizasyonu ile model becerileri arttırılmıştır.

Bu çalışmanın bir sonucu olarak yeni bir model metodolojisi ve üç-alanlı elektrot model yaklaşımı geliştirilmiştir.

Anahtar Kelimeler: Enerji, Yenilenebilir Enerji Sistemleri, Elektrokimyasal Empedans Spektroskopisi, Batarya Karakterizasyonu, Sistem Dinamiği, HAD Model.

ACKNOWLEDGEMENTS

This thesis supported by the Scientific and Technological Research Council of Turkey (TÜBİTAK) projects with the project numbers of #117M222 and #114M774.

I wish to express my sincere gratitude to my advisor Prof. Mehmet Ali ARSLAN and co-advisor Assoc. Prof. Mustafa Fazıl SERİNCAN for their supports in scope of this study. His knowledge has broadened my mind during my studies. Their encouragements were motivating, and their support became the reason of my willing to learn and study more in the pursuit of excellence during this master's thesis.

I would also express my sincere thanks to Assoc. Prof. Catia ARBIZZANI and Assoc. Prof. Francesca SOAVI working at the University of Bologna, who helped me to learn the working principles of electrochemical measurement systems and experimental setups.

Also, I am extremely thankful to Eda GÜZEL who helped the experiments directly and indirectly during the study.

I express my deepest gratitude to my family for all their support and leading at each stage of my life.

TABLE of CONTENTS

LIST of ABBREVATIONS and ACRONYMS

Abbreviations and Acronyms		**Explanations**
ESS	:	Energy Storage System
ECS	:	Energy Conversion System
MCFC	:	Molten Carbonate Fuel Cell
SOFC	:	Solid Oxide Fuel Cell
PEMFC	:	Proton Exchange Membrane Fuel Cell
DMFC	:	Direct Methanol Fuel Cell
AFC	:	Alkaline Fuel Cell
PAFC	:	Phosphoric Acid Fuel Cell
LIB	:	Lithium-Ion Battery
SoC	:	State of Charge
ECM	:	Equivalent Circuit Modeling
OCV	:	Open Circuit Voltage
R	:	Resistor
C	:	Capacitor
L	:	Inductor
Z	:	Impedance
Z_r	:	Real Part of Impedance
Z_j	:	Imaginary Part of Impedance
E	:	Electric Potential
I	:	Current
ΔS	:	Entropy Change
Q	:	Cell Capacity
ΔG	:	Free Energy Change
P	:	Power
ΔH	:	Enthalpy Change
EDL	:	Electrical Double Layer
DLC	:	Double layer capacitance
EIS	:	Electrochemical Impedance Spectroscopy

IUPAC	:	International Union of Pure and Applied Chemistry
ψ	:	Phase angle
ω	:	Frequency
Z_w	:	Warburg Impedance
CPE	:	Constant Phase Element
ξ	:	Warburg Coefficient
Hz	:	Hertz
H	:	Henry
F	:	Farad
NMC	:	Nickel Manganese Cobalt Oxide
M	:	Molar
SoH	:	State of Health
C-rate	:	Current flow rate
CC-CV	:	Constant Current-Constant Voltage
Ah	:	Ampere-Hours
SEI	:	Solid-Electrolyte Interface
GITT	:	Galvanostatic Intermittent Titration Technique
ODE	:	Ordinary Differential Equation
RMS	:	Root-Mean-Square
SNOPT	:	Sparse Nonlinear Optimization
1-D	:	One Dimensional
CFD	:	Computational Fluid Dynamics
NMC	:	Lithium Nickel Manganese Cobalt Oxide
LTO	:	Lithium Titanate
NCA	:	Lithium Nickel Cobalt Aluminum Oxide
FLW	:	Finite-length Warburg
FSW	:	Finite-space Warburg
P2D	:	Pseudo two-dimensional
MSMD	:	Multi-scale Multi-domain
DFN	:	Doyle-Fuller-Newman

LIST of FIGURES

LIST of TABLES

1. INTRODUCTION

One of the main research topics in today's world is how the energy demand could be fulfilled. In order to supply energy for the expanding population or the big industries such as space, automotive and defense, fossil fuels –which are the non-renewable energy sources- for instance petroleum, coal and natural gas are the most common energy supplies from the beginning of the industrial revolution. According to a statistical report [1] published by British Petrol in 2019, the growth in energy consumption is 40% in the last 30 years. Moreover, the rapid growth on energy use (2.9%) seen in 2018 since 2010. Today, although 82% of energy demand is supplied by burning the fossil fuels, the harms on environment and human health challenging the governments and industries to use the renewable energy sources such as wind, solar, geothermal, hydroelectric, biofuel and electrochemical energy. In the figure [2] given below, global energy consumption (1000 TWh) per year is indicated for from 1965 to 2017.

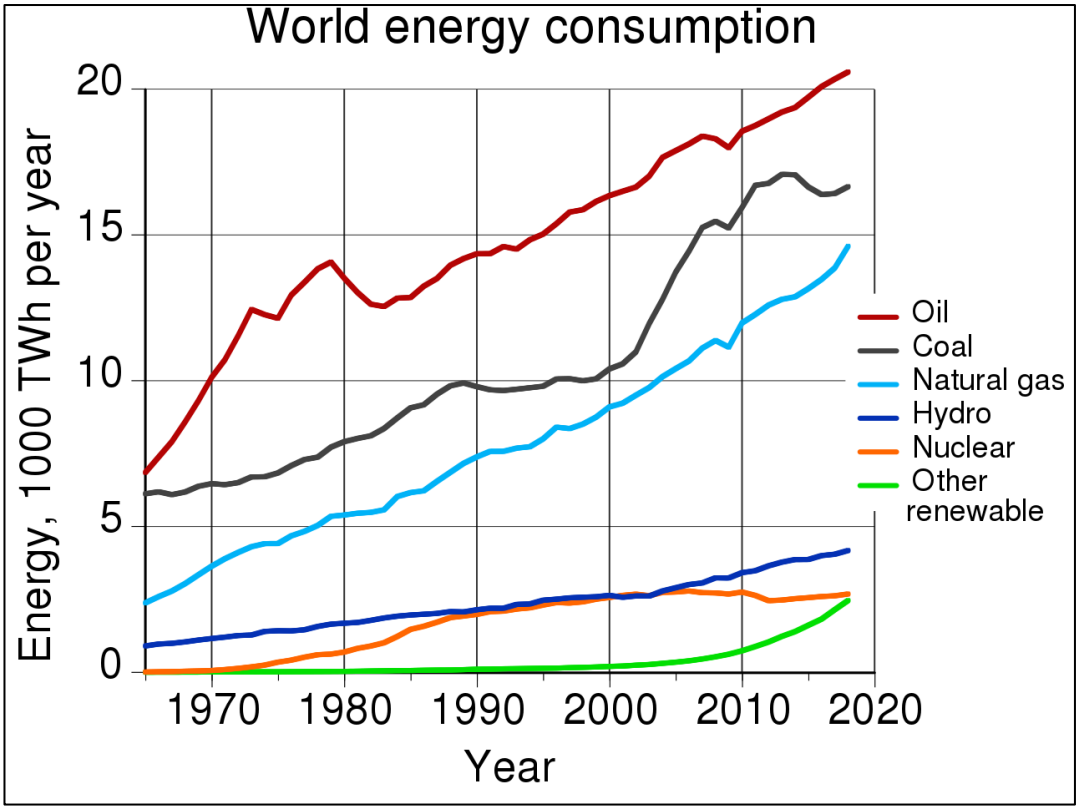

Figure 1.1. World energy consumption per year.

According to Badwal et al. [3] clean energy generation is mostly limited with national borders. Furthermore, this limitation has been a challenging feature for energy storage and large power generation. On the other hand, the increase of the energy requirements and demand of hybrid energy solutions have been pointed out the electrochemical energy conversion systems in order to meet the needs such as low cost, high efficiency and long-life cycle. Batteries and fuel cell systems are the most promising energy storage systems (ESS) due to their power and energy density rates [4].

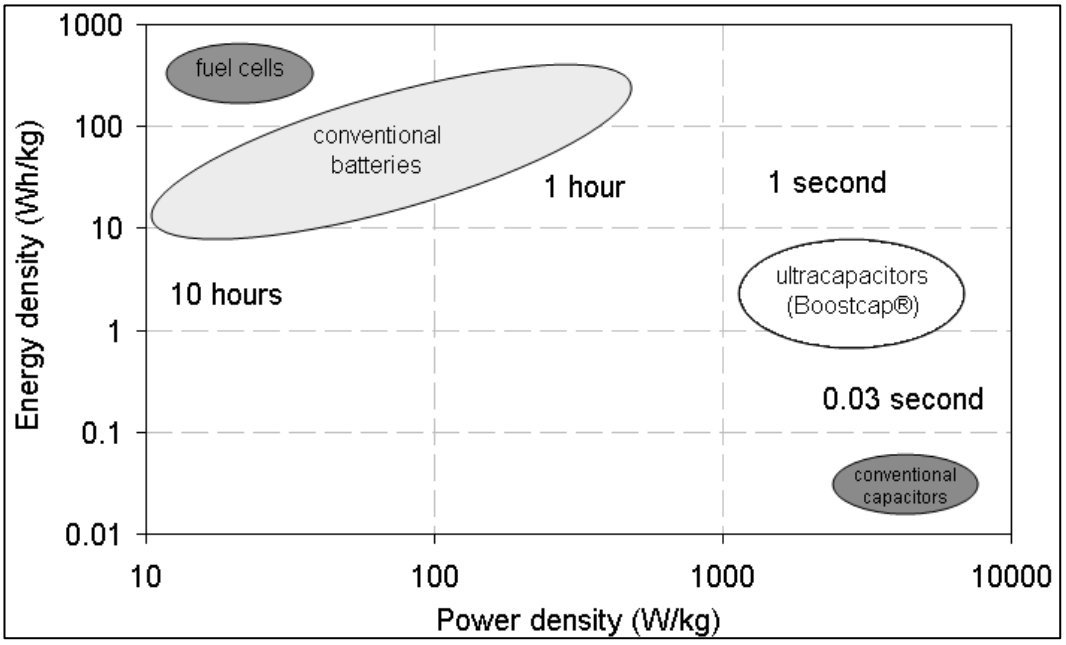

Figure 1.2. Energy density vs. power density comparison of ESS devices.

1.1. Fuel Cells

Fuel cells are basically responsible for converting electrochemical energy into electrical energy as long as fuel and oxidant are supplied. William Grove who has demonstrated the first fuel cell (also called gaseous voltaic battery), burnt hydrogen with a simple reaction and reversed the electrolysis by replacing power supply with an ammeter in an experiment and recombining the hydrogen and oxidant in 1839.

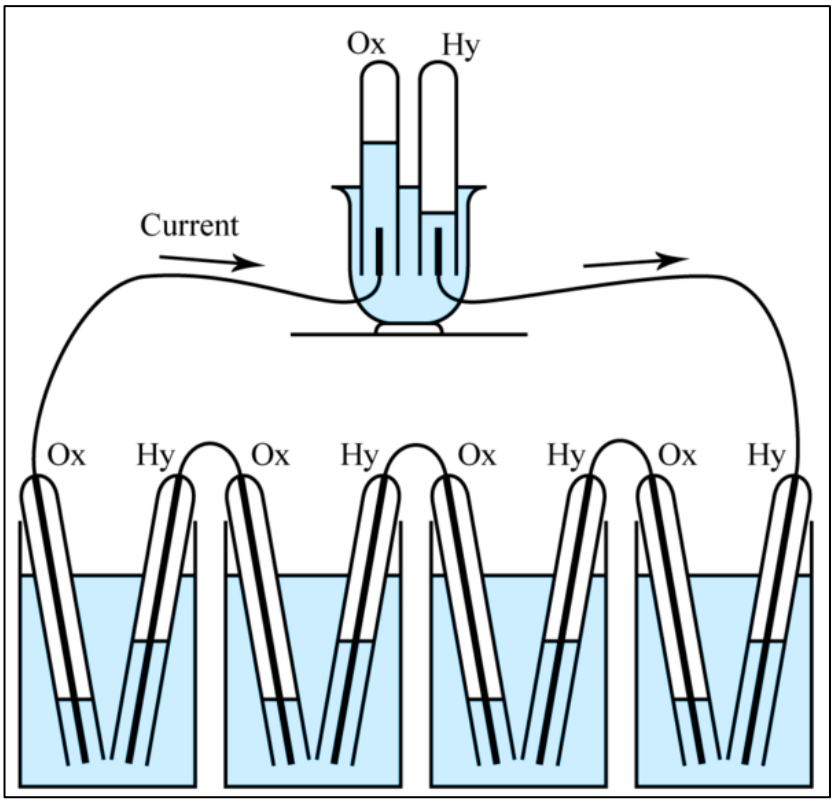

Figure 1.3. A schematic illustration of the gaseous voltaic battery.

The working principle of a fuel cell can be explained briefly. The ionization of the hydrogen gas while provides to release electrons (energy) at the anode of the cell and hydrogen ions (protons) pass through the electrolyte, on the other hand, hydrogen ions are burnt in the cathode by oxygen. As a result of those reactions, unused gases or formed water are released outside of the system and electrical energy is generated continuously as long as fuel is supplied. The schematic diagram of a fuel cell is represented in the Fig. 1.4. As described above, the reactions taking place at the anode and cathode of a fuel cell can simply formulated as the formulas given below.

At the anode:

$$2H_2 \xrightarrow{ionization} 4H^+ + 4e^- \tag{1.1}$$

At the cathode:

$$O_2 + 4e^- + 4H^+ \xrightarrow{oxidation} 2H_2O \tag{1.2}$$

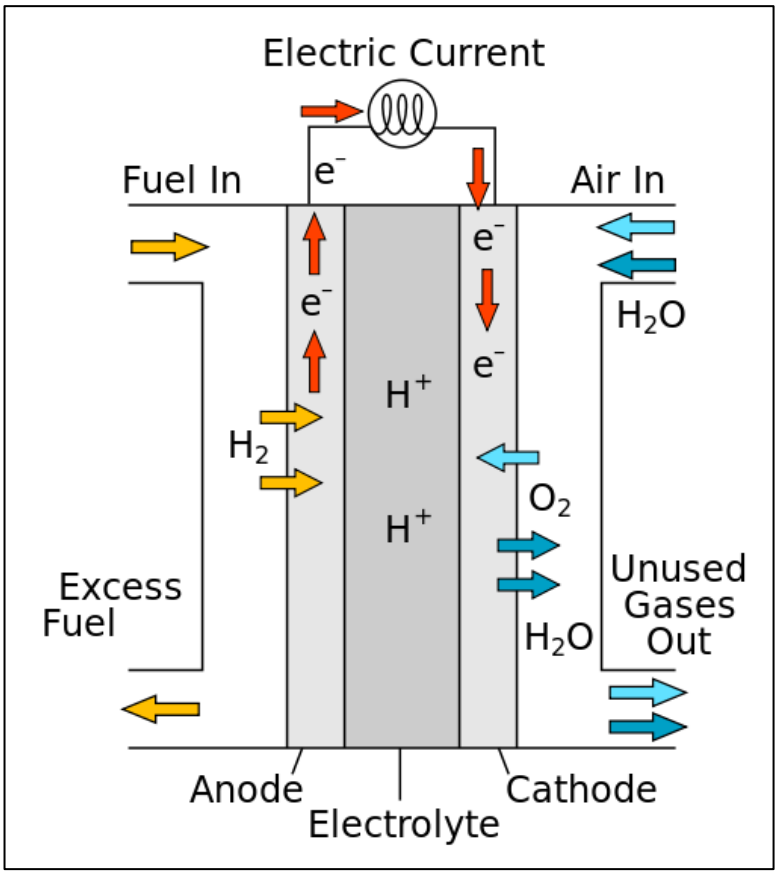

Figure 1.4. A schematic diagram of a fuel cell.

Although energy density of fuel cells is high and not limited by Carnot efficiency, the voltage obtained from a fuel cell is about 0.7 V, which means, in order to generate more power fuel cells, have to be connected in series as a stack. Furthermore, because of the fact that slow reaction rates and low currents and power are occurring in these systems, designing and optimizing the cells are crucial. Thus, porous electrodes are used in fuel cell systems and bipolar plates are developed so the fuel and oxidant can flow over the face of the electrodes. There are six main types of fuel cells:

Due to its low working temperature and high-power generation density, the proton exchange membrane fuel cells (PEMFC) have the most consideration on themselves since they have been first used in Gemini spaceships [5,6]. As a result of the fact that a polymer membrane called as Nafion used in these systems, operating temperature is about 80 ℃ and the efficiency is about 40% according to Oosterkamp [7].

Although, PEM fuel cells are commonly operating with hydrogen, methanol fuels in liquid form can be used for the long-term and low-power steady electricity generation and are called as direct methanol fuel cells (DMFC).

Another type is alkaline fuel cells (AFC), which are operating 60 ℃ to 240 ℃. They were used in Apollo and Shuttle Orbiter crafts to provide electricity.

The phosphoric acid fuel cells (PAFC) are the first commercialized fuel cell type and are used for numerous electrochemical power plants up to 4 MW electricity generation. The operating temperature is between 180 and 200 ℃. Even though they are complex and big sized systems, easy to maintain.

One of the main types is solid oxide fuel cells (SOFC) which generates electricity with the operation temperature up to 1000 ℃. As a result of high temperature reactions these kind of systems needs more parts such as coolers or pre-heaters to achieve desired efficiency. In addition, it is difficult to manufacture the ceramic materials used in these systems. Despite of the fact that operating temperature of SOFC is very high, the electrolyte material (zirconium dioxide) always remains in solid state.

There is a type of fuel cell that uses carbon dioxide in the air to generate electricity which is called as molten carbonate fuel cell (MCFC). Besides, its operation temperature (~700℃) is less than SOFCs and it can directly use hydrogen and carbon monoxide as fuel.

Today, while the most challenging factor for fuel cells is the cost there are many advantages such as efficiency, simplicity, silence and low emission values. For an example, due to fuel cells have higher energy density than batteries they can be used in portable electronics or they can be used in the distributed environmentally friendly power generation by considering their efficiency and silence [8].

1.2. Batteries

Batteries are the one of the main research fields on electrochemical power sources due to their high energy rate and stability. The first electrochemical battery was demonstrated by Alessandro Volta in the beginning of 19^{th} century. After the second half of 19^{th} century, invention of high current batteries for electrical motors, invention of the incandescent lamp and introduction of radio receivers and after the last quarter of 20^{th} century developments in information technology, automobile and

space industry have made batteries one of the widely used energy conversion systems today [9]. A battery is a group of electrochemical cells connected serials or parallel arrangement. As demonstrated in the Figure 1.5, a traditional battery cell contains two electrodes with different electrochemical compositions separated by an electrolyte solution.

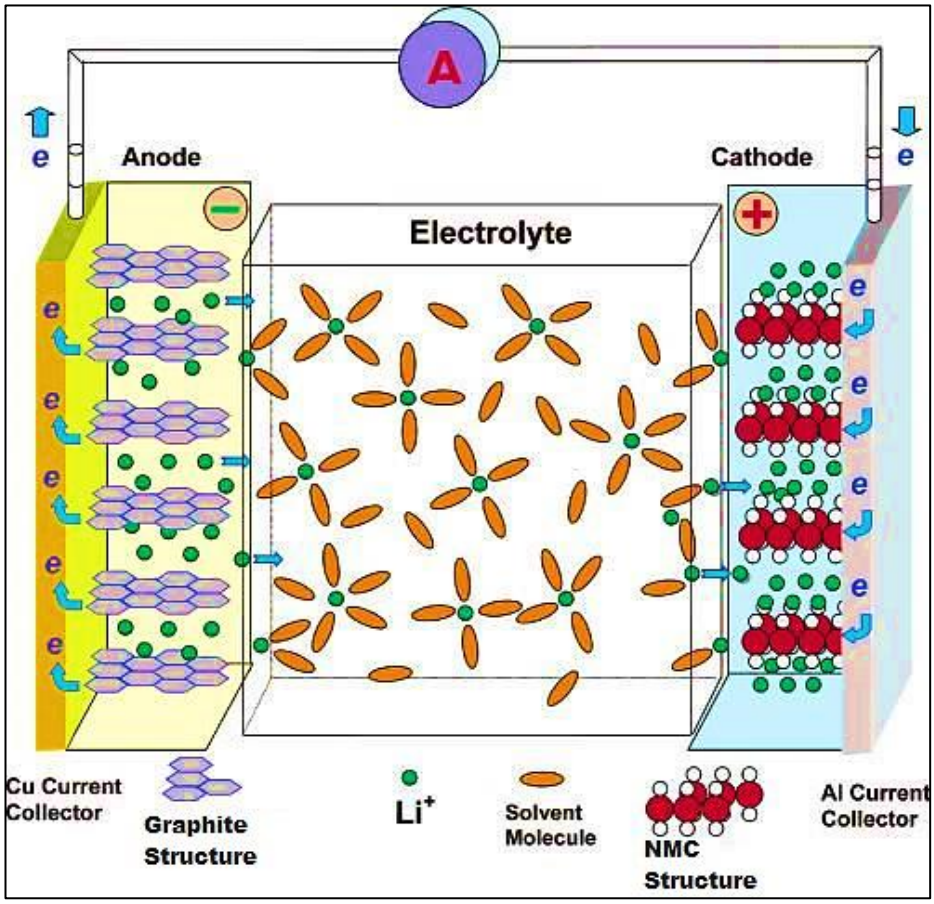

Figure 1.5. A schematic of a battery cell.

Batteries can be arranged into various classifications by considering the chemical composition, size and use cases and yet, there are two principle kinds of batteries, which are Primary batteries (throwaway batteries) and secondary batteries (storage batteries). While primary batteries are not rechargeable, secondary batteries can switch chemical responses to electrical power many times. Also, secondary batteries can be arranged in several different types such as Nickel Cadmium (Ni-Cd), Nickel-Metal Hydride (Ni-MH), Lead Acid and Lithium-ion (Li-ion) due to their chemical decompositions [10]. One of the most common approaches for the battery classification is as explained in Table 1.1 categorizing by considering their size [11].

It makes sense to develop the battery technology for the systems in order to provide high energy and power with long life and low cost.

Table 1.1. Table of the categories of batteries considering their size.

Battery type according to size	Applications	Energy Range
Miniature batteries	Calculators, watches, implants…	100 mWh – 2 Wh
Batteries for portable equipment	Toys, mobile phones, computers…	2 Wh – 100 Wh
SLI batteries	Cars, trucks, buses…	100 Wh – 600 Wh
Vehicle traction batteries	Locomotives, fork-lift trucks…	20 kWh – 630 kWh
Stationary batteries	Local energy storages…	250 Wh – 5 MWh
Load levelling batteries	Load levelling, spinning reserve…	5 MWh – 100 MWh

Today, in order to provide those needs lead acid, manganese dioxide and lithium batteries (LIBs) are used. Nonetheless, the chemical properties of lithium metal provides LIBs higher energy, lighter weight and smaller size as shown in Figure 1.6 [12].

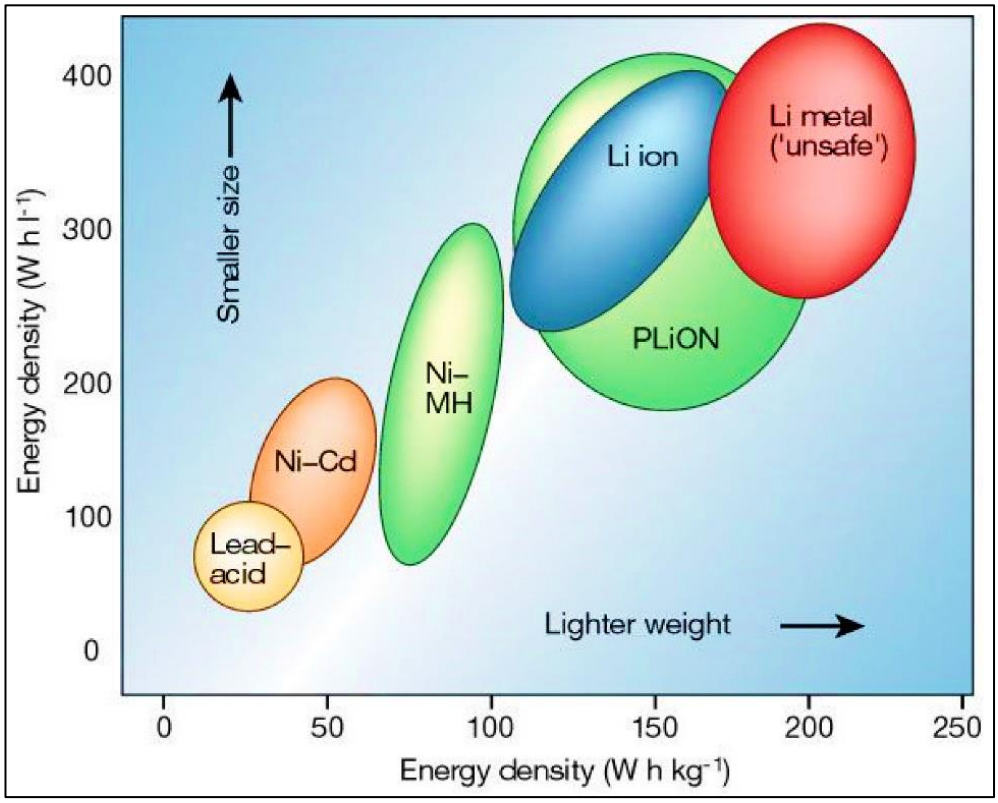

Figure 1.6. Energy density scale of various batteries.

While LIBs have higher efficiency, good cycle life and higher energy density with respect to other common batteries, several studies conducted aiming on the improvements about the higher cycle life, temperature dependent performance (especially in low-temperature) and manufacturing cost reduction [9,10]. Au contraire, while LIBs are first introduced as primary batteries, developments on the material technology and electrochemical improvements converted them into rechargeable secondary cells within the years. However, the first used rechargeable LIBs contributes to the safety problems in spite of the fact that the lithium dendrite formation and powder deposition of lithium metal while recharging. Thence, a new approach was developed called "Li-ion battery technology" by Sony Inc. and Asahi Chemical Co. and as the key factor was the instead of the use of lithium metal for negative electrodes carbon based lithium intercalation materials such as graphite as well as $LiCoO_2$ (lithium-cobalt-oxide) and $LiMnO_2$ (lithium-manganese-oxide) materials were used for the positive electrode material in order to overcome the safety issues [13].

1.3. Literature Review

Batteries can be modelled both electrical circuit and electrochemical modeling. While electrochemical modeling is complex and evaluation of electrochemical properties of a cell is difficult (see Chapter 4), electrical circuit i.e. equivalent circuit model (ECM) shows the electrical characteristics of the battery by using passive electrical elements such as capacitor, resistance and inductance or more complex elements such as Warburg element. According to an article published in 2014 [14] ECM can be classified into six main categories and different sub-categories.

Simple battery models classified into six sub-categories. The simplest one is ideal battery model which is suitable to simulate the power systems in steady state because the internal parameters and state-of-charge (SoC) of the battery are neglected. While simple battery model elements are independent from the relationship between the voltage and SoC of the battery, modified simple battery models consist of SoC dependent resistances [15–18].

Thevenin-based models consist of basically parallel arrangement of a resistance and a capacitor connected with internal resistance in series. All the parameters used in

Thevenin model are in relation with SoC, capacity, temperature or discharge flow current of the battery. Modified Thevenin battery models have advantages than simple battery models like evaluating the parameters of the battery in over charge/discharge, self-discharge states, transient behavior or nonlinear characteristics of the battery with respect to SoC [19–22].

Runtime-based model is a complex one which provides to simulate the DC response of the battery under constant discharge current flow. The model consists of three separated circuits to analyze the dependency of discharge current, dependency of SoC and discharge rate and lastly, open circuit voltage (OCV) and internal resistor [23].

Generic-based model is used in order to understand battery characteristics. This type of model is easy to use. On the other hand, temperature effect, capacity fade or self-discharge of the battery are ignored for the simulations. In addition, modified generic battery model provides to evaluate data from charge and discharge cycles of different types of battery technologies [24–26].

Another category of ECM is impedance-based model which provides to analyze the parameters by applying electrochemical impedance measurements. Resistance and capacitor (R-C) pairs are used in order to interpret the charge transfer, surface film values and Warburg element can be used to simulate the diffusion behavior of the battery. In many studies in order to decrease the complexity of model instead of using Warburg element, R-C or R-CPE (see Chapter 2) pairs are used considering the frequency range of the impedance measurements. In this model while the ambient temperature and SoC dependency are ignored the fitting mechanism is complicated. In order to fit the EIS data to equivalent circuit to obtain meaningful parameters various ECM had developed by different research groups as listed in Table 1.2.

Table 1.2. Various equivalent circuit models used by different research groups.

No.	ECMs for used for the impedance of batteries	Notes
1	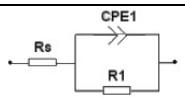	Resistive elements (R) are used in order to represent the DC resistance of the systems which are not frequency dependent. $Z = R$ Ideal capacitors (C) are used for the identify the capacitive behavior of frequency response of the system. $Z = \frac{1}{j\omega C}$ Inductors (L) are used to identify the inductive behavior of the system. $Z = j\omega L$ Constant phase elements (CPE) are mentioned as non-ideal capacitors. They are used to analyze the capacitive behavior of the system with constant phase angle. $Z = \frac{1}{(j\omega)^{\alpha} CPE}$ Warburg elements (W) are used in order to investigate the diffusion behavior and mass transport characterization of the system with 45 ° phase angle. $Z_W(\omega) = \xi\left(\frac{1-j}{\sqrt{\omega}}\right)$
2	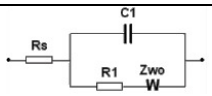	
3	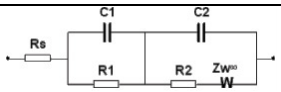	
4	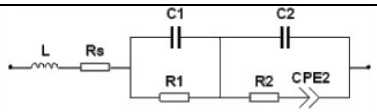	
5	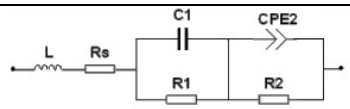	
6	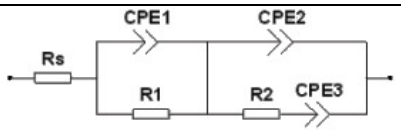	
7	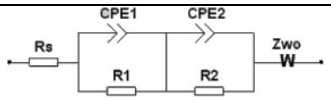	
8	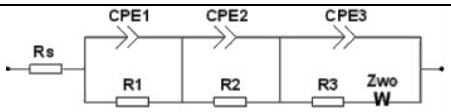	
9	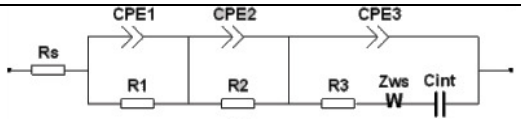	
10	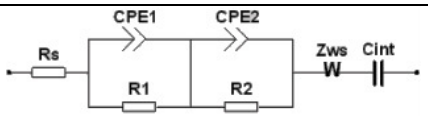	
11	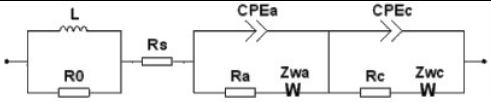	
12	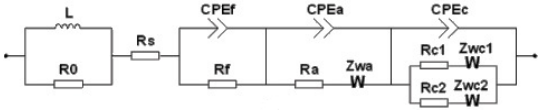	

Model 1 is used to analyze the behavior of charge transfer kinetics and double-layer characteristics in a narrow frequency range in other words diffusion behavior is excluded [27]. Model 2 is used for investigating the diffusion behavior using least number of components [28,29]. In order to focus on the solid-electrolyte interface (SEI) formation (see Chapter 3, 4), capacity loss, as well as low temperature dependence model 3 can be used [30–33]. Model 4 had been developed to analyze the cycle life and the inductive behavior of the batteries [34]. Model 5 is used to identify the effect of constant phase element on ion-diffusion instead of using Warburg element [35]. Model 6 had been developed with the aim of investigation of diffusion behavior of Lithium ions in graphite electrodes [36,37]. The use of CPE instead of C to represent heterogeneous interface. Model 7 had been developed for analyzing the diffusivity in a single-phase Vanadium pentoxide by excluding diffusion tail at low frequency [38]. While model 8 and 9 is used in order to study the dynamic response of LIBs and represent the ion diffusivity of the electrodes with special thicknesses [39], model 10 is modified version of model 9 had been constructed to investigate the diffusion behavior and the doping effects [40,41]. Finally, model 11 were used in order to analyzed capacity fade and Li^+ insertion effects and improved version of model 11 which is model 12 had been used for studying the particle size and SEI formation in positive electrode [42].

The other type of ECM is combined electrical circuit-based model, which is a combination of the Thevenin, impedance and runtime-based ECM. The model consists of energy balance and voltage response parts. While in the first part provides to detect the capacity, self-discharge and battery runtime, the second part helps to explain the voltage changes with respect to input current [23,43].

According to studies cited below, electrochemical modeling approach describes the chemical processes occurring in the batteries detailed. However, this approach comes with a complexity and time-spending computations. In order to overcome the complexity, several methods are developed. One of the most common approach is a time-dependent model based on Nernst's theory and it provides to solve the model with differential algebraic equations [44]. Although this lumped model is fast to solve, it is not representing the details of the electrochemical and physical processes as the battery technology is getting advanced.

The other approach for modeling most of the LIBs which uses the porous electrode theory developed by Newman et al. [45–47] provides to interpret the side

reactions, diffusion, mass transport and temperature effects also battery ageing in 1-D battery geometry. This method uses the partial differential equations-based Fick's law, Kirchhoff's law combined with Ohm's law, Nernst's and Butler-Volmer equations with porous electrode theory defined for each battery component (separator and negative-positive electrodes) [48–50]. While this approach still has problems like complexity and time-spending computations, there are several different techniques separately to decrease the computation time by turning partial differential equations into ordinary differential equations and to overcome the complexity neglecting some model parameters even it causes information loss.

Figure 1.7. [51] shows the 1-D isothermal EIS modeling of positive electrode of a battery consisting of $Li_{14}Ti_{15}O_{12}$ (LTO) material as negative and $LiNi_{0.08}Co_{0.15}Al_{0.05}O_2$ (NCA) material as positive electrode studied by Abraham et al. [52].

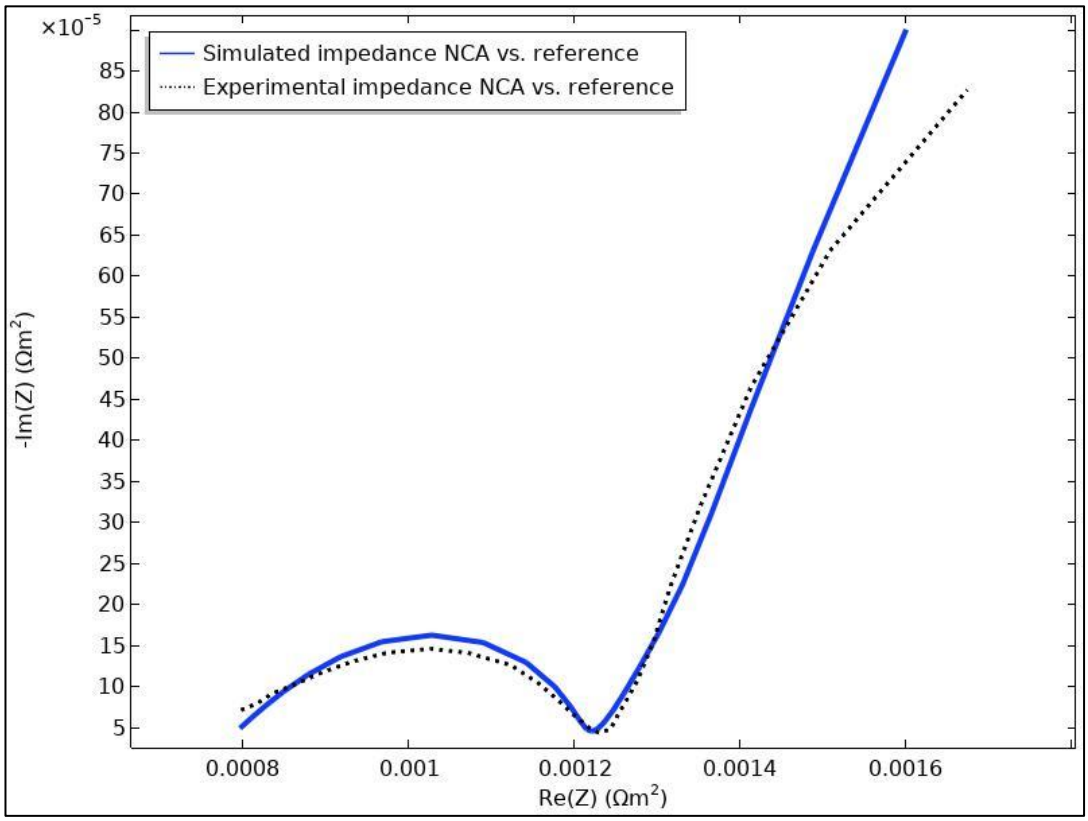

Figure 1.7. EIS model of NCA electrode based on porous electrode theory.

1.4. Motivation of the Study

Electrochemical impedance spectroscopy (EIS) is an essential method to investigate performance and shortcomings of batteries and fuel cells. The electrochemical impedance spectroscopy is used to analyze the frequency response of the system. A small sinusoidal AC input is applied at a varying frequency while the current or potential response is measured as the output. Like classical frequency response analysis methods, output is given as either Bode or Nyquist plots. Nyquist plot of a typical fuel cell or a battery system can be compared to the response of a simple electric circuit. Therefore, conventionally EIS analysis of fuel cells and batteries are carried out by fitting the response to a response of an equivalent circuit. However, equivalent circuit modeling (ECM) of EIS response gives limited information about the electrochemical systems. The entire response of the system is lumped into a single point as a capacitor or resistance. On the other hand, a fuel cell or a battery is comprised of anode, electrolyte and the cathode which have their own capacitance and resistance values. In order to differentiate between the capacitance of the anode and the cathode a more detailed modeling is required.

In this study a novel method will be developed to interpret the EIS results of an electrochemical system. Computational fluid dynamics (CFD) modeling of a battery cell will be developed to analyze frequency response of each system. The CFD response will be compared with the EIS data taken from the experiments conducted at particular operating conditions. The model parameters will be tuned as the EIS data will be fit to the model results. This way a more thorough understanding of the impedance data will be available to evaluate the performance of the electrochemical system.

2. THEORETICAL BACKGROUND

2.1. Electrochemistry

Electrochemistry is one of the widespread fields of chemistry and electrical science. Since the first electrochemical device, which is voltaic pile, was introduced in 1800, electrochemistry has been working on the electrical properties of the systems, chemical and surface developments of materials.

During charging and discharging of an electrochemical cell, chemical reactions such as oxidation (anodic process) and reduction (cathodic process) occurs and those are called as redox reactions. An example of such a reaction is given below:

$$Pb + PbO_2 + 4H^+ + SO_4^{2-} \rightarrow 2PbSO_4 + 2H_2O \quad (2.1)$$

A typical electrochemical cell consists of two electrodes separated by ion conductive electrolyte. Since the discharge and charge processes are occur in a cell, reduction and oxidation terms are interchangeable by each other. During the charge process oxidation occurs in positive electrode, during the discharge process negative electrode is oxidizing. In addition, reduction is also dependent to type of the process. Therefore, instead of naming anode and cathode for the electrodes, it would be simpler to name them as positive and negative electrodes.

While the open circuit voltage (OCV) of a cell which means the current application on cell equals to zero amperes i.e. the numerical value of the tendency of cell's reaction, depends on lithium concentration of electrolyte, temperature and discharge state the discharge potential (E) of cell is lower than OCV since it is dependent with ohmic losses and the discharge current. The relation between E_{OCV} and E simply shown as a linearized formula:

$$E = E_{OCV} - IR_{eq} \quad (2.2)$$

While R_{eq} represents the internal resistance of the electrochemical cell, which depends on the contact resistance, ion migration resistance within the electrolyte, and

electron transport resistance between electrodes and current collectors, discharge current denoted as I.

In addition, temperature dependence of the cell OCV could be associated with the formula given below:

$$E_{OCV}(T) = E^0 + \frac{(T - T_0)\Delta S}{nF} \tag{2.3}$$

While E^0 represents the open circuit potential at T_0 K, ΔS associated with entropy change. T is the ambient temperature in Celsius degree.

The cell capacity "Q" of ideal storage systems expressed as ampere-hours (Ah). It means measurement of stored Coulombs by drawing amperes in an hour. Ideally, discharge capacity equals to charge capacity but in many cases, they are not equal and the rate between those called as "Coulombic efficiency" (μ_Q). The discharge (charge) capacity can be calculated either a formula or from a discharge (charge) curve of a cell. The area under the fully charged (discharged) batteries' discharge (charge) curve equals to the discharge (charge) capacity.

$$Q_{cell,d} = \int_0^t I_{disch} dt \tag{2.4}$$

$$Q_{cell,c} = \int_0^t I_{ch} dt \tag{2.5}$$

$$\mu_Q = \frac{Q_{cell,d}}{Q_{cell,c}} \tag{2.6}$$

A typical discharge curve (also named as a polarization curve) consist of three zones, as shown in the Figure 2.1. [9] first zone corresponds to (where the rapid voltage drop is seen) polarization overvoltage or the passive film layer of the electrodes, the second zone (where slow voltage drop is seen) corresponds to internal cell resistance, the third zone (where the last region that rapid voltage drop occurs) is addressing the voltage polarization and electrode polarization.

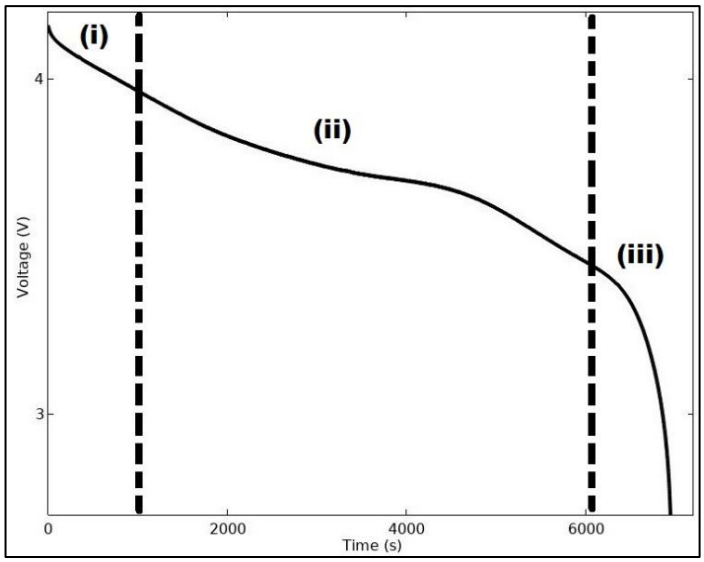

Figure 2.1. Typical discharge curve of an electrochemical cell.

During the electrochemical processes in a cell free energy change and enthalpy change should be considered. Thermodynamically, free energy change ΔG^0 in joules equals to:

$$\Delta G^0 = -w_{max} = -nFE^0 \tag{2.7}$$

Here, number of electrons transferred per 1 mole n by Faraday constant F equals to charge transfer with an applied voltage, E^0 represents the potential difference of the cell and "w_{max}" is the work done by the cell i.e. the theoretical available energy per 1 mole reaction either in joules (J) or watt hours (Wh).

The power generated by cell "P" is described as current flow through the cell "I_{app}" (A) multiplied by the cell voltage "E" (V).

$$P = I_{app}E \tag{2.8}$$

The enthalpy change "ΔH" is dependent on work done by the cell "$(w_{out})_{max}$" and the heat given out to the atmosphere "$(q_{out})_{min}$".

$$-\Delta H = (w_{out})_{max} + (q_{out})_{min} \tag{2.9}$$

All aside, lithium batteries works with inner-sphere mechanism [53], which limits the charge transfer and potential (lithium particles have to be transferred one electrode to the other in electrolyte solution). Moreover, the energy stored in a cell is related with the electrical double-layer (EDL) that affects charge transfer kinetics and electrochemical reaction rates. EDL is a non-uniform transition boundary region (interphase) between the liquid and the solid phase [54].

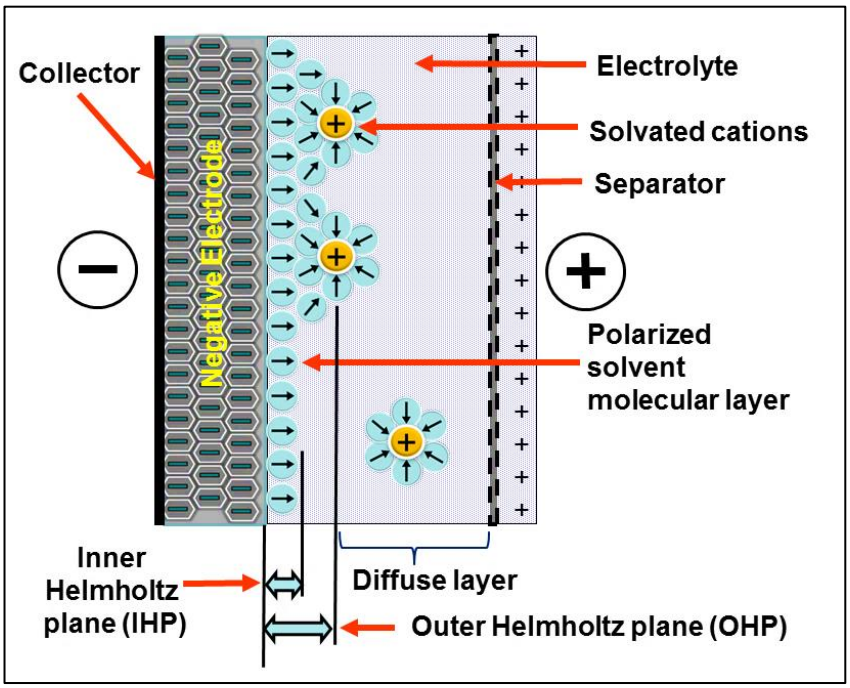

Figure 2.2. Representation of electrical double layer.

EDL could be investigated as two regions: the inner layer where inner-sphere reactions (slow reactions) are observed and the diffuse layer where outer-sphere reactions (fast reactions) occur. As shown in Figure 2.2., while the region near to the surface of the electrode, the anions tend to have strong chemical bonding, in diffuse layer electrostatic forces and could be observed. Besides, temperature, electrolyte concentration and electrical characteristics of the solvent affects the depth of diffuse layer. Nevertheless, while the inner-sphere reactions where intercalation of the particles and insertion of electrochemical species are observed strongly dependent to electro catalytic properties of used electrode, outer-sphere reactions where typical redox reactions occur are dependent to electrolyte properties.

2.2. Frequency Response of a System

Frequency-response analysis of a system is a critical method to study output of the system given sinusoidal input in a varying frequency range. EIS analysis can be converted both Bode diagrams and polar i.e. Nyquist plots due to the advantages of the ready to applicable sinusoidal signals and accurate measurements with minimizing the noise [13].

In order to obtain sinusoidal output for a linear and stable system, the transfer function $G(s) = \frac{P(s)}{Q(s)} = \frac{P(s)}{(s+s_1)+(s+s_2)\dots(s+s_n)}$ is used with an input of $x(t) = Xsin\omega t$. Here, the term ω represents the frequency in the units of rad/s. The frequency response of given system can be obtained by changing the s with $j\omega$ in its transfer function.

By applying Laplace transformation to the system:

$$Y(s) = G(s) \cdot X(s) = G(s) \cdot \frac{\omega X}{s^2 + \omega^2} = \frac{a}{s + j\omega} + \frac{\overline{a}}{s - j\omega} + \frac{b_1}{s + s_1} + \frac{b_2}{s + s_2} \dots + \frac{b_n}{s + s_n} \tag{2.10}$$

Where $X(s)$ is the Laplace transformation of the input signal, a and b_i represent the constants of the function and $\overline{a}$ denotes the complex conjugate of the constant a.

The inverse Laplace of the resultant equation can be written as by considering $t \geq 0$:

$$y(t) = ae^{-j\omega t} + \overline{a}^{j\omega t} + b_1 e^{-s_1 t} + b_2 e^{-s_2 t} \dots + b_n e^{-s_n t} \tag{2.11}$$

As it mentioned before, for a stable and linear system as $t \to \infty$ the term of $e^{-s_i t}$ approaches to the zero because of the term s_i includes the negative real numbers. ($i = (1, 2, \dots, n)$).

Therefore, the response of the system can be rearranged as:

$$y(t) = ae^{-j\omega t} + \overline{a}^{j\omega t} \tag{2.12}$$

The constants a and $\overline{a}$ can be obtained by using the S-domain function, which are:

$$a = G(s)\frac{\omega X}{s^2 + \omega^2}(s + j\omega) \tag{2.13}$$

$$\overline{a} = G(s)\frac{\omega X}{s^2 + \omega^2}(s - j\omega) \tag{2.14}$$

After replacing the term s with $-j\omega$ for the constant a and $j\omega$ for the constant $\overline{a}$ the resultant constants can be rewritten as below.

$$a = -X\frac{G(-j\omega)}{2j} \tag{2.15}$$

$$\overline{a} = X\frac{G(j\omega)}{2j} \tag{2.16}$$

In order to identify the magnitude and the angle of the function the following equations should be considered.

$$G(j\omega) = |G(j\omega)|e^{j\psi} \tag{2.17}$$

$$G(-j\omega) = |G(-j\omega)|e^{-j\psi} = |G(j\omega)|e^{-j\psi} \tag{2.18}$$

After identifying those functions, the constants can be rewritten as:

$$a = -X\frac{|G(j\omega)|e^{-j\psi}}{2j} \tag{2.19}$$

$$\overline{a} = X\frac{|G(j\omega)|e^{j\psi}}{2j} \tag{2.20}$$

While ϕ denotes the angle of the function, the value of it can be obtained by using geometrical relation between the imaginary and real parts of the function G.

$$\psi = \tan^{-1}\left[\frac{imaginary\ part\ of\ G(j\omega)}{real\ part\ of\ G(j\omega)}\right] \tag{2.21}$$

When turning back to the function of $y(t)$ and placing the constants a and $\overline{a}$ into it, the resultant steady-state, sinusoidal output can be evaluated as below transforming the exponential form of the term to the trigonometric function by using the Euler's transformation, where $Y = X|G(j\omega)|$.

$$\begin{aligned} y(t) = X|G(j\omega)|\frac{e^{j(\omega t+\psi)} - e^{-j(\omega t+\psi)}}{2j} &= X|G(j\omega)|\sin(\omega t + \psi) \\ &= Y sin(\omega t + \psi) \end{aligned} \tag{2.22}$$

The frequency-response characteristics of a system can be represented in graphical forms with its transfer function, phase angle, magnitude and frequency parameter in either in Bode diagrams or Nyquist plots.

A Bode diagram shows either the logarithmical magnitude of a transfer function in decibels (for an EES in Ohms) against the frequency or the phase angle in degrees vs. the frequency on a logarithmic scale. The basic principle of the Bode representation is the turning exact curves by using asymptotic approximation of the straight lines to determine the frequency-response characteristics. The magnitude of the transfer function generally represented as $G(j\omega) = 20\log|G(j\omega)|$ where the base logarithm is 10.

Moreover, bode diagrams are commonly used representation method for the frequency-response analysis (FRA) because of the fact that Bode plots are easy to plot, simple to rearrange or modificate, also it requires less time than the other computational methods for the FRA. The procedure of plotting the Bode diagram is starting with rewriting the transfer function $G(j\omega)H(j\omega)$ and continuing with the identification of the corner frequencies. After drawing the asymptotic magnitude curves with their slopes, the exact curve can be obtained by correcting them properly [55].

A Nyquist plot i.e. polar plot is a complex representation method of the magnitude of a certain sinusoidal transfer function $G(j\omega)$ against the phase angle varies from zero to infinity. The points represented in the graph responsible for the

magnitude of the transfer function on associated frequency ω. The plot projects real component on x-axis and imaginary component on y-axis of the transfer function. High frequency to low frequency can be observed from left to the right in the graph. Despite of the fact that the main advantage of using the polar plot is that the entire frequency-response characteristics for all frequencies of the system can be studied in a single plot, it is not clear to observe the contributions of individual factors of the transfer function [56].

For example, assuming the sinusoidal transfer function has given as:

$$G(j\omega) = \frac{1}{1 + j\omega T} \tag{2.23}$$

When considering $\omega \to \infty$, magnitude of the transfer function approaches to 0 also the phase angle approaches to -90°. If as $\omega \to 0$, magnitude of the transfer function would be 1, and the phase angle is derived as 0 °. Nevertheless, $\omega \to \frac{1}{T}$, magnitude of the transfer function will be $1/\sqrt{2}$ with the phase angle of 45 °. The Nyquist plot of the system can be plotted as a semi-circle centered at the 0.5 on the real axis with the radius of 0.5.

If the transfer function $G(j\omega) = X + jY$, the real and imaginary parts of this function can be written as below.

$$Re\{G(j\omega)\} = \frac{1}{1 + \omega^2 T^2} \tag{2.24}$$

$$Im\{G(j\omega)\} = -\frac{\omega T}{1 + \omega^2 T^2} \tag{2.25}$$

2.3. Electrochemical Impedance Spectroscopy

Electrochemical Impedance Spectroscopy (EIS) is one of the most effective experimental approaches in order to interpret the physical meanings of such as reduction and oxidation reactions occurring in electrochemical systems under steady state conditions, stress values for mechanical systems, viscosity and corrosion rates of

materials or biological membranes. EIS measurement technique is simply a Laplace transformation of transient response of working materials perturbed with sinusoidal voltage or current. The resulted perturbation/answer ratio described as impedance (Z) in frequency domain. Since the distorted data could be occurred during the EIS measurements because of antenna effect or cell geometry, ideal frequency range in standard measurements is between 1 MHz and 100 mHz. During the experiments conducted in low frequencies (<100 mHz), it is highly important to put the working materials under constant pressure, constant temperature and stable conditions. On the other hand, at high frequency range (>100 MHz) electrodes and electrolyte could affected by noise which results with a data seriously distorted [57].

The main approach of the EIS is application of known voltage or current to the electrodes and analyzing the response of the system. According to Hara et al. (2013) [57] explained that there are mainly three types of electrical stimuli application in order to observe the response of the system. Firstly, application of step function of voltage for transient measurements, which leads to measure the time varying current response. While this method is simple and easy, at the end of the measurements, impedance may not be observed clearly in a specific frequency. The second method is application of the voltage signal mixed with white noise to the electrodes. However, it is difficult to identify the true white noise for the measurements. On the other hand, this method provides a good signal to noise ratio for the specific frequencies. The last method is most common and standardized one, which has an ability to measure the frequency response, current response, amplitude and phase shift of the cells in wide frequency range.

Impedance is a complex variable that consists of real and imaginary parts of impedance that leads to analyze the resistive and capacitive behaviors of working material. While the resistive behavior, which equals to real part of impedance called as resistance (R), the capacitive behavior, which is the imaginary part of impedance called as capacitive or inductive reactance (X_C or X_L), and both of them frequency dependent values. As they could represented in Cartesian coordinates, polar form includes more data like magnitude and phase shift of impedance with the help of Euler's transformation.

$$X_C = \frac{1}{2\pi f C} \tag{2.26}$$

$$X_L = 2\pi f L \tag{2.27}$$

$$Z = R + j \cdot X \tag{2.28}$$

Above, while Z is representing impedance, R denotes the resistance, j is the imaginary number and X is reactance. Also, capacitive reactance can be calculated where C is capacitance in the units of Farads and L is used in Henrys to calculate the inductive reactance of a system.

According to a study conducted in 1994 by Sluyters-Rehbach [53] in order to eliminate the confusion for the identification of impedance symbols while the imaginary number $\sqrt{-1}$ denoted with j, which is electrical engineering tradition instead of the IUPAC notation, the real part of the impedance denoted with Z_r and the imaginary part of impedance indicated with Z_j.

Mathematical Concept of Electrochemical Impedance Spectroscopy:

While the EIS measurements are performed by applying a small sinusoidal voltage to the cell, because of the fact that electrochemical systems are non-linear systems the current response will appear as periodic, but not sinusoidal. On the other hand, the non-linear response of the system depends on the perturbation signal. However, as decreasing the amplitude of the signal increase the noise in the measurements, higher signal rates are not effective to detect the electrochemical characteristics of the system. In general, EIS measurements of electrochemical systems are performed with the perturbation of 5 mV/s and 10 mV/s [54,58–65].

In a simple electrical circuit, potential (V) can be calculated by multiplying the current applied over the system in the unit of A and resistance of the system in ohms:

$$E(t) = I_{app}(t)R \tag{2.29}$$

Here, applied current can be calculated by considering the derivative of the electric charge with respect to application time:

$$I_{app}(t) = \frac{dq(t)}{dt} \tag{2.30}$$

On the other hand, inductor and capacitor can be evaluated as below:

$$E(t) = L\frac{dI_{app}(t)}{dt} \tag{2.31}$$

$$I_{app}(t) = C\frac{dE(t)}{dt} \tag{2.32}$$

L represents the inductor value in Henries (H) and C corresponds to capacitor value in Farads (F).

Additionally, EIS results may be obtained both in time domain and frequency domain. Also, it is possible to get information of the magnitude and the phase shift of the perturbing signal with respect to the frequency range. Furthermore, it is complicated to analyze the response of more than one signal in time domain. At this point, the mathematical operation called “Fourier Transform” is used to convert time domain responses to frequency domain [13].

Assuming, a time domain periodic function of $f(t)$ represented as:

$$f(t) = a_0 + \sum_{n=1}^{\infty}(a_n \cos \mathrm{n}\omega\mathrm{t} + b_n \sin \mathrm{n}\omega\mathrm{t}) \tag{2.33}$$

If the Euler formula is applied in order to make a connection between the trigonometric equations and the complex identities:

$$f(t) = c_0 + \sum_{n=1}^{\infty}(c_n exp\ (jn\omega t) + c_m exp\ (-jn\omega t)) \tag{2.34}$$

Here,

$$c_n = \frac{a_n - jb_n}{2} \tag{2.35}$$

$$c_m = \frac{a_n + jb_n}{2} \tag{2.36}$$

$$c_0 = a_0 \tag{2.37}$$

Lastly, a simple form of the given formula can be expressed as:

$$f(t) = \sum_{n=-\infty}^{\infty} (c_n \exp(jn\omega t)) \tag{2.38}$$

In order to finalize the simple Fourier analysis for EIS measurement, the coefficient c_n can be expressed as a period T with respect to frequency ω by integrating and converting the trigonometric function:

$$c_n = \frac{1}{T}\int_0^T f(t)\big(\cos(n\omega t) - jsin(n\omega t)\big)dt \tag{2.39}$$

Now, supposing that the perturbation signal given to the system as a linear sinusoidal function in time domain:

$$E_{in}(t) = \Delta E_{in}.cos(\omega t) \tag{2.40}$$

The answer of the system (response current) can be obtained with a phase shift in time domain. Which is:

$$I_{out}(t) = \Delta I_{out}.cos(\omega t + \psi_1) = a_1\, cos(\omega t) + b_1 sin\,(\omega t) \tag{2.41}$$

While ΔE represents the amplitude of input signal in volts, ΔI is responsible for the output current amplitude in amperes in time domain. ψ_1 corresponds to the phase shift between the input and output signals.

While the real and imaginary parts of input signal in frequency domain can be written as:

$$E_{in,r}(\omega) = \frac{1}{T}\int_0^T E_{in}(t)\cos(\omega t)\,dt \tag{2.42}$$

$$E_{in,j}(\omega) = -\frac{1}{T}\int_0^T E_{in}(t)\sin(\omega t)\,dt \tag{2.43}$$

The real and imaginary parts of the output current in frequency domain is:

$$I_{out,r}(\omega) = \frac{1}{T}\int_0^T I_{out}(t)\cos(\omega t)\,dt \tag{2.44}$$

$$I_{out,j}(\omega) = -\frac{1}{T}\int_0^T I_{out}(t)\sin(\omega t)\,dt \tag{2.45}$$

At the end, the real and imaginary parts of impedance can be calculated by using input and output signals in complex representation.

$$Z_r(\omega) = Re\left\{\frac{E_{in,r} + jE_{in,j}}{I_{out,r} + jI_{out,j}}\right\} \tag{2.46}$$

$$Z_j(\omega) = Im\left\{\frac{E_{in,r} + jE_{in,j}}{I_{out,r} + jI_{out,j}}\right\} \tag{2.47}$$

Thus, impedance can be simply represented as:

$$|Z(\omega)| = \sqrt{Z_r(\omega)^2 + Z_j(\omega)^2} \tag{2.48}$$

And the phase angle can be formulated by using the inverse tangent function of the rate of the imaginary part of the impedance and the real part of the impedance. It is important to use constant phase element (CPE) in order to describe the phase angle as constant for all the elements of a simple electrical circuit.

$$\psi(\omega) = \tan^{-1}\left(\frac{Z_j(\omega)}{Z_r(\omega)}\right) \tag{2.49}$$

As discussed in Section 2.3, the real part of impedance corresponds to resistive behavior of the system, which is independent from frequency while the imaginary part is inductive or capacitive behavior. For a circuit with two elements arrangement (R_0 as a resistor, C as a capacitor) connected in series, impedance can be formulated as:

$$Z = R_0 + j\frac{1}{\omega C} \tag{2.50}$$

Impedance can be formulated for the common energy conversion systems as assuming the resistor R_0 is connected in series to the parallel arrangement of R and C elements.

$$Z = R_0 + \frac{R}{1 + j\omega RC} = R_0 + \frac{R}{1 + (\omega RC)^2} - j\frac{\omega R^2 C}{1 + (\omega RC)^2} \tag{2.51}$$

Considering as the frequency ω approaches to zero, while the real part of the impedance will approach to $R_0 + R$, imaginary part of the impedance will approach to zero as well. On the other hand, while the frequency ω approaches to infinity, the resultant impedance will approach to R_0 and its imaginary part will approach to zero.

Additionally, the magnitude of the impedance and the phase angle can be calculated as for this system:

$$|Z| = \sqrt{\left[R_0 + \frac{R}{1 + (\omega RC)^2}\right]^2 + \left[\frac{\omega R^2 C}{1 + (\omega RC)^2}\right]^2} \tag{2.52}$$

$$\psi = \tan^{-1}\left(\frac{\omega R^2 C}{R + R_0(1 + (\omega RC)^2)}\right) \tag{2.53}$$

In practice, electrochemical systems are not ideal electric circuits. In fact, due to the non-homogenous surface of the electrodes or the charge transfer reactions in order to using an ideal capacitor CPE has been used [66]. The impedance of a series arrangement system with R_0 and CPE can be calculated by using the formula given below:

$$Z(\omega) = R_0 + \frac{1}{(j\omega)^{\alpha} CPE} \tag{2.54}$$

Here, while the value of α equals to 1, CPE represents the capacity of the system (simply the capacitance). On the other hand, when α is less than 1 (greater than 0) real capacitance of the system can be obtained by using the relation between the CPE and C:

$$C = \frac{(CPE.R_0)^{\frac{1}{\alpha}}}{R_0} \tag{2.55}$$

One of the most important elements as an additive to the electrical circuit for EIS measurements is the convective-diffusion impedance, also called as "Warburg Impedance" –simply, a constant phase element with 45 ° constant phase angle, which is associated with the mass transfer and the diffusion behavior of the system. Warburg element is generally connected in series with R parallel to C (or CPE) or to the final part of the equivalent circuit. In general, the semi-finite Warburg impedance is related with the diffusion tail as a straight line (can be observed at the low frequency region) in a properly obtained Nyquist diagram. The phase angle of the diffusion tail can be observed as 45° in the diagram.

The equation of the semi-finite Warburg impedance is given below, only if Eq. (2.57) considered:

$$Z_W(\omega) = \xi\left(\frac{1 - j}{\sqrt{\omega}}\right) \tag{2.56}$$

ξ is associated with the Warburg coefficient (Ωs^{-1}) and CPE and ξ are related with each other when α value fixed to 0.5 by the equation:

$$\xi = \frac{1}{\sqrt{2}.CPE} \tag{2.57}$$

Furthermore, the low frequency response of the battery associated with mass transport and diffusion might be observed as two different types which are finite-length Warburg (FLW) impedance and finite-space Warburg (FSW) impedance at low frequency (< 1 mHz). While FLW is associated with ideal reservoir at the boundary, FSW is associated with limited electroactive substance [67]. Figure 2.3. [68] shows the behavior of the impedance tail types. Although it is difficult to show impedance characteristics in diffusion layer by R, L, C elements, combinations of R-C element pairs can provide information about mass transfer mechanism in diffusion layer.

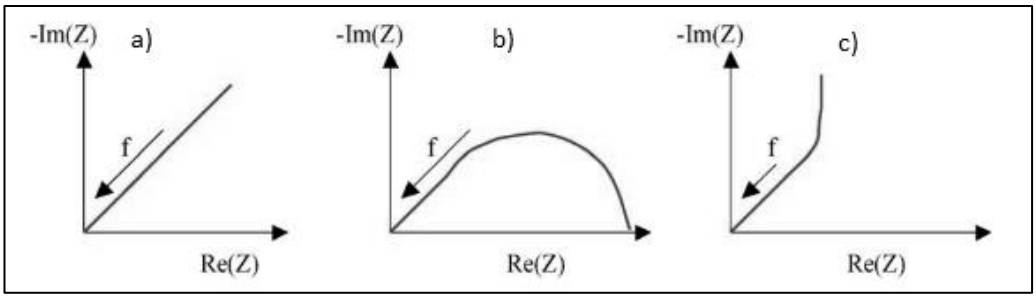

Figure 2.3. Diffusion effects observed in Nyquist plot. a) CPE, b) FLW and c) FSW.

In addition, the evaluation of the FSW and FLW elements can be obtained by using the equation mentioned in a study published by Xu et al. [69] as below:

$$Z_{FSW}(j\omega) = \sqrt{\frac{R_D}{j\omega C_D} \cdot \coth\left(\sqrt{R_D \cdot j\omega C_D}\right)} \tag{2.58}$$

$$Z_{FLW}(j\omega) = \sqrt{\frac{R_D}{j\omega C_D} \cdot \tanh\left(\sqrt{R_D \cdot j\omega C_D}\right)} \tag{2.58}$$

In the formulas given above, R_D and C_D represent the resistance and capacitance values in diffusion region of the impedance spectra.

Impedance of the system can be calculated also using the electrical double-layer capacitance and Warburg impedance. EDL capacitance is denoted as C_{dl} (F) below.

$$Z(\omega) = R_0 + \frac{R + Z_W(\omega)}{1 + j\omega C_{dl}(R + Z_W(\omega))} \tag{2.59}$$

3. EXPERIMENTAL METHOD

In the experimental part, three identical commercial SLPB75106100 pouch type Li-ion batteries manufactured by Kokam and three identical SONY Murata US18650VTC5 cylindrical type batteries were used for the experiments by considering their high energy density, high efficiency (According to [70] more than 96%), their reliability and safety features. Furthermore, SLPB batteries are called as "Ultra High-Power Batteries" by Kokam because of the fact that their increased cycle life, high energy, low internal resistance and low heat generation. The cells were made from Lithium Nickel Manganese Cobalt Oxide (NMC) material as positive electrode, graphite material as negative electrode and LP-30 as electrolyte, which is 1.0 M $LiPF_6$ (Lithium hexafluorophosphate) solution in ethylene carbonate and dimethyl carbonate (EC/EMC 1:1) mixture.

During the experiments Nüve Climate Chamber ID 301 for temperature control, ARBIN BT2000 battery tester for transient analysis (pulse tests, polarization tests) and GAMRY 5000E Interface Potentiostat/Galvanostat/Zero-Resistance-Ammeter for impedance measurements were used.

Thanks to the wide test temperature range (-40 °C - +150 °C) of Nüve Climate Chamber ID 301 and the humidity range (15% - 98%) between 10 °C and 90 °C the ambient temperature was stabilized during the tests with ±1 °C tolerance range. Figure 3.1. shows the climatic test cabinet used in the experiments.

Figıre 3.1. Nüve ID 301 climatic test cabinet.

ARBIN BT2000 battery tester is a good solution to do experiments with flexible specifications such as voltage range and current range. Although one channel used in the experiments, due to the well-designed compact system the test station has an ability to do multiple tests simultaneously without affecting other channels. The test station allows to do some common applications such as life cycle tests, device simulation and telecommunications battery testing. Nevertheless, the test station can supply voltage up to 60 V and current up to 2500 A, also it has an ability to show real time temperature of tested item by connecting thermocouples. Figure 3.2 shows the test station used in the experiments.

Figure 3.2. ARBIN BT2000 battery tester.

Impedance measurements were conducted with GAMRY Interface 5000E potentiostat fully featured potentiostat/galvanostat for testing of batteries, fuel cells and supercapacitors. While the voltage range is ±6 V, the current range is ±5 A. Electrochemical energy tests, critical pitting temperature, pulse voltammetry and electrochemical impedance, DC corrosion tests, physical electrochemistry and electrochemical noise tests are included in the techniques. The potentiostat has an ability to do 2, 3, 4 and 5 electrode measurements for half cells and full cells. Also, it has a wide frequency range (10 μHz - 1 MHz) for EIS measurements. The potentiostat used in the experiments shown in Figure 3.3.

Figure 3.3. GAMRY 5000E Potentiostat.

3.1. Discharge Characteristics

Charging and discharging of the batteries give information about the details – which affect the performance and efficiency of the electrochemical systems- such as State of Charge (SoC), State of Health (SoH), capacity and electrochemical dependency for the controllable parameters like pressure, ambient temperature and discharge current flow rate (C-rate) [58,71–74]. Hence, by considering the importance of those mentioned above, discharge tests were obtained for this study for the determination of the parameters.

3.1.1. Discharge Characteristics of Kokam SLPB75106100 Pouch Type Battery

During the measurements, ambient temperature and discharge current flow rate were controlled with ARBIN Battery Tester at atmospheric pressure in Nüve Climatic Chamber. With respect to the battery specifications as indicated in Table 3.1. (see also Appendix A), while maximum voltage value is 4.2 V, the minimum voltage value is 2.7 V. The measurements were performed constant current-constant voltage charge-discharge (CC-CV) technique.

The tests were conducted at 0 °C, 25 °C and 40 °C with 0.5 C discharge current and discharging at constant temperature with different C-rates under atmospheric pressure. Before the tests, battery tabs were cleaned with ethyl alcohol and put the climate chamber for temperature balancing. The same preparation procedure was followed during the tests.

Table 3.1. Battery specifications of Kokam SLPB75106100 pouch type battery.

Property	Unit	Value
Nominal Voltage	V	3.7
Charge-up Voltage	V	4.2
Discharge cut-off Voltage	V	2.7
Internal resistance	mΩ	4
Nominal Capacity	mAh	7.5

The batteries were firstly charged up to 4.2 V with desired constant C-rate and at that point constant voltage procedure was started to fix the voltage at 4.2 V with decreasing current flow rate until the current flow reaches to cut-off current 100 mA. Charge process lasted with 30 minutes relaxation ($i(t) = 0\ A$) time.

Discharge processes were performed with application of various C-rated discharge current to the cut-off voltage 2.7 V. After the batteries reached the cut-off voltage, charging process were applied. The results are shown in Figure 3.4.

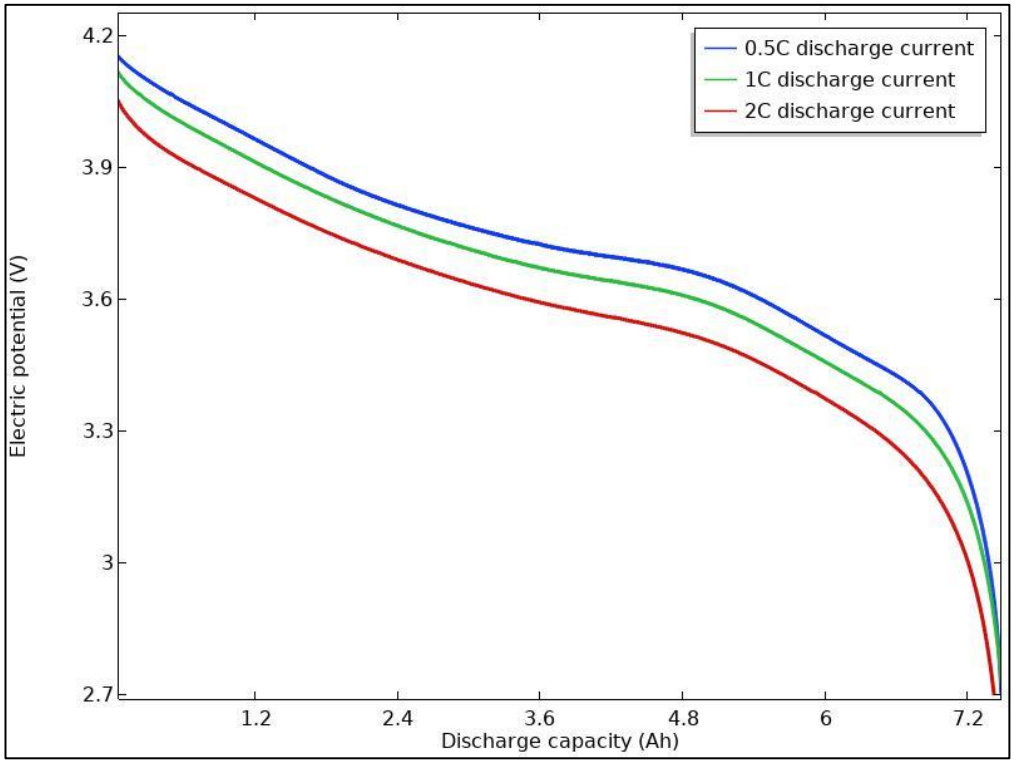

Figure 3.4. Experimental discharge curves of the battery applied different C-rated discharge currents at 25 °C ambient temperature.

In order to obtain proper data while charge-discharge processes, constant current-constant CC-CV technique with 0.5 C-rate were performed in 0 °C, 25 °C and 40 °C ambient temperatures. Before starting the tests, batteries were put in Nüve climate chamber for an hour in chosen ambient temperature in order to balance the batteries' internal temperature and operation temperature. The results are shown in Figure 3.5.

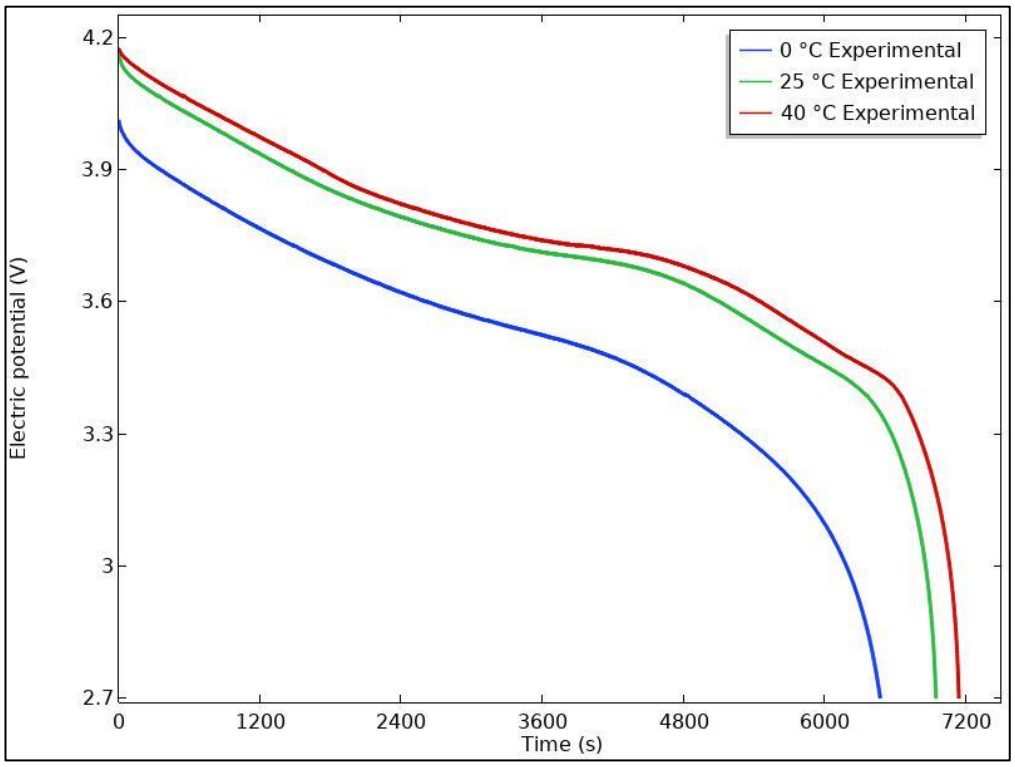

Figure 3.5. Experimental discharge curves of the battery at different ambient temperatures by discharging with 0.5 C-rate.

3.1.2. Discharge Characteristics of SONY Murata 18650 Cylindrical Type Battery

The cylindrical type batteries are firstly charged up to 4.2 V and discharged to 2.5 V with the same process as indicated in Section 3.1.1. The tests were performed with respect to the battery specifications indicated in Table 3.2. The C-rate dependency of the batteries had been obtained by discharging the batteries in various operation temperatures with 1 C, 0.5 C and 0.2 C until the voltage reaches 2.5 V with 100 mA cut-off current.

Table 3.2. Battery specifications of SONY Murata 18650 cylindrical battery.

Property	Unit	Value
Diameter	mm	18.35
Length	mm	65.2
Weight	g	44.3
Nominal Voltage	V	3.6
Charge-up Voltage	V	4.2
Discharge cut-off Voltage	V	2.5
Internal Resistance	mΩ	13.0
Nominal Capacity	mAh	2577

Figure 3.6. represents the discharge characteristics of the battery at 0 °C, 25 °C and 40 °C with the application of 1 C current flow rate. Figure 3.7., Figure 3.8. and Figure 3.9. show the current flow rate dependency of the batteries at 0 °C, 25 °C and 40 °C operation temperatures respectively.

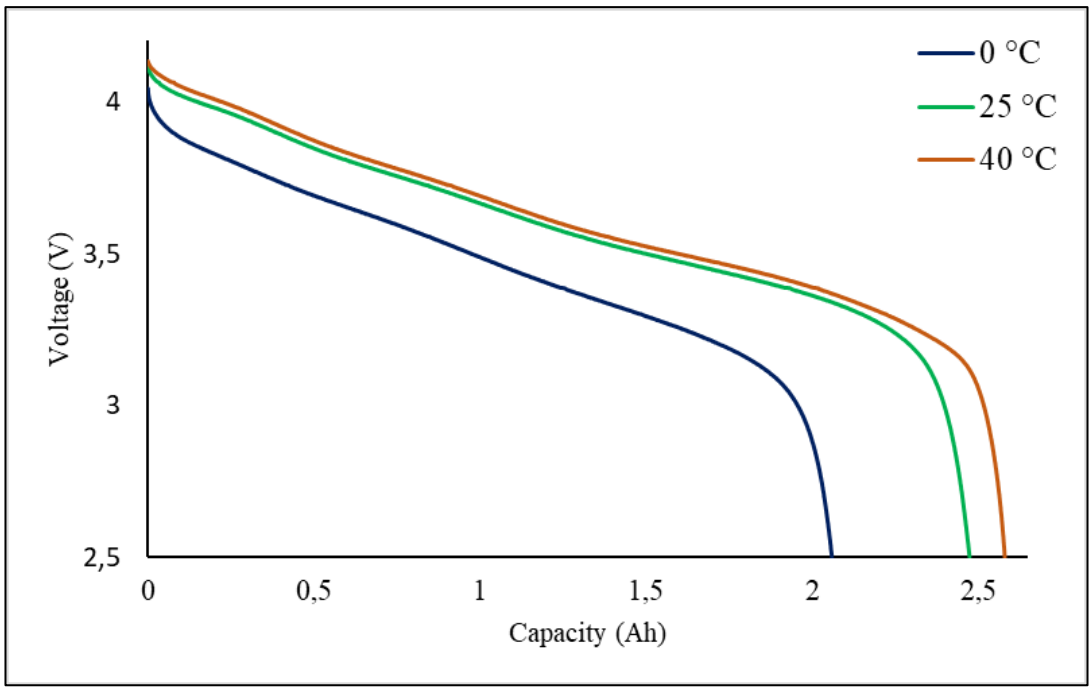

Figure 3.6. Experimental discharge curves of the battery at different ambient temperatures by discharging with 1 C-rate.

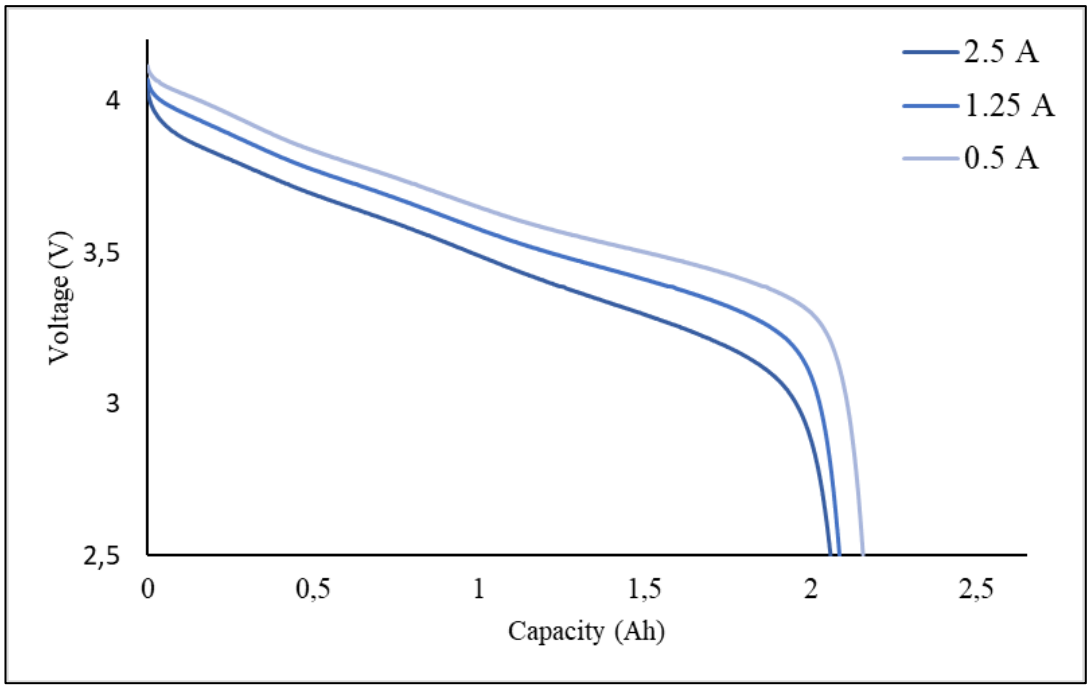

Figure 3.7. Experimental discharge curves of the battery with different current flow rates at 0 °C.

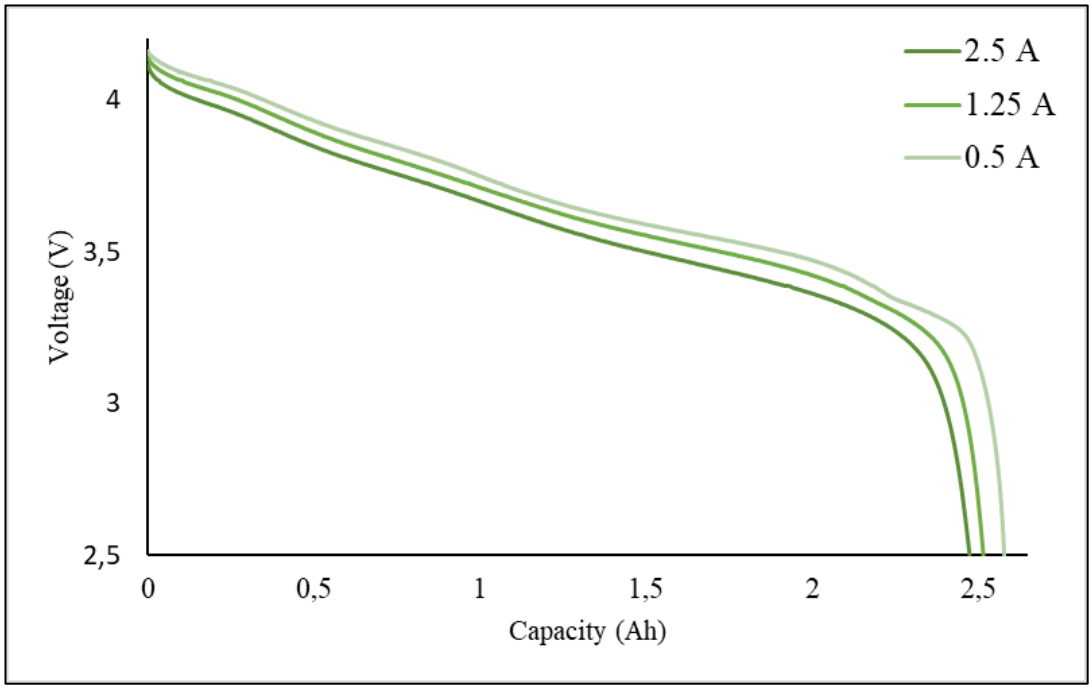

Figure 3.8. Experimental discharge curves of the battery with different current flow rates at 25 °C.

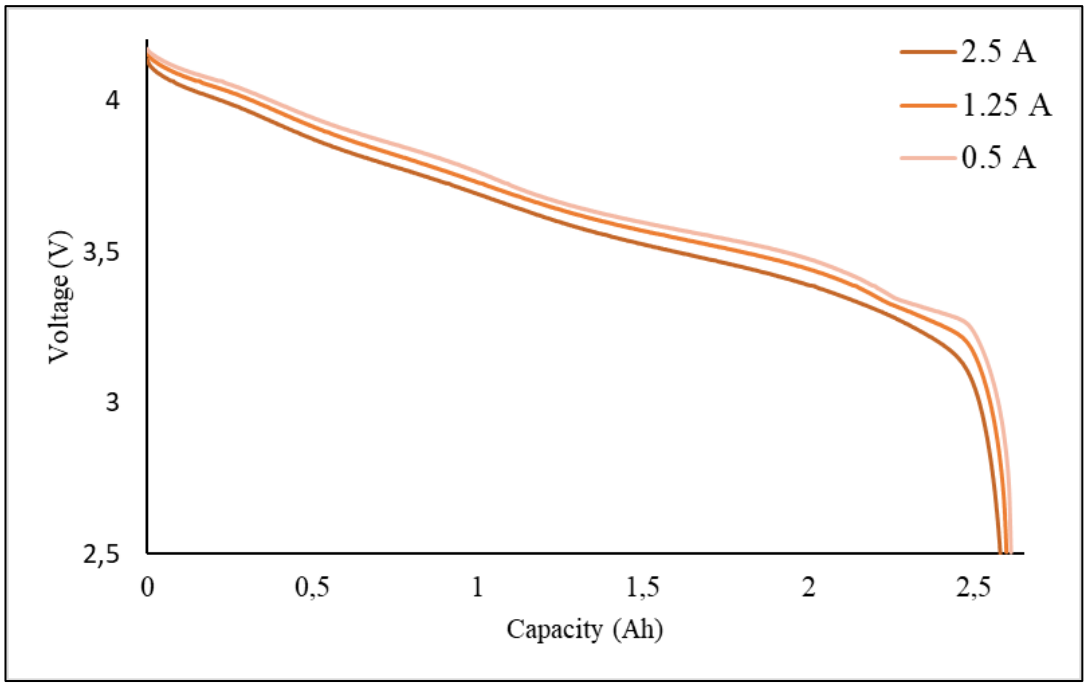

Figure 3.9. Experimental discharge curves of the battery with different current flow rates at 40 °C.

3.1.3. Pulse Tests

Pulse tests were carried out using ARBIN BT2000 Battery Tester and Nüve Climate Chamber with the desired pulse current discharge rate and in a controlled temperature environment in order to calculate the SoC of the battery. These tests were repeated at three different temperatures to fully charged batteries with the application of 20 pulses with 90 minutes relaxation times until the cut-off voltage limit with 2.5 A discharge current. The experimental results are shown in Figure 3.10., Figure 3.11. and Figure 3.12. for 0 °C, 25 °C and 40 °C respectively.

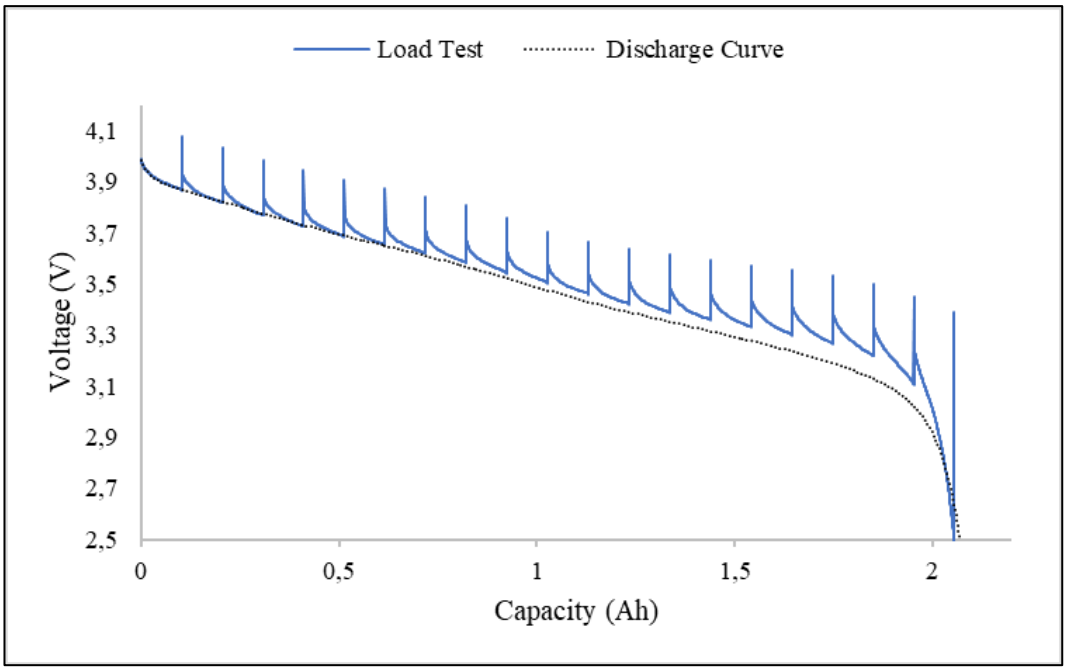

Figure 3.10. Pulse test of the battery at 0 °C.

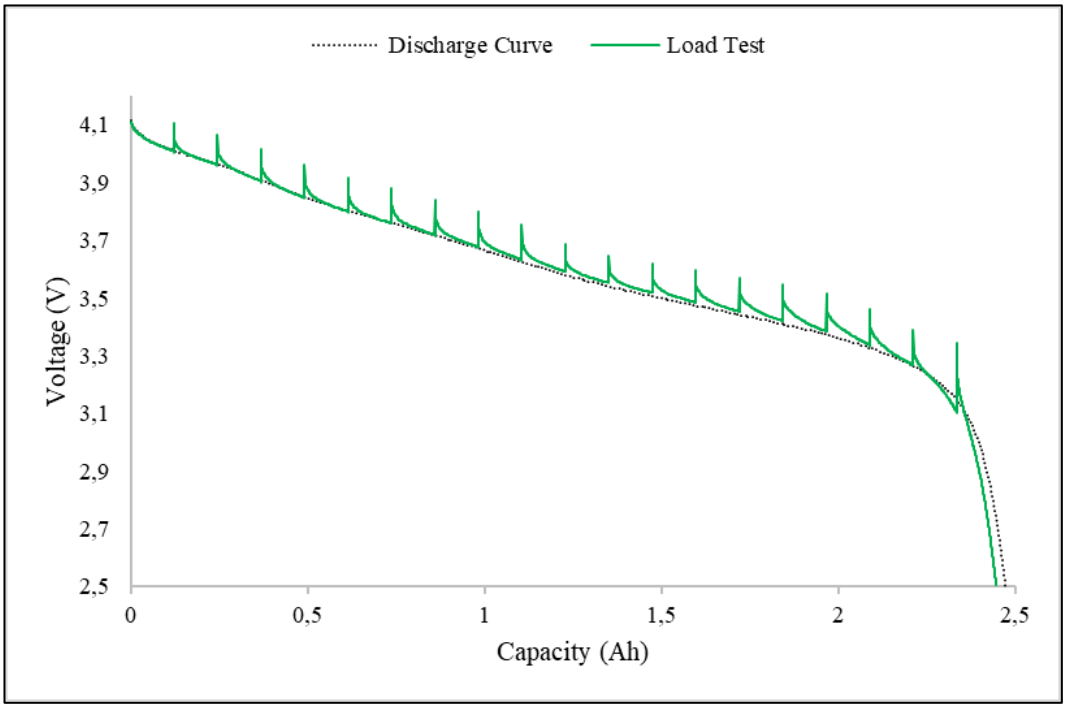

Figure 3.11. Pulse test of the battery at 25 °C.

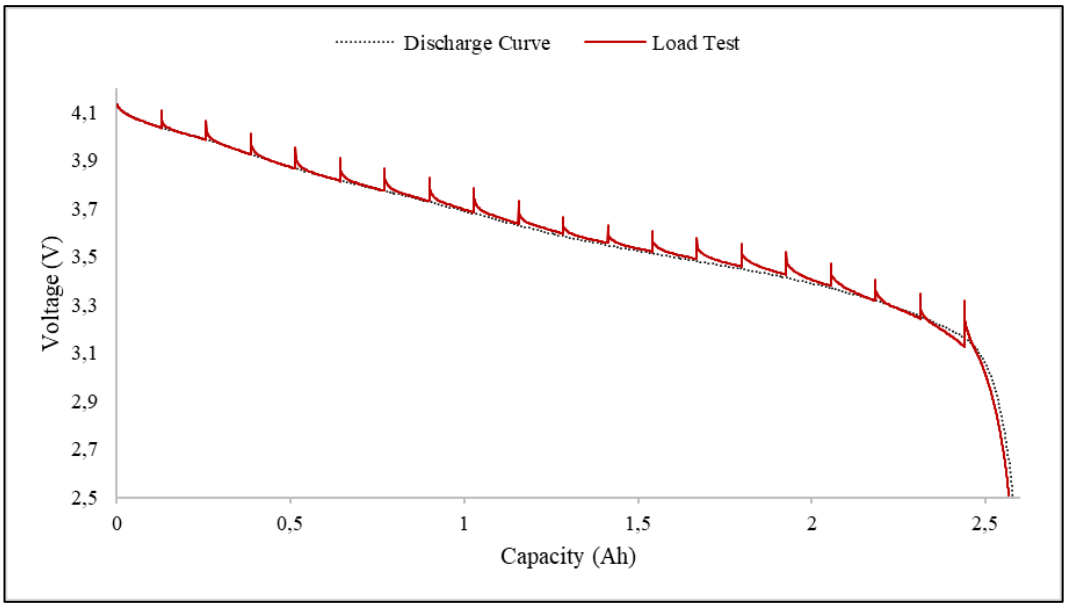

Figure 3.12. Pulse test of the battery at 40 °C.

3.2. Electrochemical Impedance Measurements

3.2.1. EIS Measurements of Kokam SLPB75106100 Pouch Type Battery

EIS measurements were performed by GAMRY 5000E Interface Potentiostat/Galvanostat/Zero-Resistance-Ammeter in Nüve climate chamber at 1atm atmospheric pressure and 25 °C for Kokam 7.5 Ah SLPB75106100 batteries. The battery was prepared for the tests by cleaning of the tabs with ethyl alcohol in order to eliminate the connection resistance and put into Faraday cage to get rid of electrical noise. As described in Section 2, EIS measurements could be performed by either applying voltage or current. For this study, potentiostatic mode was used by the application of 5 mV/s sinusoidal voltage to fully charged battery. Frequency range for the measurements were chosen between 100 kHz to 10 mHz in order to obtain useful data for the model. The experimental results are shown in Figure 3.13. and Figure 3.14.

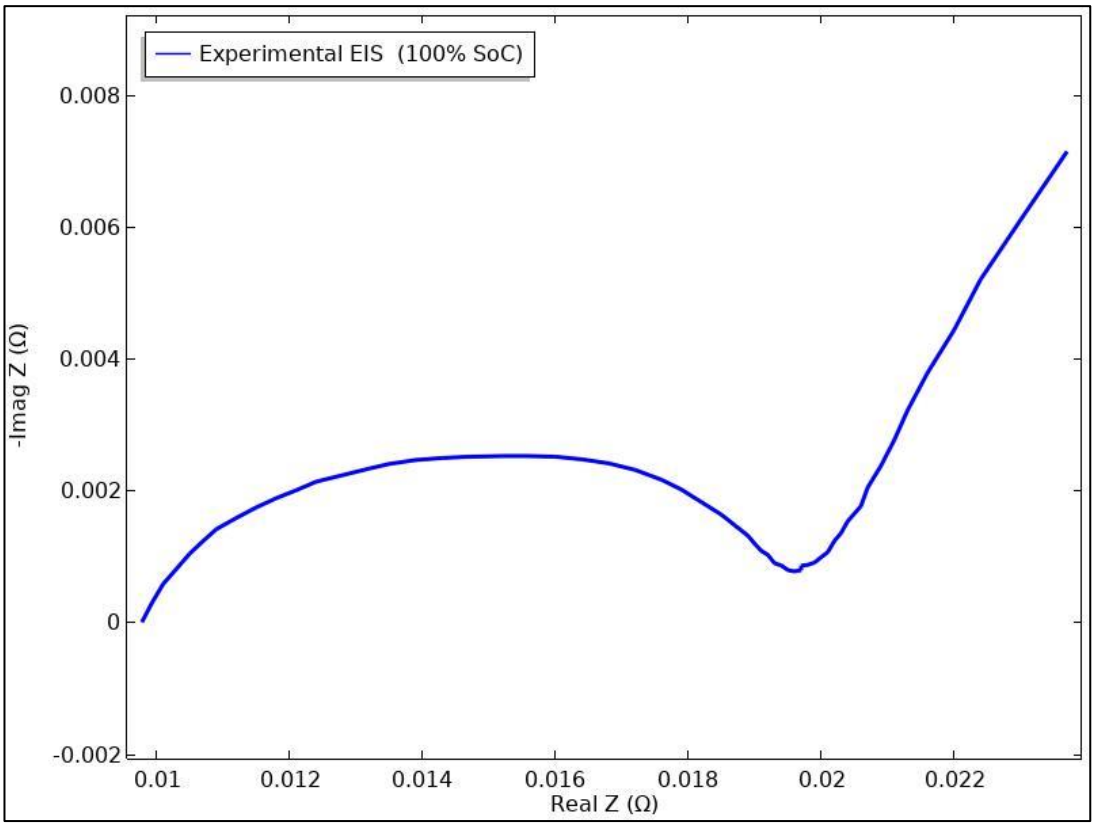

Figure 3.13. Nyquist plot of experimental data of EIS of fully charged LIB.

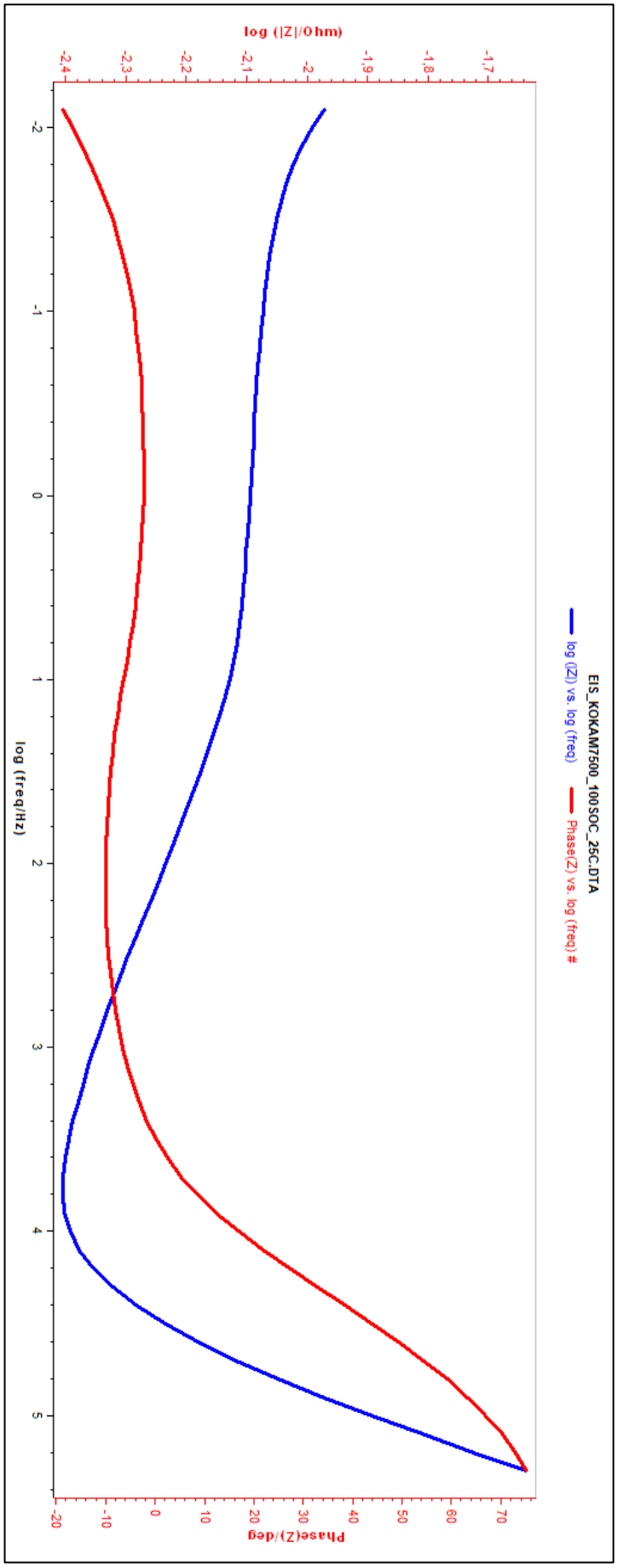

Figure 3.14. Bode representation of the impedance spectra of studied LIB.

3.2.2. EIS Measurements of SONY Murata 18650 Cylindrical Type Battery

Electrochemical impedance measurements were performed with the frequency range between 100 kHz – 10 mHz and 5 mV/s scanning rate in different state of charges of the batteries at different ambient temperatures with GAMRY 5000E Interface instrument. State of charge of the lithium ion battery isn't related with open circuit potential directly. Therefore, in order to calculate the state of charge, battery's voltage-capacity graphs are obtained from discharge tests and discharge load tests. While Figure 3.15., Figure 3.16. and Figure 3.17. shows the change in impedance in each SoC at 0 °C, 25 °C and 40 °C respectively, Figure 3.18. represents the temperature dependence of EIS on Nyquist plots for each SoC.

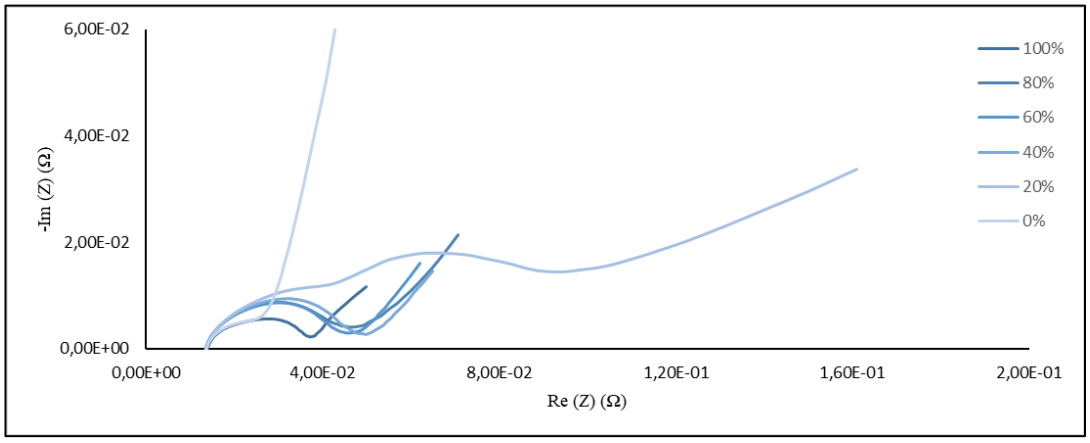

Figure 3.15. EIS of the battery for each SoC at 0 °C.

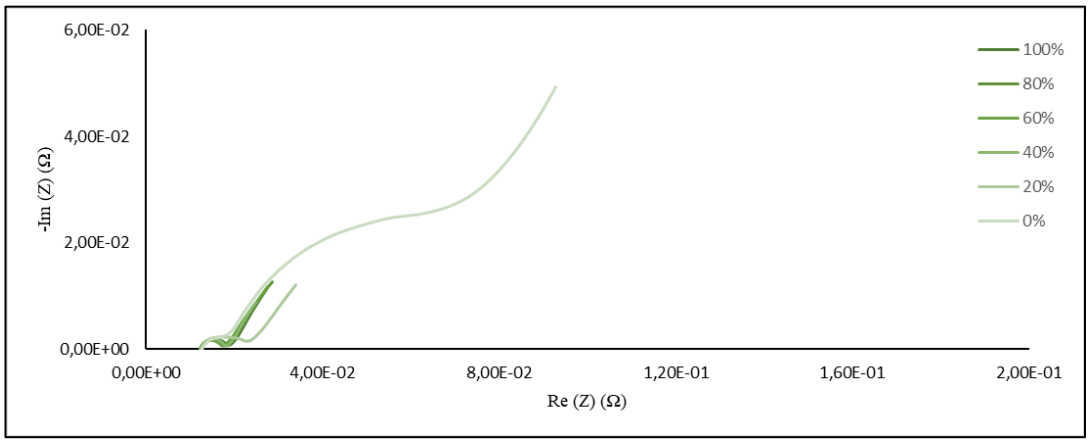

Figure 3.16. EIS of the battery for each SoC at 25 °C.

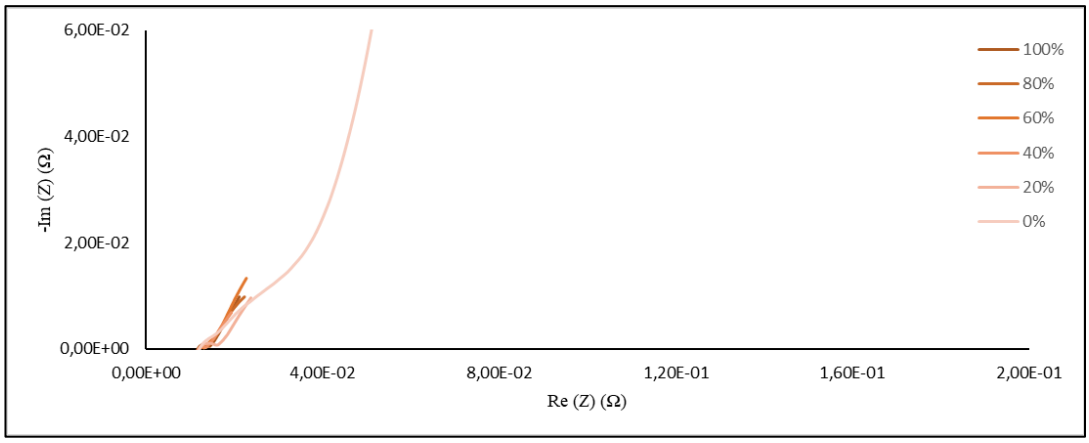

Figure 3.17. EIS of the battery for each SoC at 40 °C.

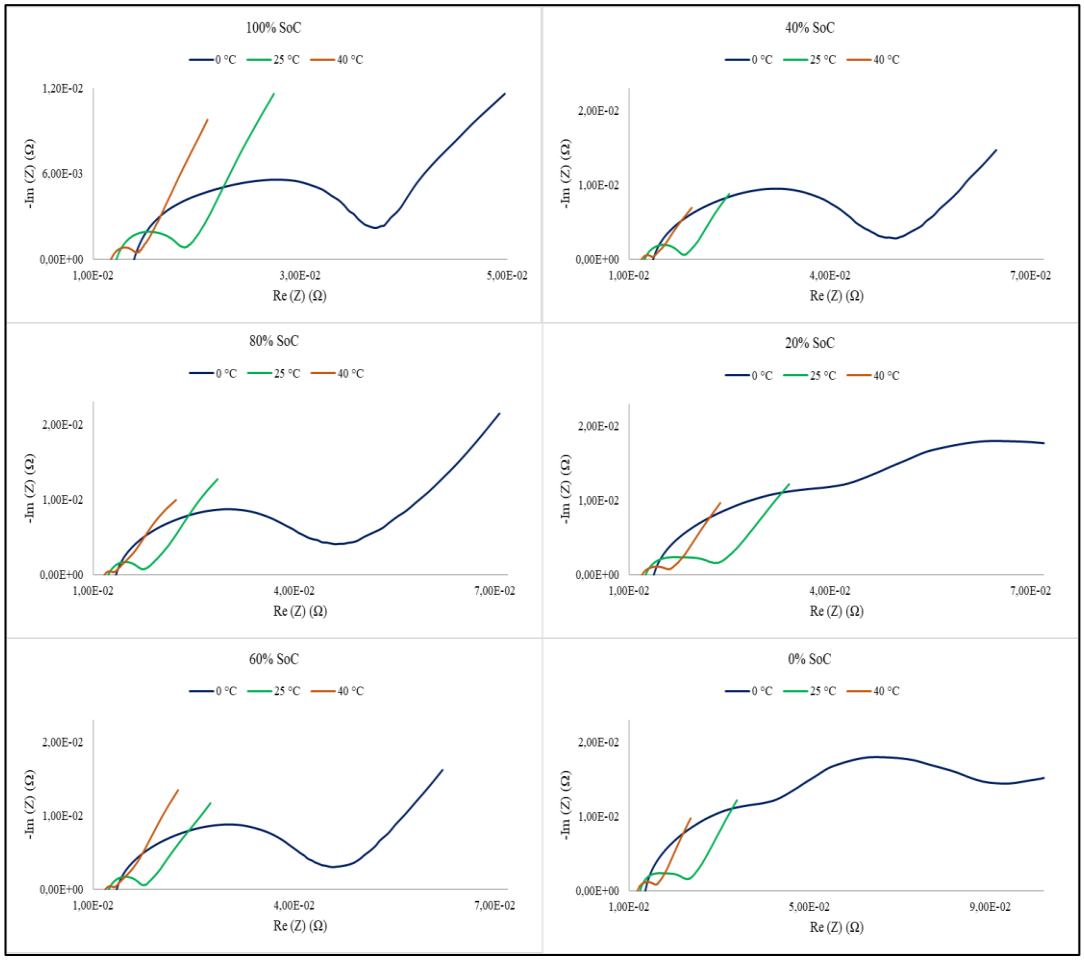

Figure 3.18. Temperature dependence of EIS for each SoC.

As the results show that temperature change has a great impact on the impedance spectra of the Li-ion battery. Therefore, in order to obtain how the change occurred regression analysis at 1 kHz for each SoC applied to the cells. The results showed that while the best fit had been occurred at 25 °C, the worst fit had been occurred in 0 °C.

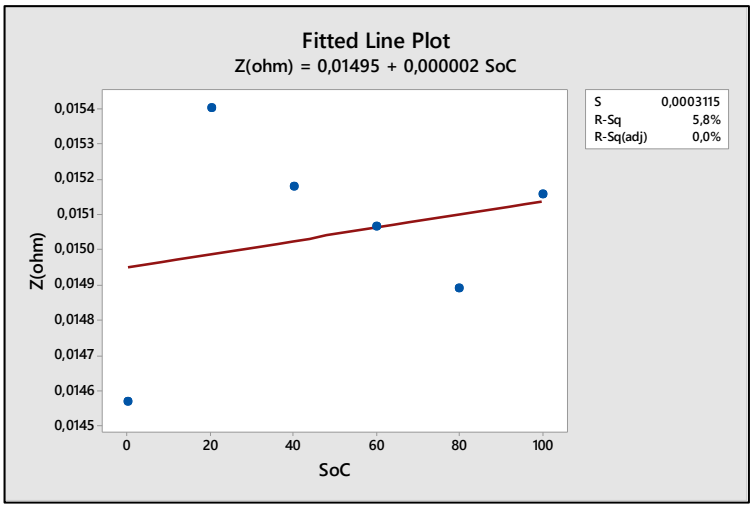

Figure 3.19. Regression analysis at 0 °C at the frequency of 1 kHz for each SoC.

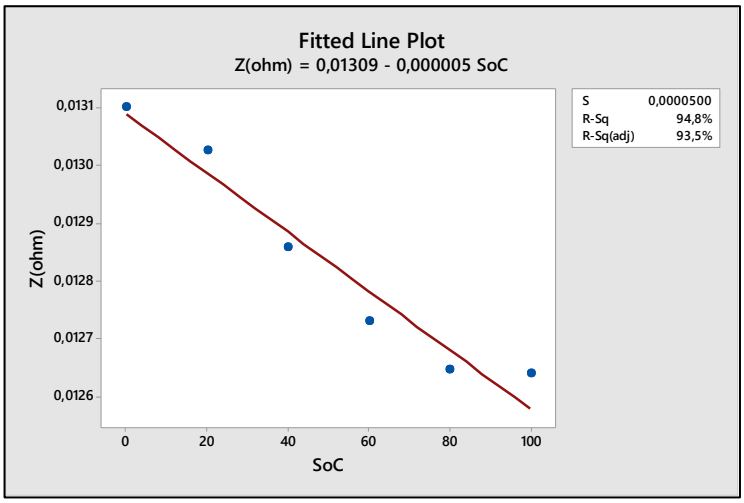

Figure 3.20. Regression analysis at 25 °C at the frequency of 1 kHz for each SoC.

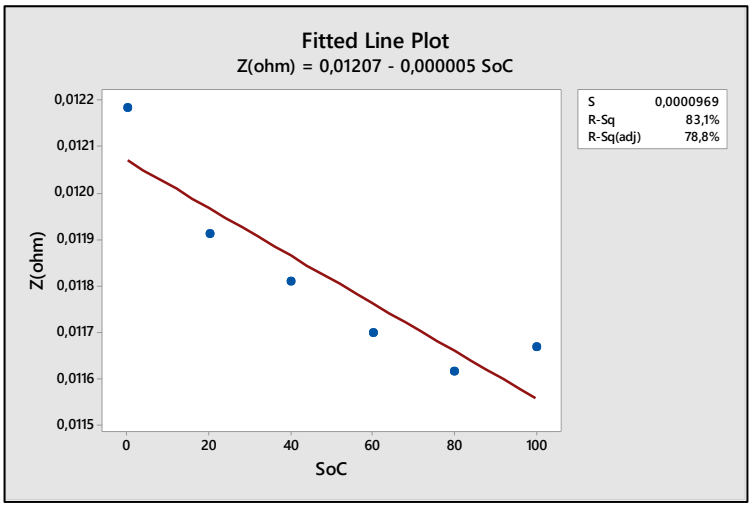

Figure 3.21. Regression analysis at 40 °C at the frequency of 1 kHz for each SoC.

Considering Figure 3.22. is the equivalent circuit of the impedance of the battery, the results showed that the ohmic resistance is dependent to temperature change but not SoC. On the other hand, SEI resistance is also dependent to temperature, but the change in SoC affects the SEI resistance while state of the battery is decreasing. Moreover, as the SoC decreases the second semi-circle of the impedance of the battery could be observed in Nyquist plot.

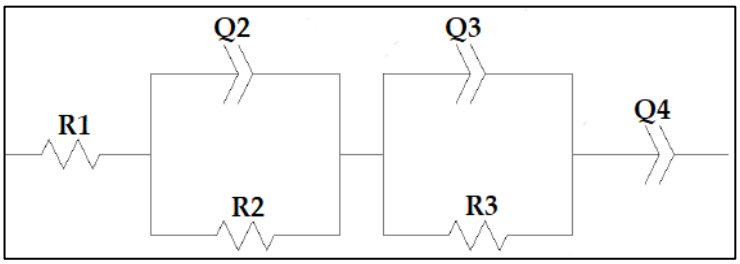

Figure 3.22. ECM of SONY Murata 18650 cylindrical type battery.

In the figure given above, R1 represents the ohmic resistance, R2-Q2 pair represents the first depressed semi-circle with constant-phase element represents the SEI film resistance, R3-Q3 pair represents the second depressed semi-circle which is associated with charge transfer kinetics and lastly Q4 represents the diffusion behavior of the battery in low-frequency range. As discussed in Chapter 2, constant phase element has a phase angle. The change in phase angle of Q4 is represented in Figure 3.29.

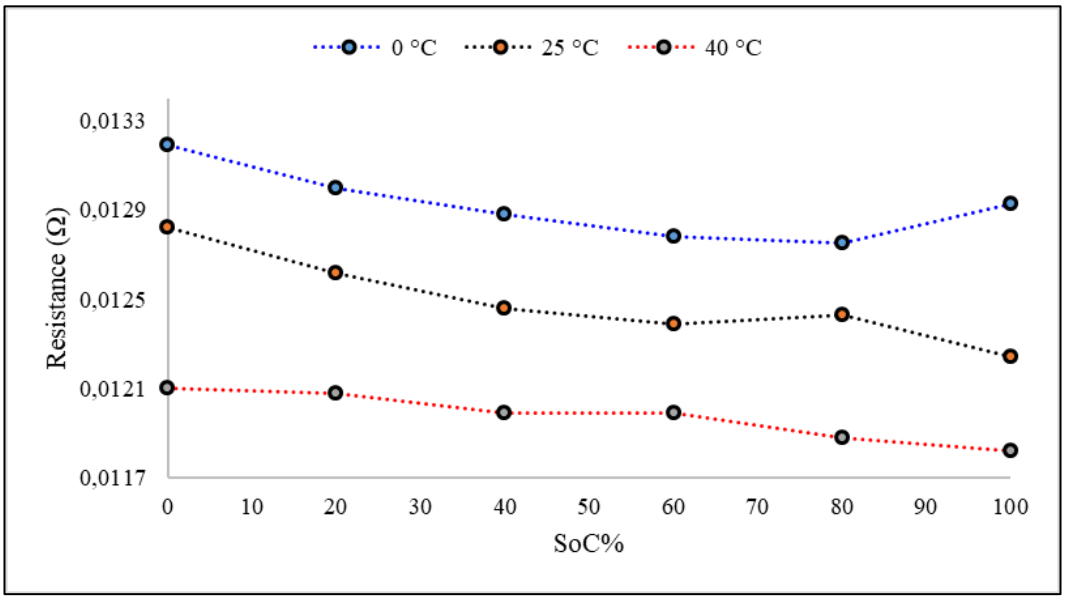

Figure 3.23. Change in R1 element of the battery.

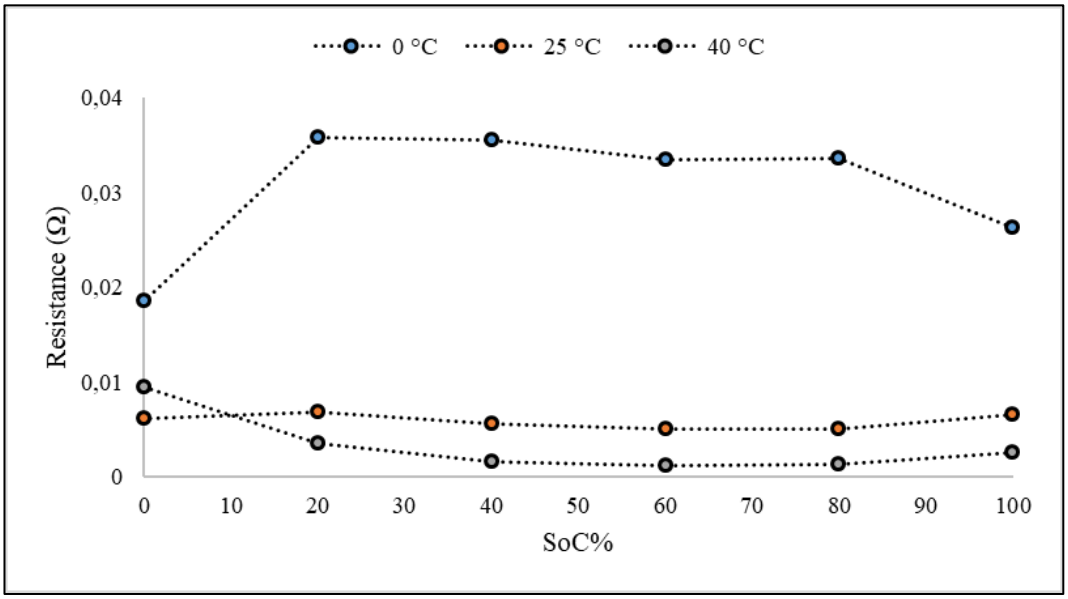

Figure 3.24. Change in R2 element of the battery.

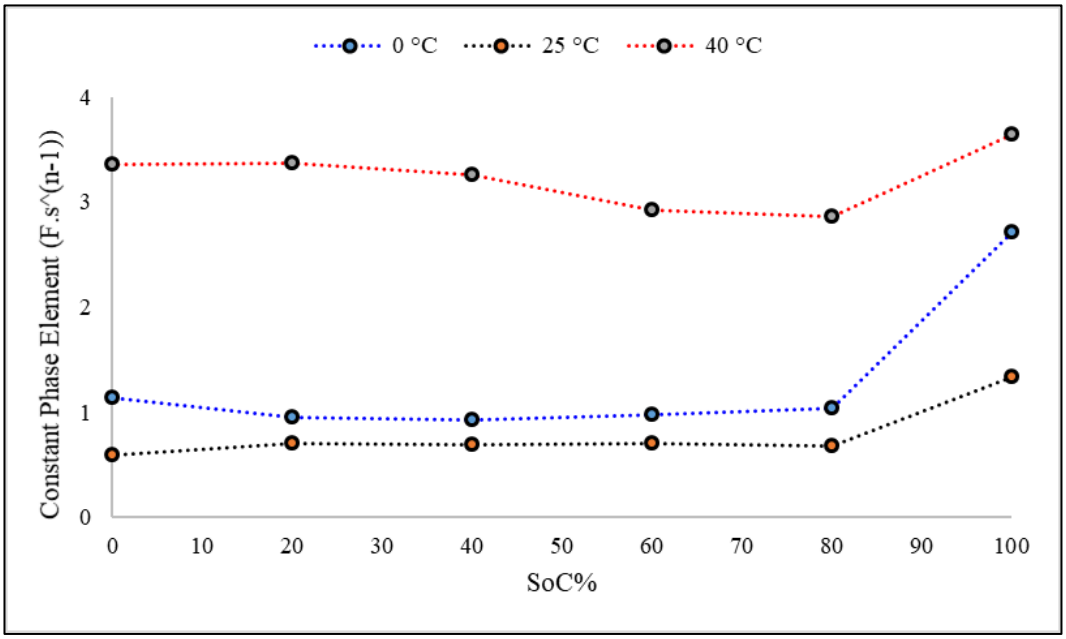

Figure 3.25. Change in Q2 element of the battery.

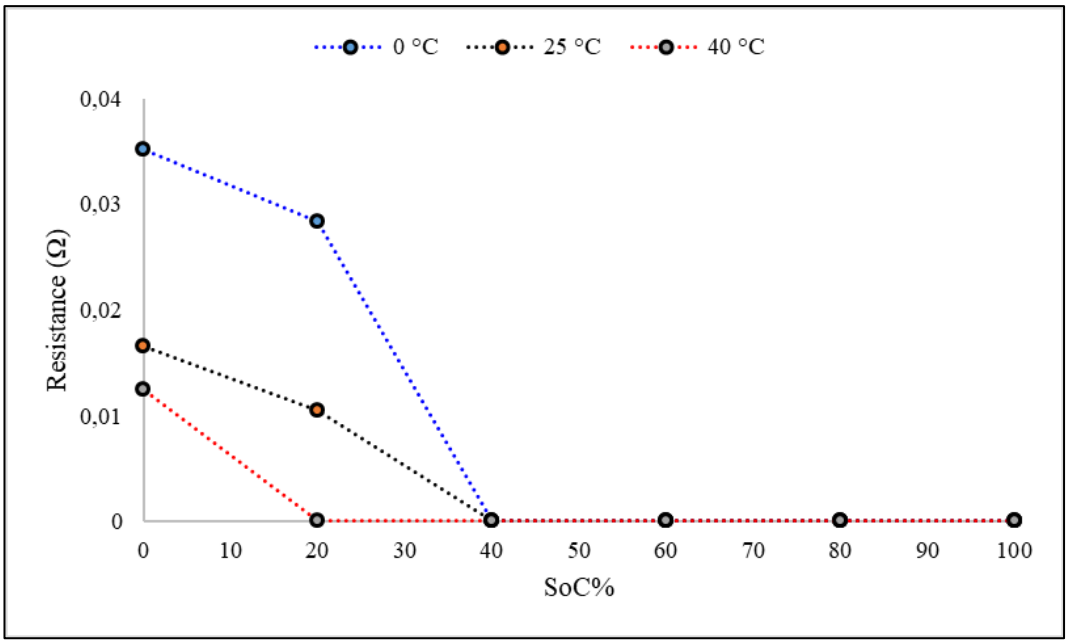

Figure 3.26. Change in R3 element of the battery.

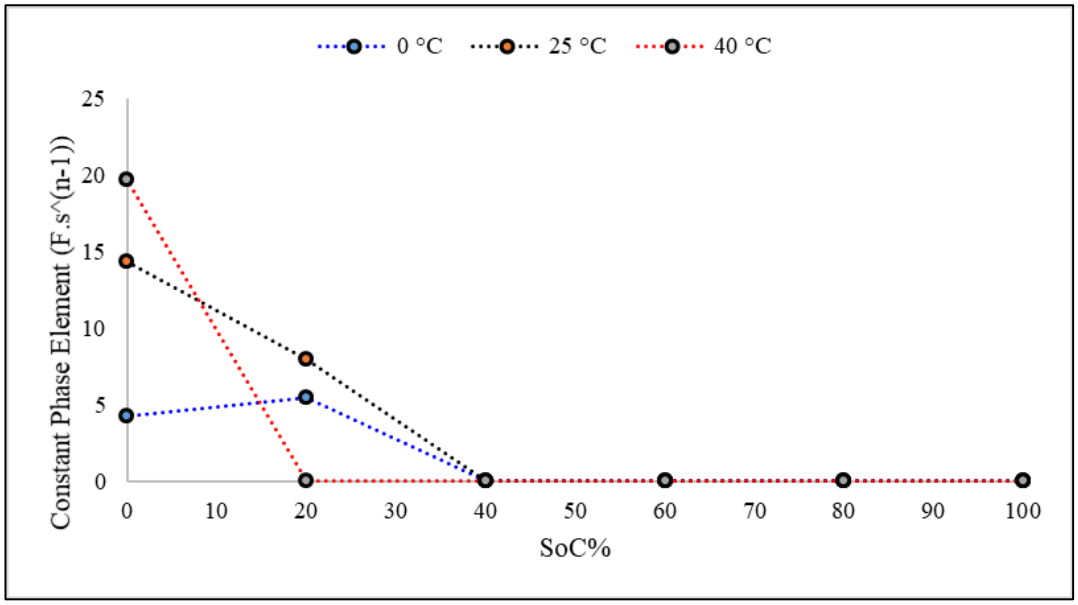

Figure 3.27. Change in Q3 element of the battery.

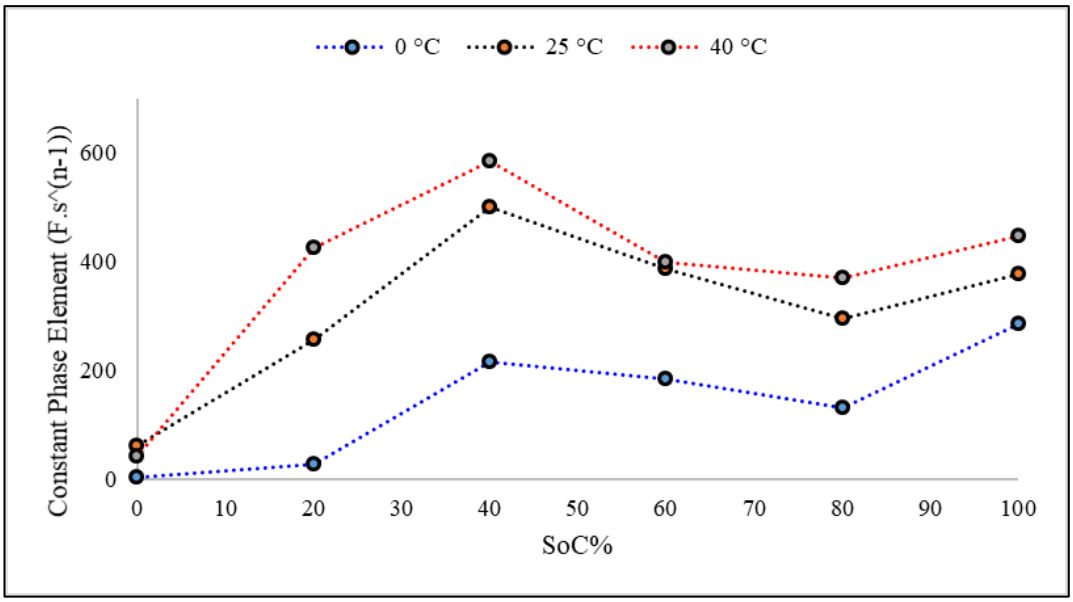

Figure 3.28. Change in Q4 element of the battery.

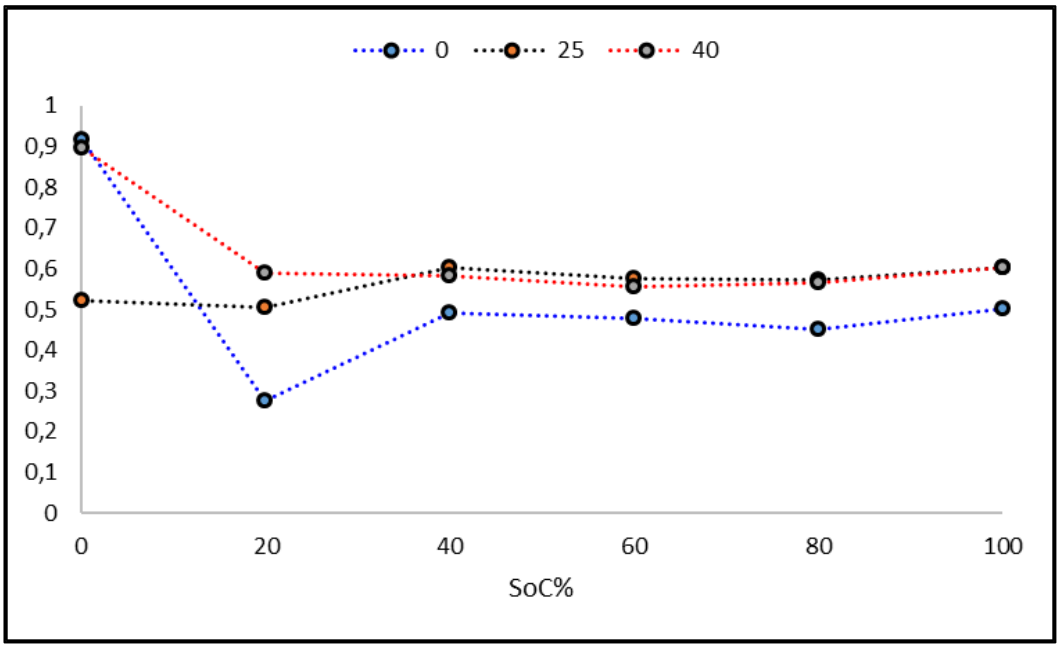

Figure 3.29. Phase angle of Q4 of the battery.

4. MODEL DESCRIPTION

A one-dimensional time-dependent model with multi-scale multi-domain (MSMD) approach [75] based on porous electrode theory developed by Newman et al. [45] of a lithium-ion pouch cell and the one-dimensional stationary frequency-domain perturbated impedance model will be introduced in this chapter.

4.1. Multi-Scale Multi-Domain Approach

Since the complexity of materials, components, kinetics or reactions take place in multi-physics problems, MSMD approach developed by National Renewable Energy Laboratory [75] had been applied to reduce the empirical assumptions. MSMD approach to modeling provides to derive solutions and transfer information domain-to-domain in multi-physics-based models.

Due to the non-linearities of reaction mechanism and transport processes in LIBs, MSMD approach had been used in this study to increase the model accuracy and investigate the dynamic behavior of the system. For example, while the Lithium intercalation/deintercalation process occurring in LIBs in nanoscale, charge transfer or mass transfer can be observed in the cell domain. Therefore, the nanoscale and microscale impact on LIB's dynamics should be considered. Moreover, the electrochemical reactions occurring in the cell can be observed in nanoseconds, charge transfer or ion transfer can be observed in seconds. Additionally, the change in electrode composition or degradation of structure or component could be observed from hours to months [76]. While thermodynamic properties and Lattice stability can be obtained from atomic material scale modeling, Li^+ diffusion, mass and charge balance can be solved in the cell scale. The electronic potential, current distribution and also heat generation for the system can be solved in the battery scale. Besides, thermal management, safety control or electrical intercell configuration can be obtained in the module scale. Figure 4.1. shows the MSMD character of a batteries.

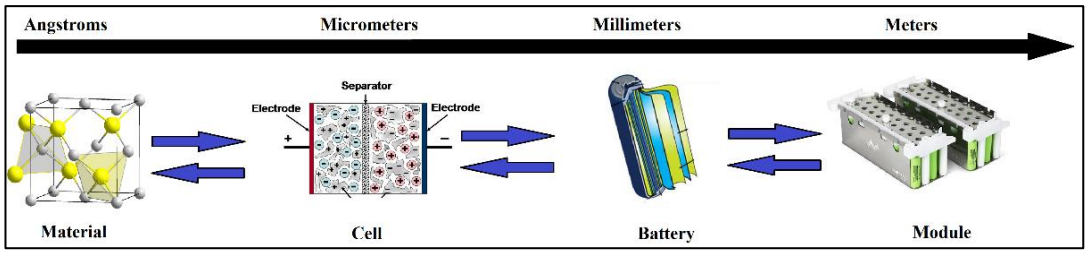

Figure 4.1. Representation of MSMD character of a batteries.

In this study, LIB model derives the solutions in three domains which are particle domain for solving collective responses of particles ionically or electrically connected, cell domain for characterizing the particle domain and battery domain for solving the response of single cell as well as the battery based on porous electrode theory. This modeling is known as the Doyle-Fuller-Newman (DFN) model or Pseudo two-dimensional (P2D) model due to the shape of the active particles in electrodes are assumed as spherical particles. Figure 4.2. shows the model hierarchy used in this study.

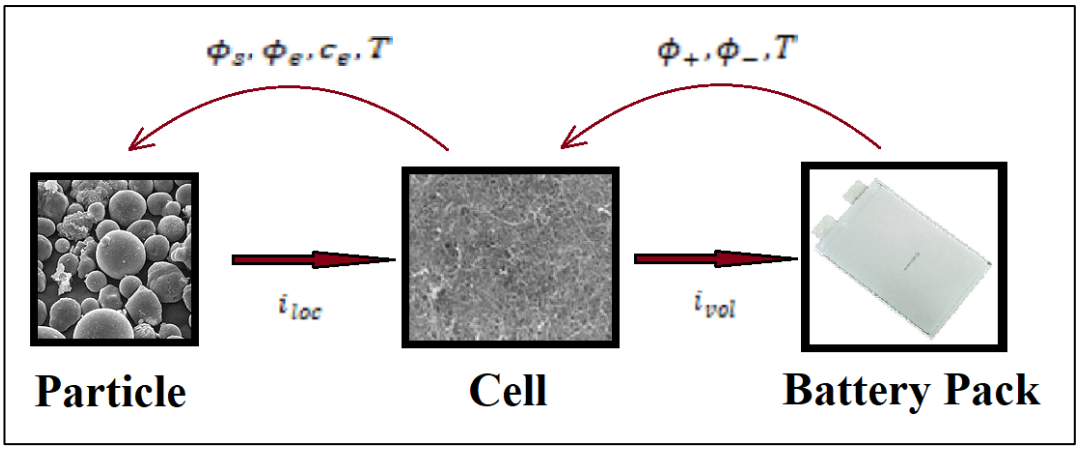

Figure 4.2. Model hierarchy.

4.2. Doyle-Fuller-Newman Model

The DFN model uses the Butler-Volmer kinetics for description of reaction mechanism, porous electrode mechanism and concentrated solution theories for characterization of charge and mass transfer occurring electrode-to-electrode in spherical coordinates.

In the particle domain, converting the Fick's second law into the spherical coordinates, lithium concentration on the surface of the electrodes can be obtained as assuming the model works with the spherical particles with neglecting the stress, assuming isotropic diffusion and the active material's conductivity is good. r_p represents the particle radius (μm) and $D_s(c_s)$ (m^2/s) denotes the solid material's concentration dependent diffusion behavior in the equation given below.

$$\frac{\partial c_s}{\partial t} = \nabla \cdot (D_s \nabla c_s) \tag{4.1}$$

$$\left.\frac{\partial c_s}{\partial r}\right|_{r=0} = 0 \tag{4.2}$$

$$\left.\frac{\partial c_s}{\partial r}\right|_{r=r_p} = -\frac{i_{loc}}{F} \tag{4.3}$$

Above, $\frac{\partial c_s}{\partial t}$ represents the change in solid-state concentration within time and D_s represents the diffusivity of the solid material. Also, $\frac{\partial c_s}{\partial r}$ represents the change in solid-state concentration with respect to particle radius. As shown in the Eq. (4.3), ion flux $-\frac{i_{loc}}{F}$ take place in the surface of the particles. i_{loc} denotes the local current density and F represents the Faraday constant.

In the cell domain, the governing equations are resolved in electrolyte, electrode and the interface sub-domains.

In the electrolyte sub-domain, change in lithium concentration within the electrolyte can be evaluated by using Stefan-Maxwell diffusion equation [77] by applying the mass and charge continuity. In addition, the formulation given below is the key factor to understand the interaction between the ions in the electrolyte solution for battery systems.

$$\frac{dc_l}{dt} = \frac{1}{\varepsilon} \cdot \nabla\left(D_{e,eff} \cdot \nabla c_l\right) + \alpha \cdot \frac{1 - t_0^+}{F \cdot \varepsilon} \cdot i_{loc} \tag{4.4}$$

$$D_{e,eff} = D_e \cdot \frac{\varepsilon}{\kappa} \tag{4.5}$$

Here, effective chemical diffusion constant of the electrolyte $D_{e,eff}$ is used due to the porous structure of the electrode material and α represents the ratio of the contact area and the volume between the electrode and electrolyte. And the change in lithium concentration c_e with respect to time is given below where the flux at the current collectors are zero:

$$\left.\frac{dc_l}{dt}\right|_{L=0\ and\ L=L} = 0 \tag{4.6}$$

The electrolyte-phase potential ϕ_l can be calculated as below:

$$\nabla\phi_l = \frac{i_l}{\sigma_{e,eff}} + \frac{R \cdot T}{z \cdot F} \cdot (1 - t_0^+) \cdot \nabla \ln (c_l) \tag{4.7}$$

$$\sigma_{e,eff} = \sigma_e \frac{\varepsilon}{\kappa} \tag{4.8}$$

The ratio between the current density i_l and the effective ionic conductivity $\sigma_{e,eff}$ shows the potential drop and the second term describes the concentration overpotential which is dependent on the gradients in the electrolyte. The value z is the charge number and it equals to 1 in LIBs and t_0^+ is responsible for the transport number for Li^+ in the electrolyte in other words, relative migration current of Li^+ with respect to the total migration current. While calculating the effective conductivity, the ratio between the porosity ε and the tortuosity κ is important due to the porous structures of the electrodes.

In the electrode sub-domain, the governing equations are:

$$\nabla \cdot i_s = a_v i_{loc} \tag{4.9}$$

Based on Ohm's Law, the solid-phase potential can be determined as following with the rate between the ionic conductivity σ_s and the current density i_s.

$$i_s = -\sigma_s \cdot \nabla\phi_s \tag{4.10}$$

In the interface sub-domain based on Butler-Volmer equation, which is the driver equation of electrochemical reactions occurring in a battery, the relation between the charge transfer current and exchange current density and the reaction overpotential can be calculated as following:

$$i_{loc} = i_0 \cdot \left(exp\left[\frac{\alpha_{A,C} \cdot z \cdot F}{R \cdot T}\right] - exp\left[-\frac{\alpha_{C,A} \cdot z \cdot F}{R \cdot T}\right]\right) \cdot \eta_D \tag{4.11}$$

And lithium material insertion occurs in both positive and negative electrodes. Hence, the exchange current density i_0 can be calculated as:

$$i_0 = F \cdot k_0 \cdot \left(\frac{c_{s,max} - c_{s,init}}{c_{s,max} - c_{s,ref}}\right)^{\alpha_A} \cdot \left(\frac{c_{s,init}}{c_{s,ref}}\right)^{\alpha_C} \cdot \left(\frac{c_l}{c_{l,ref}}\right)^{\alpha_A} \tag{4.12}$$

$$c_{s,ref} = \frac{c_{s,max}}{2} \tag{4.13}$$

While F represents the Faraday constant, k_0 is responsible for the reaction rate coefficient in the units of m/s, c_l and $c_{l,ref}$ denotes the salt concentration of the electrolyte and initial salt concentration of the electrolyte ($1000\ mol/m^3$) in the units of mol/m^3. α_A and α_C are the unitless anodic and cathodic transfer coefficients and $a_A + \alpha_C = 1$ [13].

The reaction overpotential η_D can be calculated by using the following equations:

$$\eta_D = \phi_s - \phi_l - \phi_{s,film} \tag{4.14}$$

ϕ_s denotes the solid-phase potential, ϕ_l represents the potential in the electrolyte solution and $\phi_{s,film}$ represents the effect of the SEI layer.

$$\phi_{s,film} = i_{loc} \cdot R_{film} \tag{4.19}$$

In the battery domain the governing equations are:

$$\nabla \cdot \left(-\sigma_{-,av} \nabla \phi_{-}\right) = -a_v i_{loc} \tag{4.15}$$

$$\nabla \cdot \left(-\sigma_{+,av} \nabla \phi_{+}\right) = a_v i_{loc} \tag{4.16}$$

For the development of the impedance modeling transformation of the equations from time-domain to frequency domain had been evaluated. In addition, a harmonic sinusoidal potential perturbation had been occupied and the experimental frequency range ($1\ kHz - 10\ mHz$) had been used for the impedance analysis.

$$\phi_s = \phi_{s,boundary} + \Delta\phi_s e^{-i\omega t} \tag{4.17}$$

Harmonic potential perturbation is denoted as $\Delta\phi_s e^{-i\omega t}$ in the units of V.

Double-layer capacitance values are modeled for both negative and positive electrodes by considering the porous matrix. Particle based are had been used as double-layer area.

$$i_{v,dl} = i_{dl} a_{v,dl} \tag{4.18}$$

$$i_{dl} = i\omega\left(\phi_s - \phi_l - \Delta\phi_{s,film}\right) C_{dl} \tag{4.19}$$

Above, $i_{v,dl}$ represents the volumetric current of the double-layer which can be evaluated by multiplying the double-layer capacitance value C_{dl} and charge transfer potential in the frequency domain, while $a_{v,dl}$ denotes the double-layer area of the associated electrode.

An additional porous electrode material had been occupied in the model in order to study the volumetric capacitance effects of the electronic conductors added to the positive electrode. As mentioned above, SEI film resistance of negative electrode had been included in the model in order to analyze the battery more accurate.

Finally, the ohmic resistance (current collectors' resistances, electrolyte resistance, the resistance of the oxidized layer of the battery tabs) had been inserted to the model as $R_{current}$.

4.3. Model Parameterization

The parameters had been obtained from experimental part of this study (see Chapter 3) and the experiments conducted by Ecker et al. [78] for Kokam SLPB75106100 high-energy commercially available pouch battery.

According to measurements conducted by Ecker et al. [78] the pouch-type Kokam battery had been disassembled carefully under argon atmosphere after discharging to 0% SoC with 1 C discharge current rate. It is observed that the battery consists of 2 single-sided, 23 double-sided NMC positive electrode sheet, 24 layers of double-sided graphite electrode sheets, current collectors and separators with $LiPF_6$ (LP-30) electrolyte solution. The parameter identification had been obtained from coin full cells with 16 mm diameter of negative and positive electrodes as well as 18 mm diameter of separator with 100 µl of LP-50 solution, coin half cells with 16 mm diameter of positive or negative electrodes assembled with 16 mm diameter of lithium foils and 18 mm diameter of separators with 100 µl of LP-50 solution. Furthermore, in order to obtain reference data Li-Li coin cells have been used with separators. Geometrical data used for the cell for the model introduced in Table 4.1.

Table 4.1. Geometrical data used for modeling.

	Sheet thickness (µm)	**Current collector thickness (µm)**	**Length (mm)**	**Width (mm)**	**Surface area (mm^2)**
Negative electrode	162	14.7	101	85	8585
Positive electrode	124	15.11	101	85	8585
Separator	19				

Calculation of charge state of battery provides the solid-state concentration information at the initial state for both of the electrodes. In order to obtain proper SoC data the electrochemical balance after the current application should be considered. As the ratio between the discharging time for a certain capacity and total discharging time gives the percentage of the SoC of the battery in constant current discharging process.

$$\%SoC = \frac{Capacity}{Total\ capacity} \times 100 = \frac{Test\ time}{Total\ test\ time} \times 100 \quad (4.20)$$

After the battery discharged until the certain charge state, relaxation i.e. no current flow in the battery should be applied for electrochemical balancing of the species. Finally, after the species balanced electrochemically, the ratio between the current solid-state concentration and maximum solid-state concentration equals to percentage of charge state of the cell.

$$\%SoC_{pos,neg} = \frac{c_{S,pos,neg}}{C_{s,max,pos,neg}} \times 100 \quad (4.21)$$

Another important parameter which is related with inhomogeneity of electrolyte solution due to the active particles inside of it is ionic conductivity of the electrolyte. Ionic conductivity is formulated as below which is strongly dependent on the salt concentration.

$$\sigma_e = 2.67c_l^3 - 12.98c_l^2 + 17.92c_l + 1.73 \quad (4.22)$$

Here, σ_e represents the ionic conductivity (mS/cm) and c_l denotes the electrolyte salt concentration (mol/dm^3) between the range of 0.5 mol/dm^3 and 1.5 mol/dm^3.

The transport number t^+ for the lithium ions inside the electrolyte has been derived by Nyman et al. (2008) [65] as 0.26 and the diffusion coefficient for the electrolyte has been calculated as $D_e = 2.44 \times 10^{-10}\ m^2/s$ by using the Einstein relation [79] as an approximation as following:

$$D_e = \frac{\sigma_e k_B T}{e^2 N_A c_l} \quad (4.23)$$

While D_e represents the diffusion coefficient of the electrolyte, k_B denotes the Boltzmann constant, N_A is the Avogadro constant, and lastly e is the elementary charge for 1 M electrolyte solution.

Electronic conductivity measurements for both negative and positive electrodes have the small error due to the unknown effects of current collectors and contact

resistance of the active materials. Moreover, the SEI layer formation over the graphite particles had been increased the measurement error in the negative electrode. However, Ecker et al. [78] claim that the measurements conducted by themselves are in the good accuracy with the literature. The electronic conductivities of the electrodes used in the system modeling are listed in Table 4.2.

Table 4.2. Electronic conductivities of the electrodes used in the model.

	Electronic conductivity (S/m)
Negative electrode	14
Positive electrode	68.1

Porosity, which determines strongly the system behavior, tortuosity factor that affects the rate of the chemical reactions and the particle radius of the electrodes and separator has been measured with Hg-porosimetry method. The values used in the model are listed in Table 4.3.

Table 4.3. Porosity, tortuosity factor and particle radius used in the model.

	Porosity (%)	**Tortuosity factor**	**Particle radius (µm)**
Negative electrode	32.9	2.03	10.5
Positive electrode	29.6	1.94	9 and 60
Separator	50.8	1.67	-

Maximum solid-phase concentration can be calculated using the ratio between the density and molecular weight of used material:

$$c_{s,max} = \frac{\rho}{M} \tag{4.24}$$

The initial lithium concentration of the positive electrode can be calculated as following:

$$c_{s,init,pos} = (1 - utilization) \cdot c_{s,max,pos} \tag{4.25}$$

The initial concentration of the Lithium in the negative electrode at the charged cell is also depends on the maximum solid-phase concentration, porosity and inactive part of the positive electrode and can be calculated as following:

$$c_{s,init,neg} = (utilization - C_{SEI}) \cdot c_{s,max,pos} \cdot \frac{V_{pos} \cdot (1 - \varepsilon_{pos}) \cdot (1 - inactive_{pos})}{V_{neg} \cdot (1 - \varepsilon_{neg})(1 - inactive_{neg})} \quad (4.26)$$

Above, ε represents the porosity of the material and V represents the volume of the coating of the electrode, $c_{s,max}, c_{s,init}, c_{s,ref}$ are responsible for the maximum solid-phase concentration, initial concentration, reference concentration of the studied electrode.

The concentration values are listed in Table 4.4. and reaction kinetics are tabulated in Table 4.5. both for positive and negative electrodes.

Table 4.4. Concentration values of the electrodes and electrolyte.

	Maximum solid-phase concentration (mol/m^3)	**Initial concentration (mol/m^3)**
Positive electrode	48580	11659
Negative electrode	31920	23332
Electrolyte	-	1000

Table 4.5. The values used in the model to identify the reaction kinetics.

	Anodic transfer coefficient	**Cathodic transfer coefficient**	**Reaction rate coefficient (m/s)**
Positive electrode	0.48	0.52	$8.158 \cdot 10^{-10}$
Negative electrode	0.48	0.52	$4.162 \cdot 10^{-10}$

Furthermore, the reaction surface of the electrodes assuming the spherical-particles relation can be identified as below. While S_r represents the reaction surface, $V_{electrode}$ is total electrode volume, $V_{particle}$ is the volume of the single particle and lastly, r_p is the Lithium particle radius of considered electrode.

$$S_r = \frac{V_{electrode} \cdot \varepsilon_{pos|neg} \cdot (1 - inactive_{pos|neg})}{V_{particle,pos|neg}} \cdot 4 \cdot \pi \cdot r_{p,pos|neg}^2 \quad (4.27)$$

Figure 4.3. [78] shows the particle size distribution in the electrode obtained by the help of Hg-porosimetry method. As in negative electrode, particle size distribution has two peek points at 9 and 60 μm, in positive electrode one peek point can be observed. The distribution in negative electrode leads to a consideration of a novel design method for the electrode. In other words, negative electrode can be considered as it has three domains, which are reacting, partially reacting and non-reacting particles related with the size. The bigger particles are considered as two domains which are partially reacting and not reacting particles, the smaller particles are considering as one domain of reacting particles as represented in Figure 4.4.

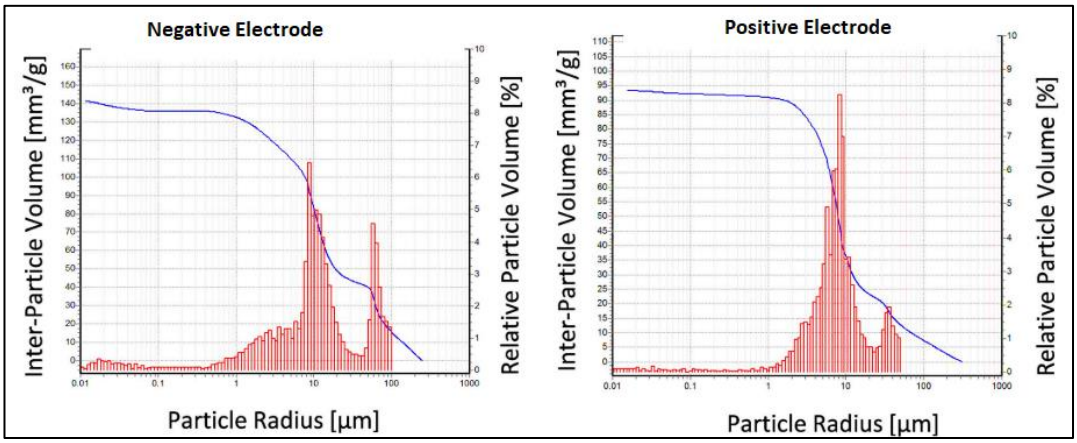

Figure 4.3. Particle size distribution in the electrodes obtained by Hg-porosimetry.

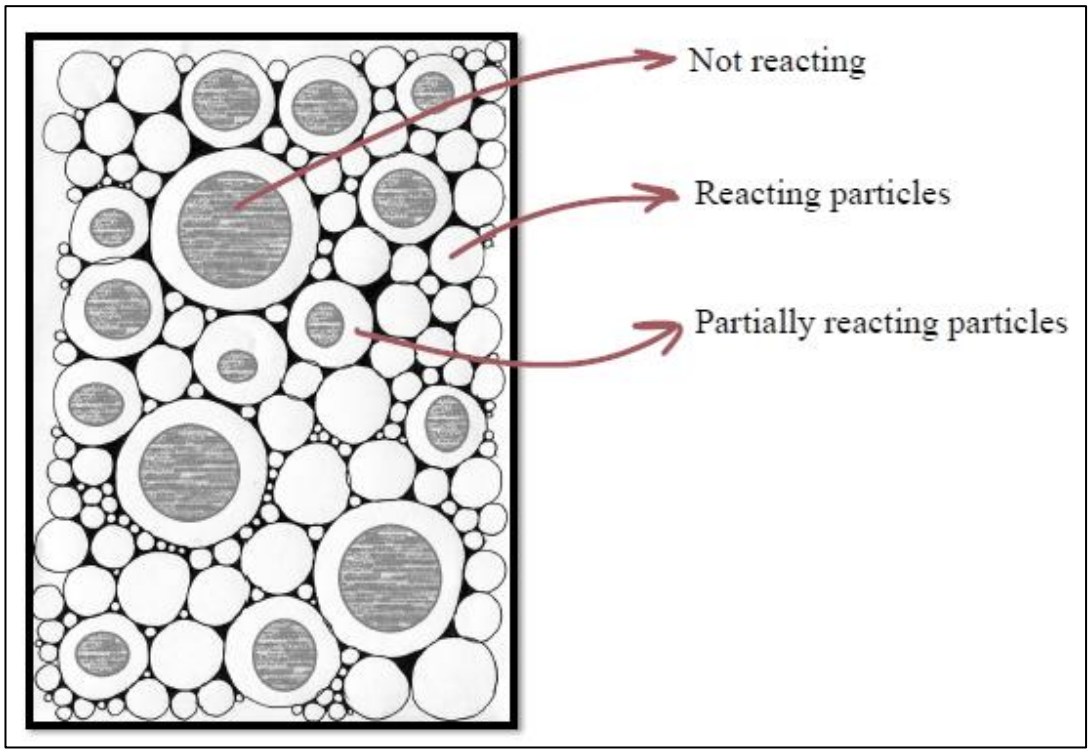

Figure 4.4. Proposed electrode model describing the domains.

The first charging process of the cell results with the formation of solid-electrolyte-interface (SEI) in the negative electrode and the utilization in the positive electrode. The reaction mechanism works with Li+ intercalation for both electrodes. During the particle intercalation at the first charge, some of the lithium particles are used in the positive electrode and the transferred particles generate the SEI layer in the negative electrode. Besides, investigation of SEI formation could provide meaningful interpretations about surface coating or gradient of the negative electrode material. Recent studies show that, EIS measurements could be very useful to analyze the SEI layer formation in order to increase the capacity of batteries [66].

Although SEI layer that bounds the lithium particles measured as 14% and the utilization for the positive electrode determined as around 74%, in the current model, the values of those parameters had been adjusted for a good fitting as shown below.

Table 4.6. SEI for the negative electrode and utilization for the positive electrode values for the model.

C_{SEI} (%)	**Utilization (%)**
8	76

Furthermore, a relation between the measured capacity and theoretical capacity of the cell provides a good estimation for the inactive part according to formula given below:

$$inactive\ part\ (\%) = \left(1 - \frac{C_{measured}}{C_{theoretical}}\right) \cdot 100 \tag{4.28}$$

$$C_{theoretical} = \frac{\rho \cdot V \cdot e \cdot (1 - \varepsilon) \cdot N_A}{M} \tag{4.29}$$

Here, ρ represents the material density (g/cm^3), M is the molar mass and ε is the porosity of the electrode material. N_A is the Avogadro's number. The results used in the model are tabulated in Table 4.7.

Table 4.7. Theoretical capacity, density, inactive part and molar mass values of the electrodes.

	$C_{theoretical}$ (C)	**Material density (kg/m^3)**	**Inactive part (%)**	**Molar Mass (g/mol)**
Positive electrode	798.28	4750	34	97.777
Negative electrode	771.66	2300	27.5	72.055

Equilibrium potentials both negative and positive electrodes have been obtained by measuring the OCVs of both coin half cells and coin full cells. The resulted graphs are shown for the negative electrode in Figure 4.5. and for the positive electrode in Figure 4.6. respectively. Considering the fully charged cell without any loss, while the initial SoC of positive electrode is almost 1, the SoC of negative electrode could be 0.

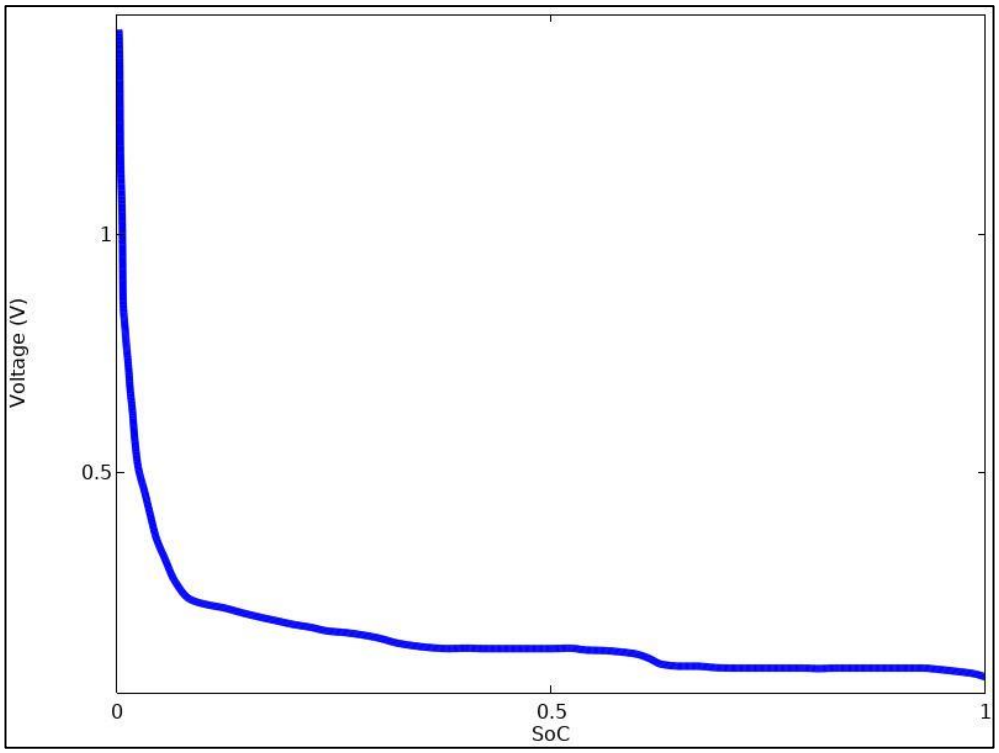

Figure 4.5. Equilibrium potential vs. SoC graph of the negative electrode.

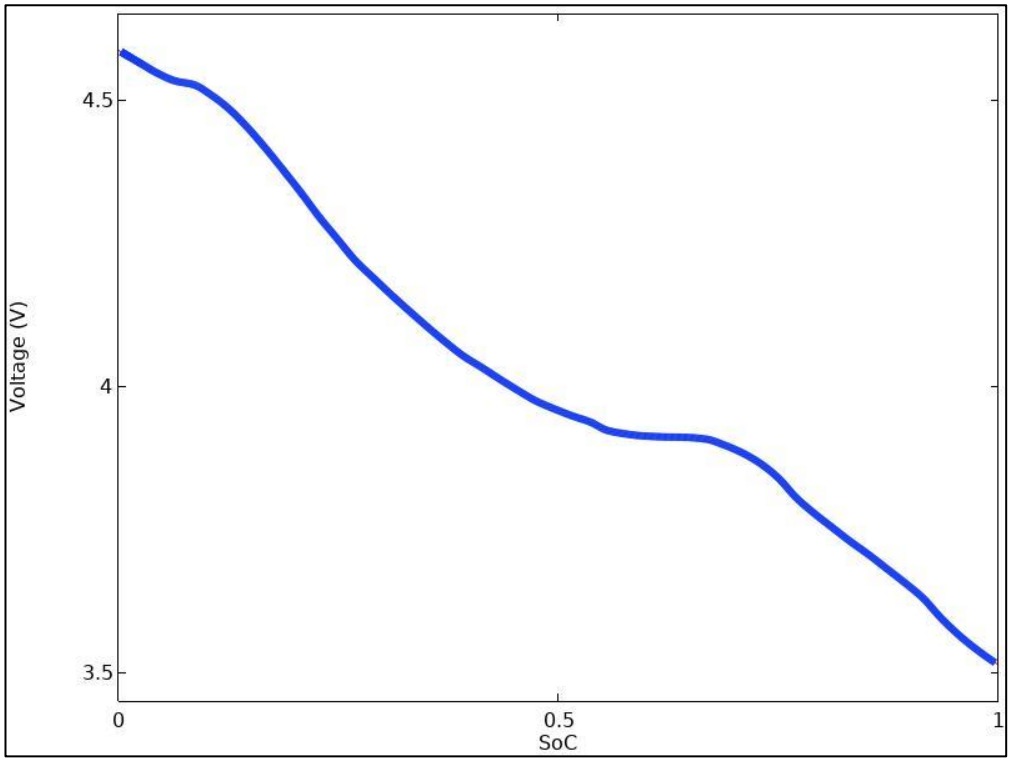

Figure 4.6. Equilibrium potential vs. SoC graph of the positive electrode.

Ecker et al. had been measured solid-state diffusion in the electrode material by using two methods, which are the GITT measurement and EIS measurement. Even if the electrode material is porous, assuming the uniform current distribution in order to parameterize the diffusion, the GITT method is appropriate for deriving the diffusion coefficient of the electrode material. By applying short currents to the battery i.e. exciting the battery in a specified SoC with the help of the Fick's law, the diffusion coefficient can be derived by measuring the IR drop in GITT method.

$$D_{GITT} = \frac{4 \cdot r_p^2}{\pi \cdot t} \cdot \frac{\Delta E_{eq}^2}{\Delta E_t} \tag{4.30}$$

Above, ΔE_{eq} is the change in equilibrium potential and E_t is the total change in the potential (IR drop is subtracted), r_p is the particle radius and t is the pulse duration.

In the EIS method, Warburg element has been considered in order to identify the diffusion coefficients for the coin cells. Diffusion coefficients obtained by Ecker et. al shown in Figure 4.7. for the positive and Figure 4.8. for the negative electrode respectively.

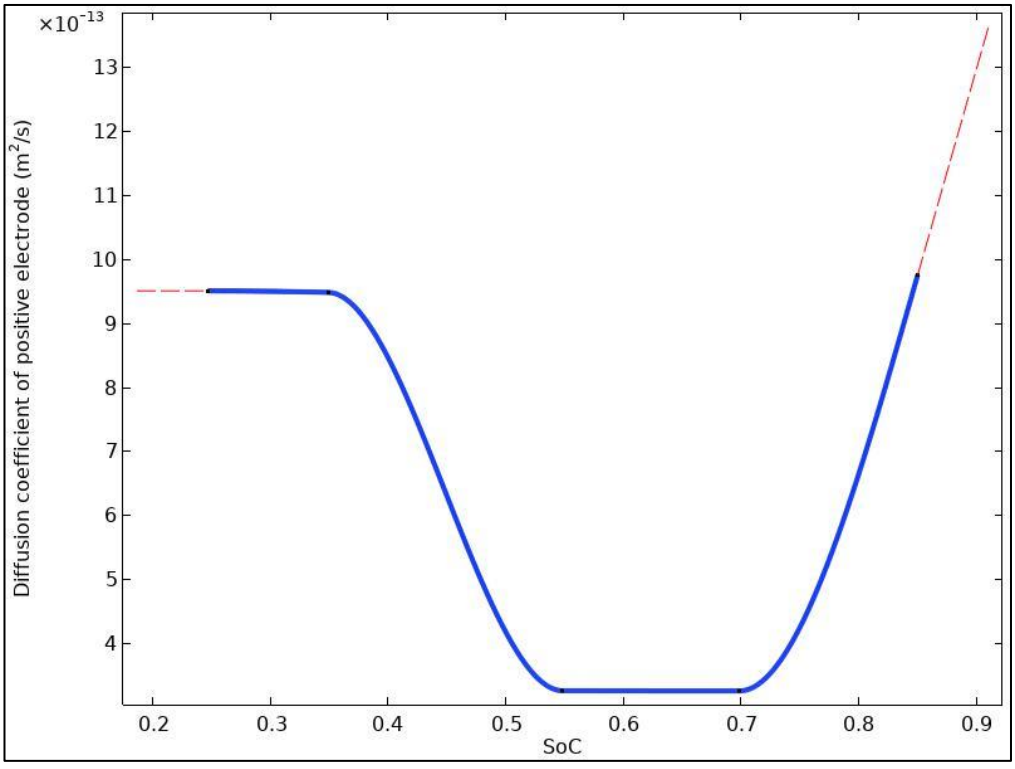

Figure 4.7. Diffusion coefficient of the positive electrode for the studied cell with respect to SoC.

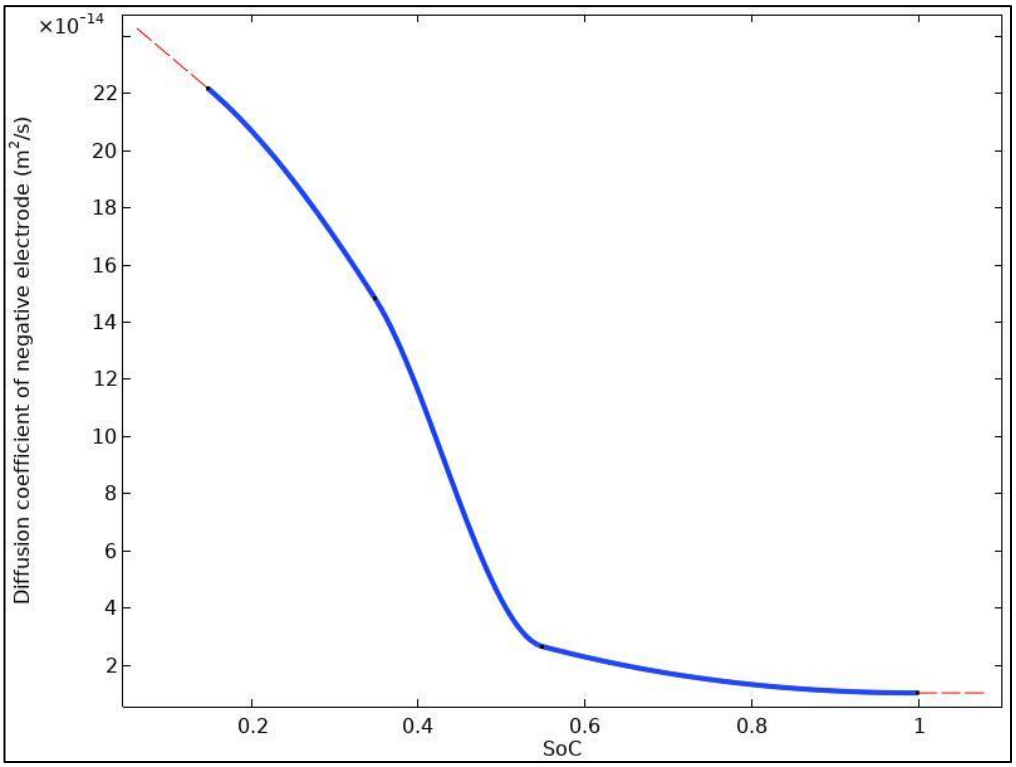

Figure 4.8. Diffusion coefficient of the negative electrode of the studied cell with respect to SoC.

The OCV characteristics of LIBs depends on the ambient temperature strongly. In order to simulate the temperature dependence of the battery Arrhenius equations are used for the ionic conductivity of the electrolyte, diffusion constants of both electrodes and electrolyte, and exchange current densities of the electrodes [78].

$$x(T) = x(T = 298.15\ [K]) \cdot e^{\frac{E_{a,x}}{R}\left(\frac{1}{298.15\ [K]} - \frac{1}{T}\right)} \tag{4.31}$$

In the Arrhenius equation given above, $x(T)$ denotes a temperature dependent parameter in a specific temperature, $x(T = 298.15\ [K])$ denotes the value of the temperature dependent parameter at ambient temperature and $E_{a,x}$ represents the activation energy of the parameter x. Lastly, T is the temperature in the units of Kelvin. Activation energies for the temperature dependent parameters are listed in Table 4.8. for the studied battery. Activation energies of the parameters had been measured by both GITT and EIS methods by Ecker et al. [78].

Table 4.8. Activation energies of the temperature dependent parameters.

Parameter	Activation energy [kJ/mol]
Diffusion coefficient of positive electrode	80.6
Diffusion coefficient of negative electrode	40.8
Diffusion coefficient of electrolyte	17.1
Exchange current density of positive electrode	43.6
Exchange current density of negative electrode	53.4
Ionic conductivity of electrolyte	17.1

In addition, exchange current densities for the positive and negative electrodes with respect to SoC of the battery are shown in the figures 4.9. and 4.10. respectively.

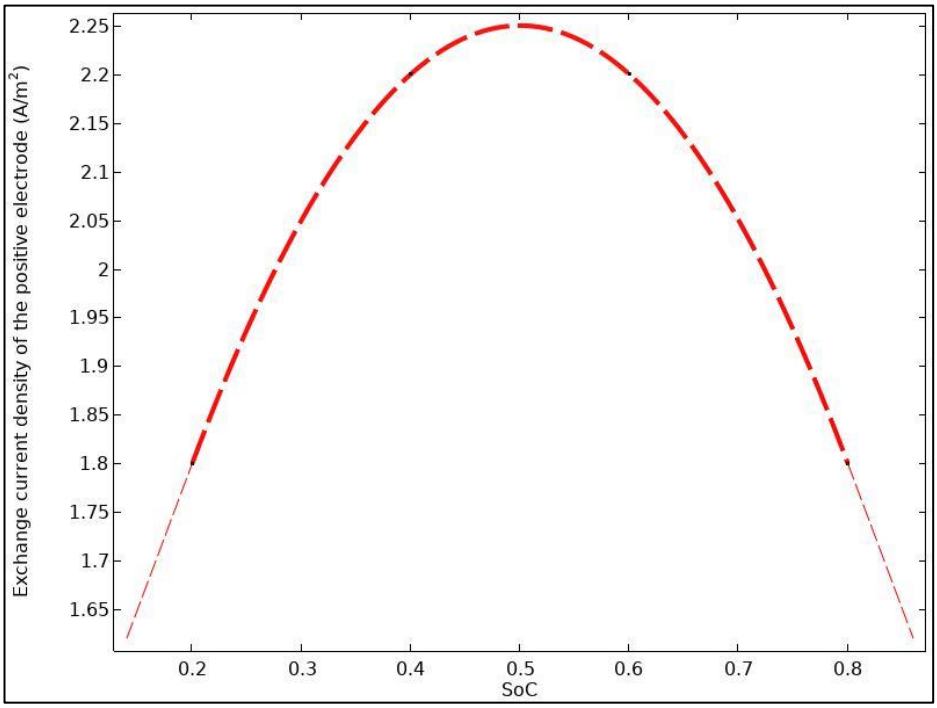

Figure 4.9. Exchange current density of the positive electrode with respect to SoC.

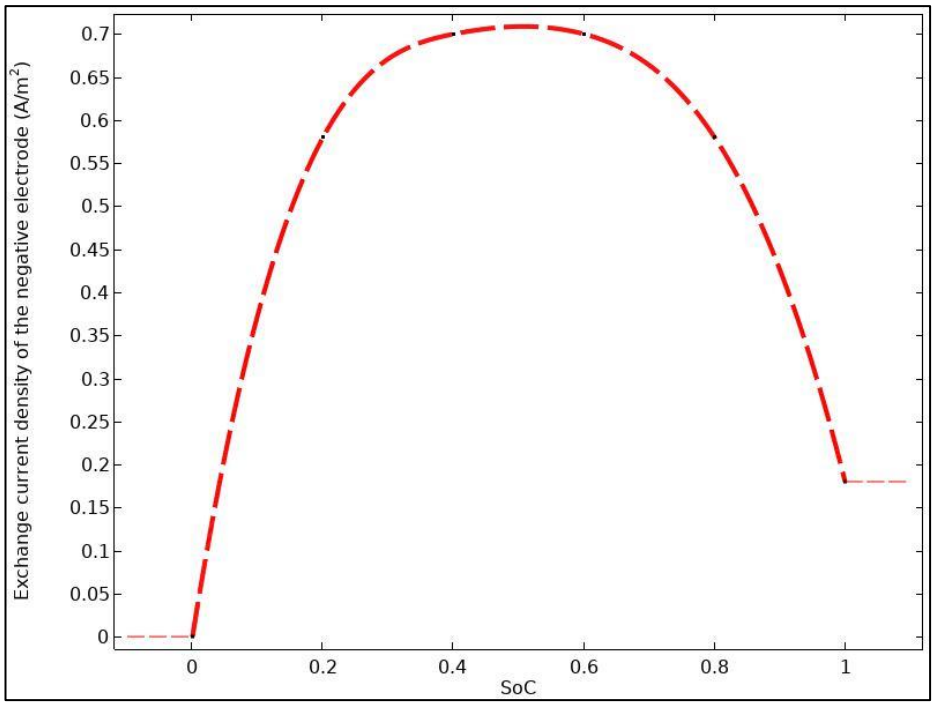

Figure 4.10. Exchange current density of the negative electrode with respect to SoC.

The resultant OCV model of the battery is shown in Figure 4.11. It can be observed that the regions that consist of higher non-linearities i.e. complicated reaction mechanism need minor arrangements. Hence, sensitivity analysis of the parameters and optimization process were considered to obtain more accurate model.

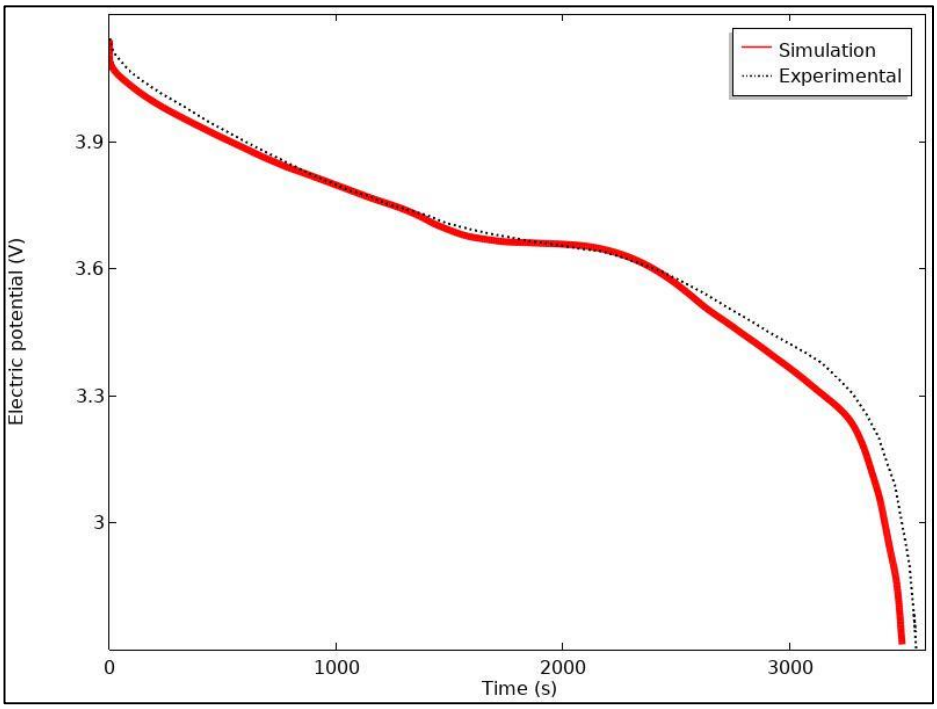

Figure 4.11. Simulated OCV of the battery before the parameters' optimization.

4.4. Design of Experiment

Fitting the model result on to experimental OCV data was performed by adjusting some of the important electrochemical parameters with a sensitivity analysis with the help of the forward difference method i.e. two-point difference method which is the 1st order derivative of the specified function. The method is chosen due to the fast step by step comparison and it is useful in solving ODEs. Moreover, the method had been used instead of backward difference method because of the fact that it provides a good accuracy in this study and comparing the central difference method forward difference method needs one data point less during the sensitivity analysis. This method basically works with shifting the function by 20% percent in positive direction with respect to reference function.

$$f'(x) = \frac{f(x+h) - f(x)}{h} \tag{4.32}$$

In the current model, in order to obtain the sensitivity results of the parameters, the Voltage change vs. time at 25 °C is simulated first. Then, the parameters used in the model were shifted 20% one by one (except geometrical parameters and accepted literature parameters). At the end of the analysis the results are compared, and the first five sensitive parameters are used for the perfection of the fitting. The sensitivity analysis process has represented in "Appendix B" and the parameters take place in the analysis has signed with the **(*)** symbol in Table 4.10.

After analyzing the parameters' sensitivity SNOPT method used for the optimization process. SNOPT method is useful for the evaluation of highly non-linear problems [80]. This process includes the minimization of the objective function which is the root-mean-square error of the voltage curve vs. time.

$$RMS = \sum_{i=1}^{N} [\mathrm{P}(u(\zeta_i), \zeta_i) - \mathrm{P}_i]^2 \tag{4.33}$$

In the formula given above is responsible for the analysis of the studied objective function where u represents the dependent variables and ζ denotes the control variables of the system. Five parameters which affects the shape of the curve strongest and their lower and upper limits for the optimization process are tabulated in Table 4.9.

Table 4.9. Optimized parameters for fitting the OCV curve of the battery.

Parameter name	**Symbol**	**Lower limit**	**Upper limit**	**Optimized Value**
Reaction rate coefficient of the positive electrode	k_{pos}	$4 \cdot 10^{-10}\ m/s$	$9 \cdot 10^{-10}\ m/s$	$8.342 \cdot 10^{-10}\ m/s$
Reaction rate coefficient of the negative electrode	k_{neg}	$2 \cdot 10^{-10}\ m/s$	$6 \cdot 10^{-10}\ m/s$	$3.624 \cdot 10^{-10}\ m/s$
Particle radius of positive electrode	$r_{p,pos}$	$6\ \mu m$	$18\ \mu m$	$6.751\ \mu m$
Particle radius of negative electrode	$r_{p,neg}$	$6\ \mu m$	$18\ \mu m$	$9.380\ \mu m$
Inactive part of positive electrode	$inactive_{pos}$	0.33	0.35	0.3371

The resultant OCV curve after the optimization process was applied to the model is shown in Figure 4.12.

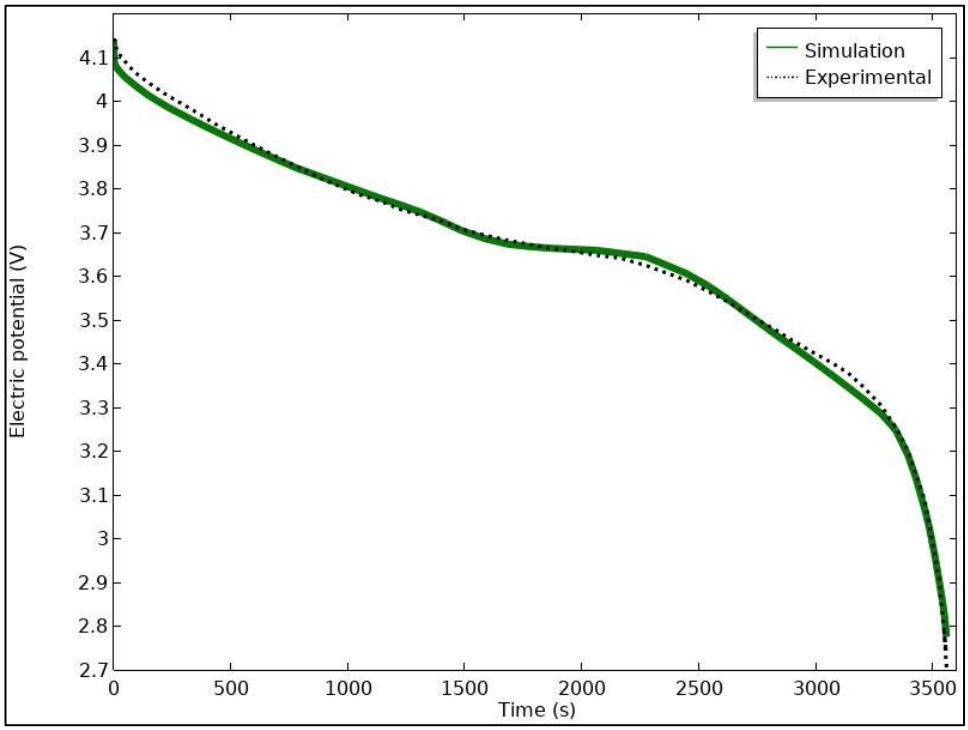

Figure 4.12. Optimized OCV simulation.

Moreover, the C-rate factor dependency of the OCV of the battery has been analyzed. The model has been fitted in a good accuracy to the experimental data. Figure 4.13. represents the fitting results of the model. While 0.5 C represents the current density of 3.75 A/h discharging, 1 C 7.5 A/h and 2 C corresponds to 15 A/h discharge current density.

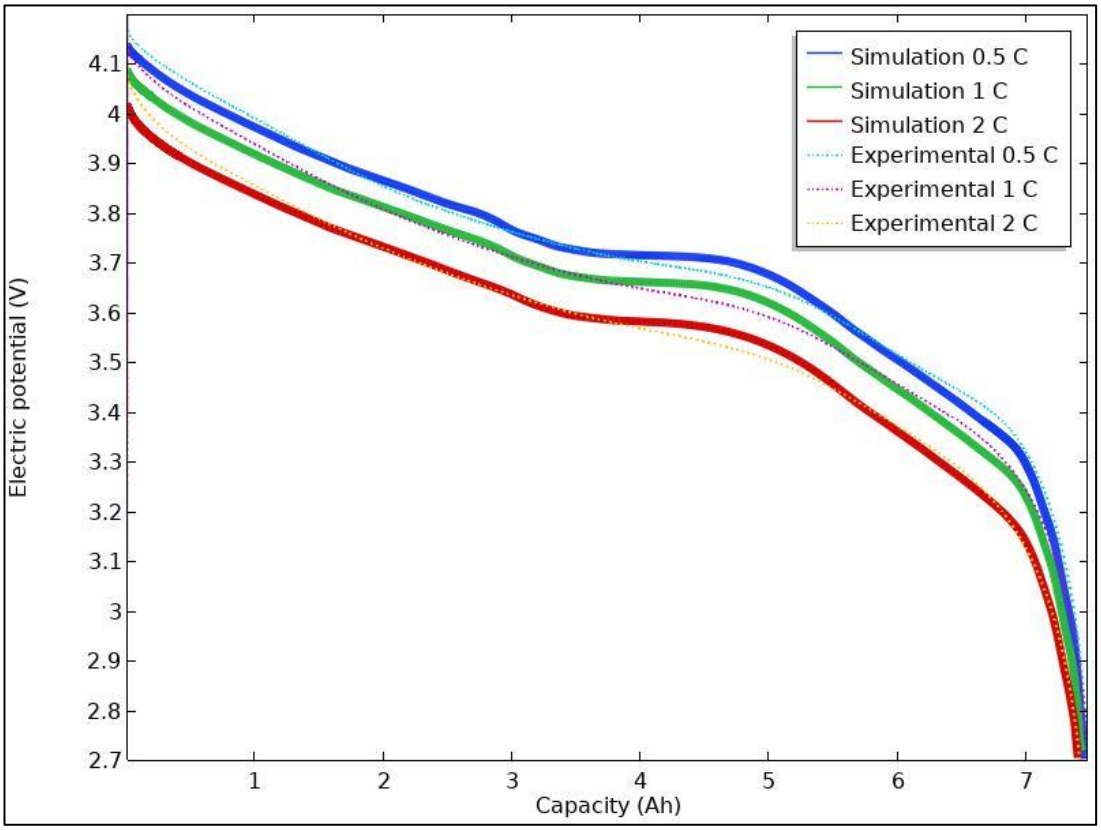

Figure 4.13. C-rate dependency of the model.

Furthermore, the effect of change in activation energies at 0 °C represented in Figure 4.14. Activation energy values of given in the table above increased by 50% one by one to observe graphically. As seen in the figure, activation energy of exchange current density of negative electrode and positive electrode can be considered as the most sensitive parameters respectively.

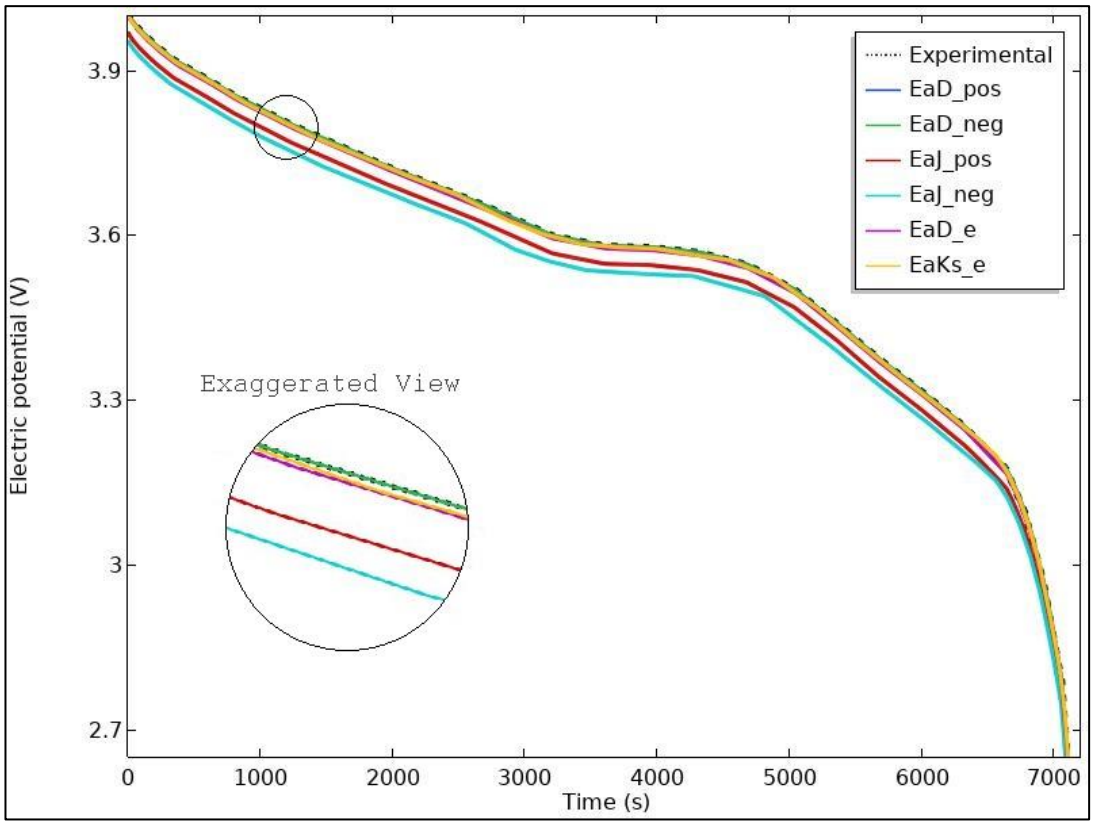

Figure 4.14. The effect of activation energy change on polarization curve at 0 °C. (EaD_pos: Activation energy of diffusion coefficient of positive electrode, EaD_neg: Activation energy of negative electrode, EaJ_pos: Activation energy of exchange current density of positive electrode, EaJ_neg: Activation energy of exchange current density of negative electrode, EaD_e: Activation energy of diffusion coefficient of electrolyte, EaKs_e: Activation energy of ionic conductivity of electrode.)

Nevertheless, at 0 °C experimental conditions capacity fade has been observed in the OCV curve. In the model, capacity fade had been studied by analyzing the inactive part of the positive electrode. As the temperature is lowering, the rate of non-reacting particles in NMC material increases. Results are shown in Figure 4.15.

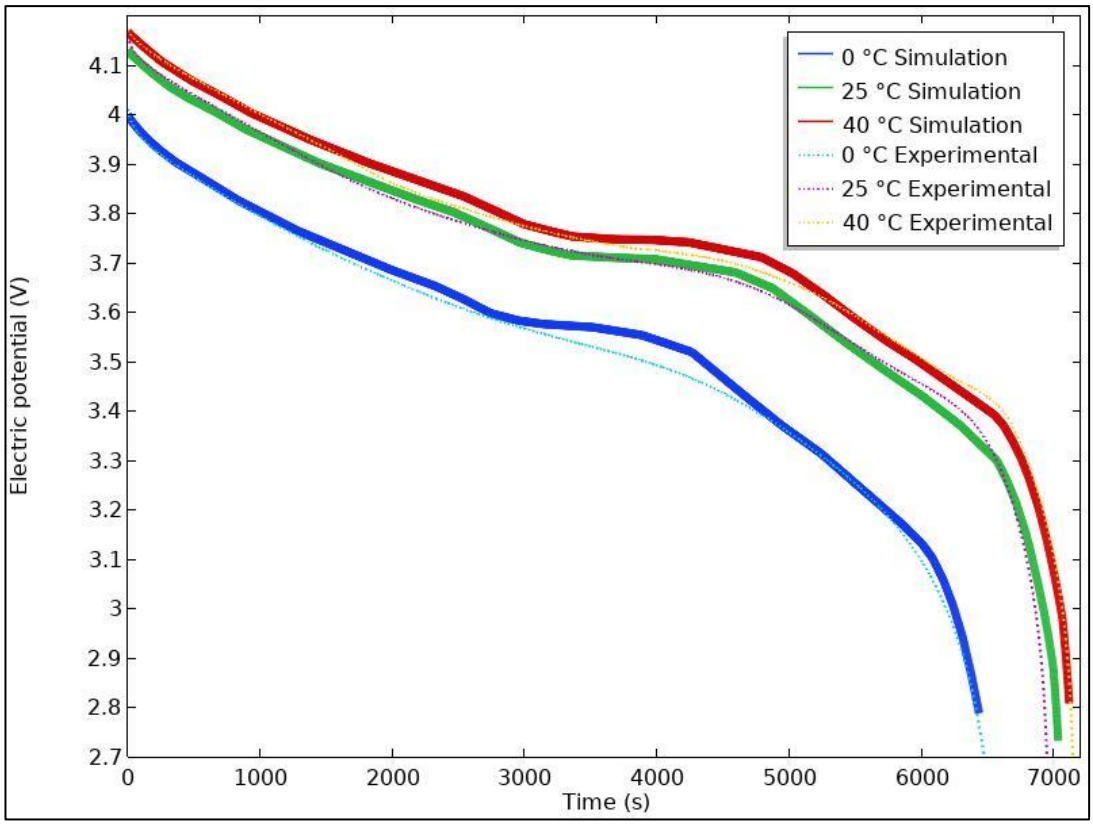

Figure 4.15. Temperature dependency of the studied battery.

Table 4.10. Parameters used in the model

Symbol	Parameter Description	Value	Unit
L_{pos}	Thickness of positive electrode	54.5	μm
L_{neg}	Thickness of negative electrode	73.7	μm
L_{sep}	Thickness of separator	19	μm
w_{pos}	Width of positive electrode	85	mm
w_{neg}	Width of negative electrode	87	mm
h_{pos}	Length of positive electrode	101	mm
h_{neg}	Length of negative electrode	103	mm
${r_{p,pos}}^*$	Particle radius of positive electrode	10.5	μm
${r_{p,pos}}^*$	Particle radius of positive electrode	9 and 60	μm
${c_{l,init}}^*$	Initial electrolyte salt concentration	1000	mol/m^3
$c_{s,init,pos}$	Initial solid phase concentration in a positive electrode particle	11659	mol/m^3
$c_{s,max,pos}$	Maximum solid phase concentration in a positive electrode particle	48580	mol/m^3
$c_{s,init,neg}$	Initial solid phase concentration in a negative electrode particle	23332	mol/m^3
$c_{s,max,neg}$	Maximum solid phase concentration in a negative electrode particle	31920	mol/m^3
$utilization^*$	Degree of utilization of positive electrode	0.76	%
${C_{SEI}}^*$	Capacity loss due to initial SEI formation	0.08	%
${inactive_{pos}}^*$	Inactive part of positive electrode	0.34	%

Table 4.10. Parameters used in the model. (Continue)

$inactive_{neg}$*	Inactive part of negative electrode	0.275	%
$\sigma_{s,pos}$*	Electronic conductivity of positive electrode	68.1	S/m
$\sigma_{s,neg}$*	Electronic conductivity of negative electrode	14	S/m
σ_e*	Ionic conductivity of electrolyte	Eq. 4.22	S/m
D_e*	Diffusion coefficient of electrolyte	$2.4 \cdot 10^{-10}$	m^2/s
$D_{s,pos}$*	Diffusion coefficient of positive electrode	Figure x.	m^2/s
$D_{s,neg}$*	Diffusion coefficient of negative electrode	Figure x.	m^2/s
k_{pos}*	Reaction rate coefficient of positive electrode	$8.158 \cdot 10^{-10}$	m/s
k_{neg}*	Reaction rate coefficient of negative electrode	$4.162 \cdot 10^{-10}$	m/s
ε_{pos}*	Porosity of positive electrode	0.296	%
ε_{neg}*	Porosity of negative electrode	0.329	%
ε_{sep}*	Porosity of separator	0.508	%
τ_{pos}*	Tortuosity of positive electrode	1.94	
τ_{neg}*	Tortuosity of negative electrode	2.03	
τ_{sep}*	Tortuosity of separator	1.67	
t_0^+	Transport number of electrolyte	0.26	
$\alpha_{A,pos}$*	Anodic transfer coefficient of positive electrode	0.48	
$\alpha_{C,pos}$*	Cathodic transfer coefficient of positive electrode	0.52	
$\alpha_{A,neg}$*	Anodic transfer coefficient of negative electrode	0.48	
$\alpha_{C,neg}$*	Cathodic transfer coefficient of negative electrode	0.52	
R_{film}*	SEI film resistance	0.0015	Ωm^2
$R_{current}$*	Current collectors' resistance	0.00125	Ωm^2
$c_{dl,pos}$*	Double-layer capacitance of positive electrode	0.7	F/m^2
$c_{dl,neg}$*	Double-layer capacitance of negative electrode	0.4	F/m^2
$c_{dlvol,pos}$*	Volumetric capacitance of electronic conductor in positive electrode	$2 \cdot 10^5$	F/m^3
$E_{a,D_s,pos}$	Activation energy of diffusion coefficient of positive electrode	80.6	kJ/mol
$E_{a,D_s,neg}$	Activation energy of diffusion coefficient of negative electrode	40.8	kJ/mol
E_{a,D_e}	Activation energy of diffusion coefficient of electrolyte	17.1	kJ/mol
$E_{a,i_0,pos}$	Activation energy of exchange current density of positive electrode	43.6	kJ/mol
$E_{a,i_0,neg}$	Activation energy of exchange current density of negative electrode	53.4	kJ/mol
E_{a,σ_e}	Activation energy of ionic conductivity of electrolyte	17.1	kJ/mol
*: Denotes that the parameter had been used in the sensitivity analysis in the transient response of the system.			

5. TRANSIENT ANALYSIS OF LI-ION BATTERIES

During the charge and discharging process electrochemical behavior of the battery changes due to the charge and mass transfer kinetics, reactions and diffusion process. Therefore, transient response of the battery has been analyzed in this chapter.

The change in SoC of positive and negative electrodes during the application of 0.5 C discharge current at 25°C is shown in Figure 5.1. As shown in the figure, after the discharging process begins the solid-state concentration in negative electrode slightly decreases while the concentration in positive electrode is increasing. When the SoC of negative electrode observed as 0, discharging process has been finished. Hence, in studied battery, solid-state concentration of negative electrode limits the experimental time.

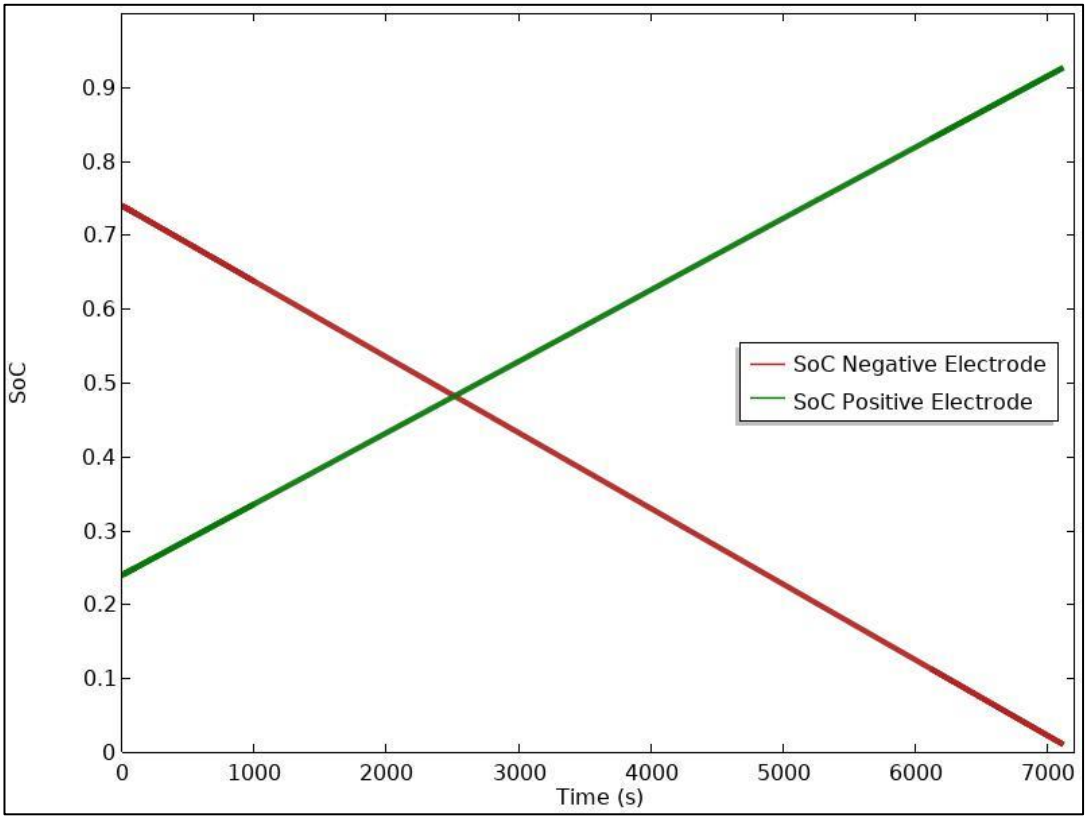

Figure 5.1. Change in SoC during the 0.5 C discharging process.

Furthermore, Figure 5.2. represents the SoC estimation process in the model for 80% SoC and 60% SoC. After applying discharge process to each SoC, relaxation should be applied for the electrochemical stabilization. Figure 5.3. shows the impact of the relaxation process on solid-state concentration of both electrodes. As shown in the figure, the concentration values of both electrodes are changing until the battery arises to the electrochemical balance.

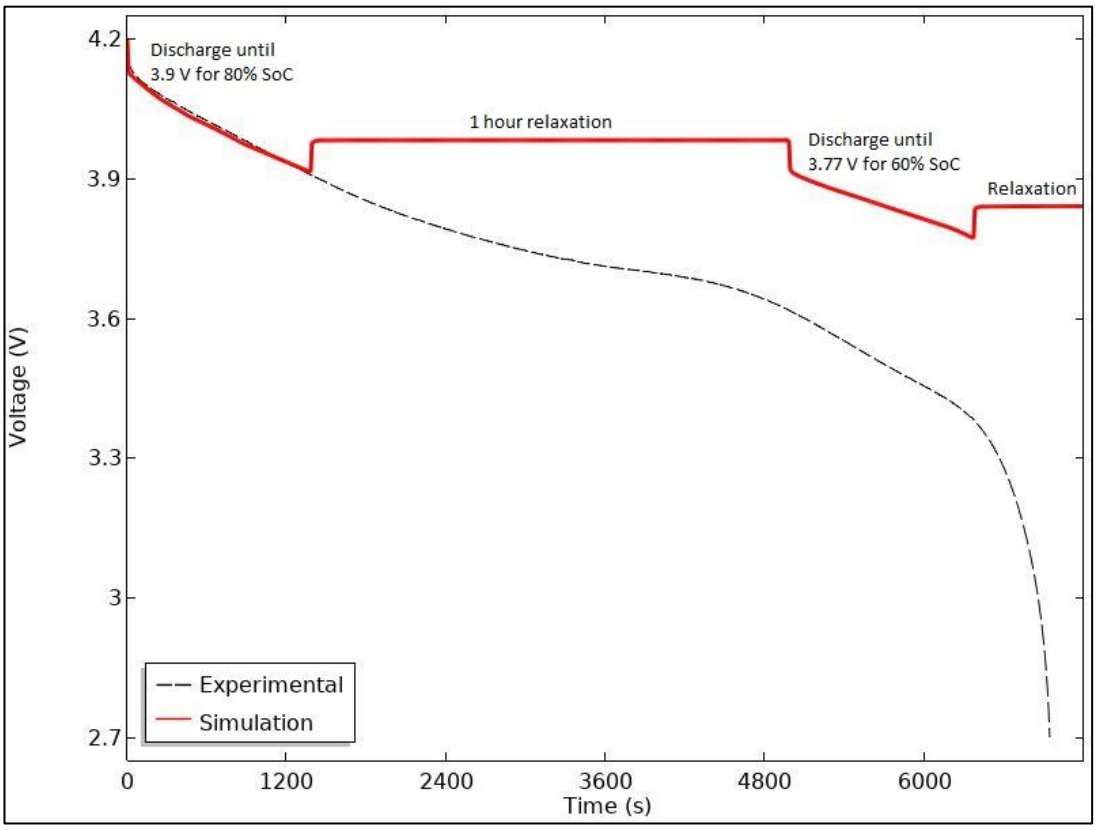

Figure 5.2. SoC estimation method for the battery.

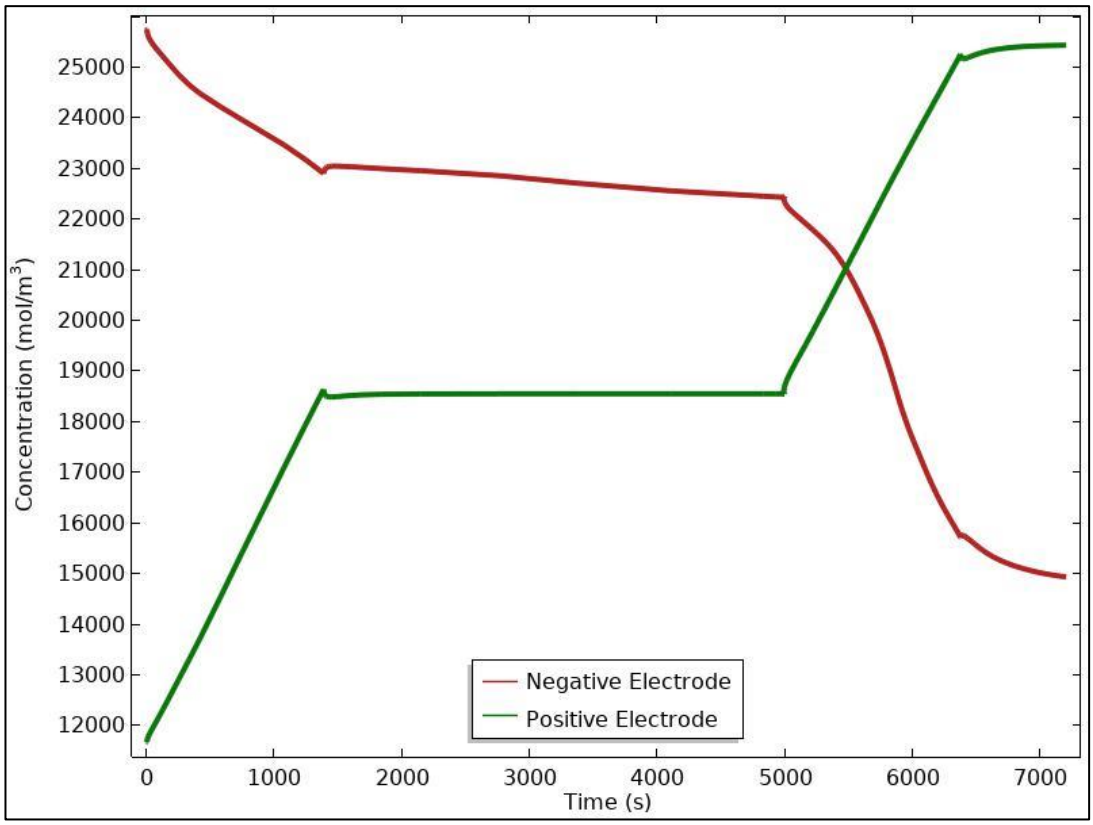

Figure 5.3. Change in solid-state concentration during the SoC estimation process.

Another application on the batteries is a one of the hybrid approaches which is the constant current – constant voltage (CC-CV) charge and discharging process. While the test time is mostly influenced by CC method, CV has an influence on capacity utilization. As Figure 5.4. shows the CC-CV process, at first the battery is discharged until the voltage becomes 2.7 V with constant voltage of 7.5 A, and constant voltage process keeps the battery at that voltage value until the discharging current reaches to 0.1 A. Secondly, the battery is charged up to 4.2 V with constant current of 7.5 A, and the battery was kept at the constant voltage till the charging current reaches to 0.1 A. While the charging process occurs, lithium concentration in the negative electrode decreasing, and in the positive electrode lithium particle concentration increases. In contrast, during the discharge process lithium particles are transferring from positive to negative electrode as shown in Figure 5.5.

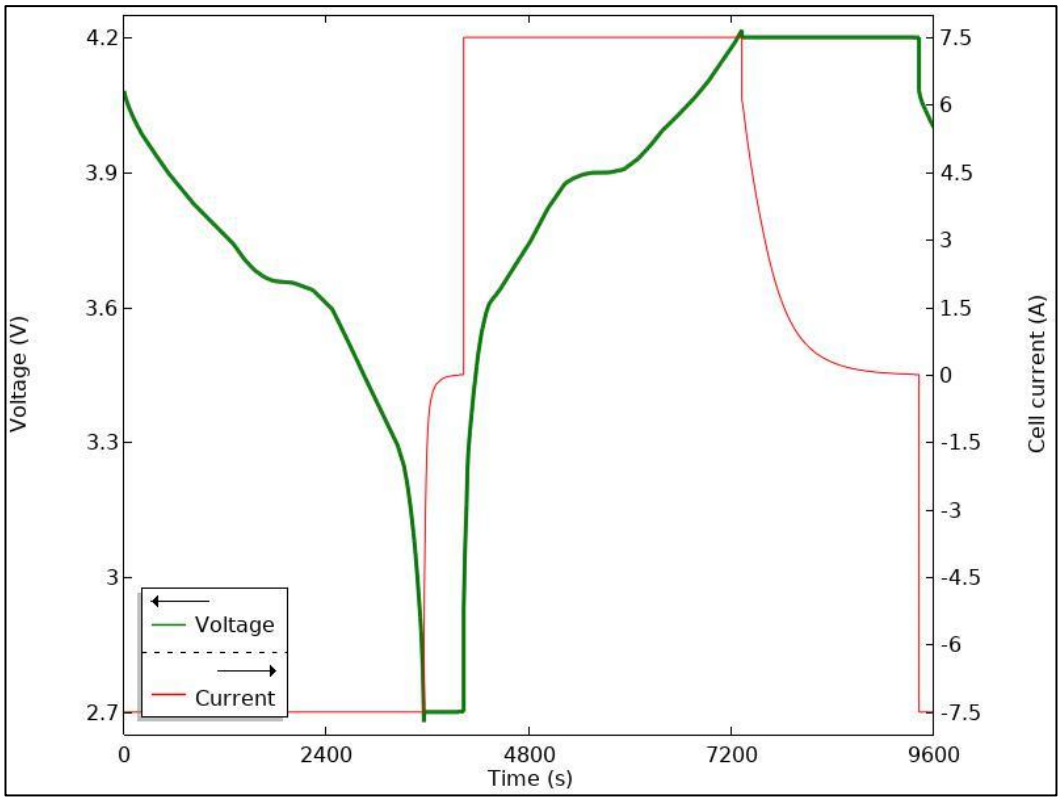

Figure 5.4. CC-CV charging and discharging process.

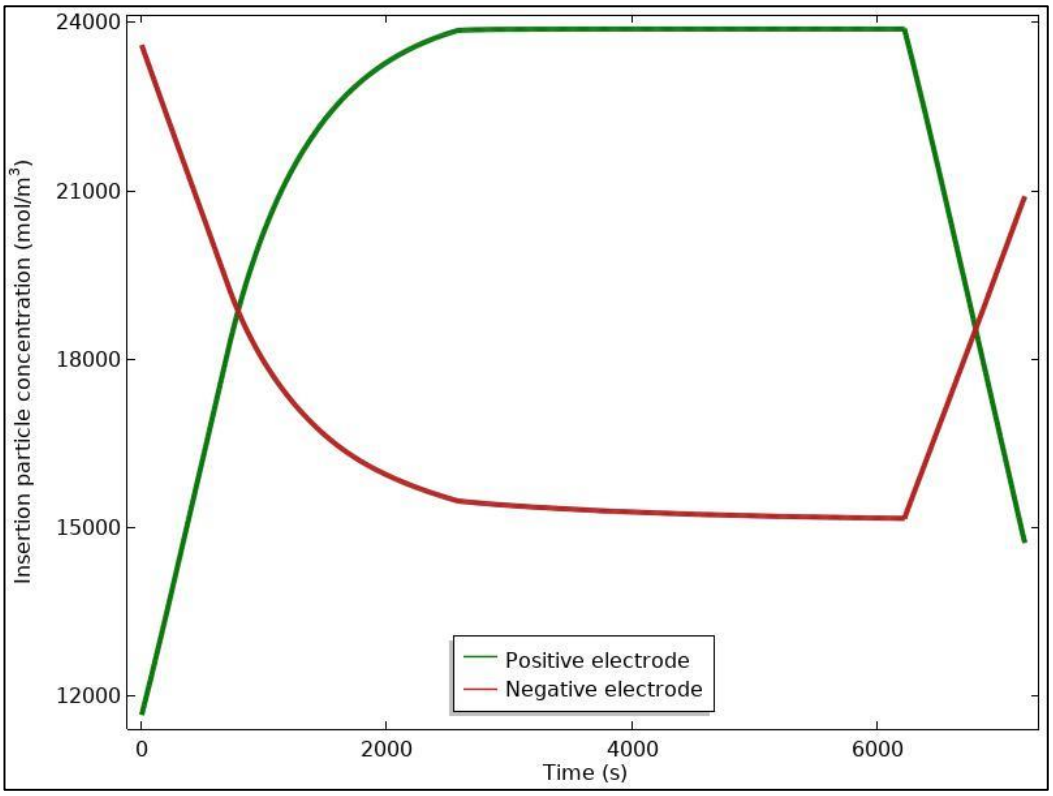

Figure 5.5. A graphical representation of the change in the particle concentrations in the electrodes during CC-CV discharging.

Nonetheless, the solid-state concentration values of the electrodes are obtained during the CC-CV charging process. As shown in the Figure 5.6., solid lines represent the CC process while charging and dashed lines correspond to CV period at 4.2 V. While the battery is charging until CV process, the solid-state concentration in negative electrode is increasing and positive electrode is decreasing. In addition, as represented in the figure, the concentration profile is changing trough the electrode thickness in CC process. That means, the particle intercalation slows down as the distance of the separator increases for both electrodes. On the other hand, during the CV process the concentration profiles are getting more stable i.e. Li^+ particles are intercalated the electrodes equally at the end of the process.

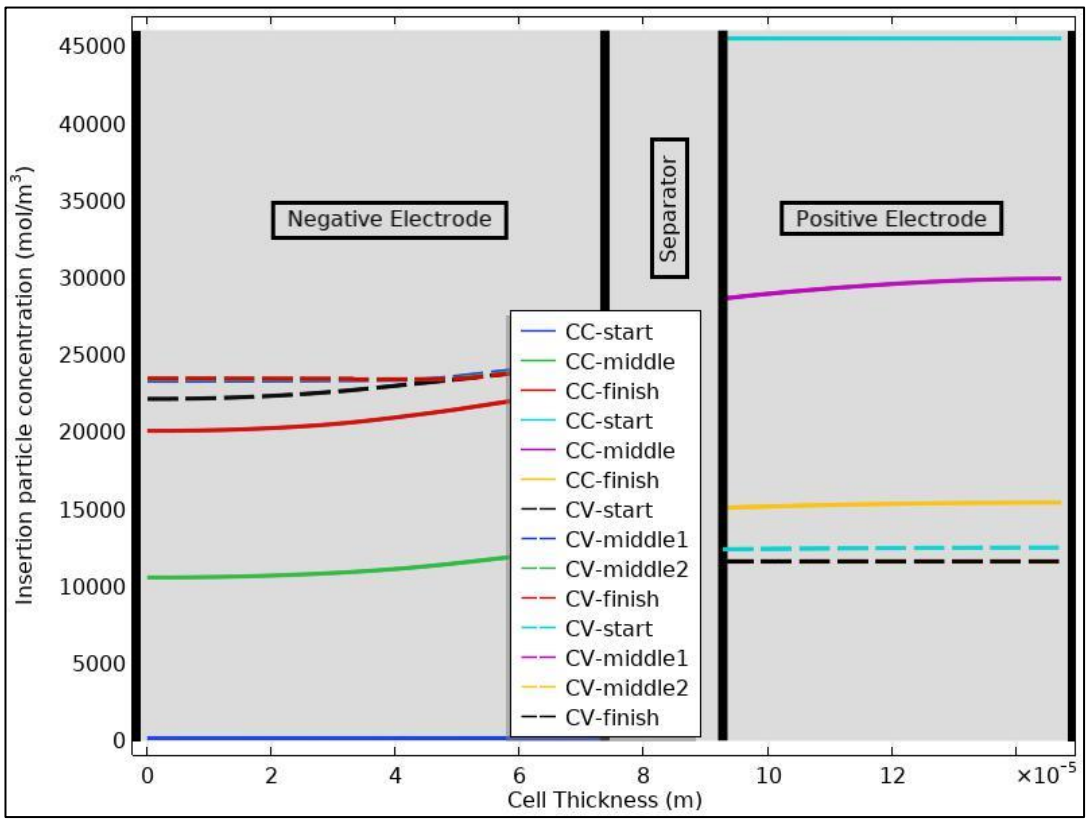

Figure 5.6. Concentration change in electrodes during the CC-CV charging process.

The CC-CV charge-discharge process could be used in order to investigate the ageing mechanism of the battery. In Figure 5.7. charge-discharge cycling of modeled battery has shown.

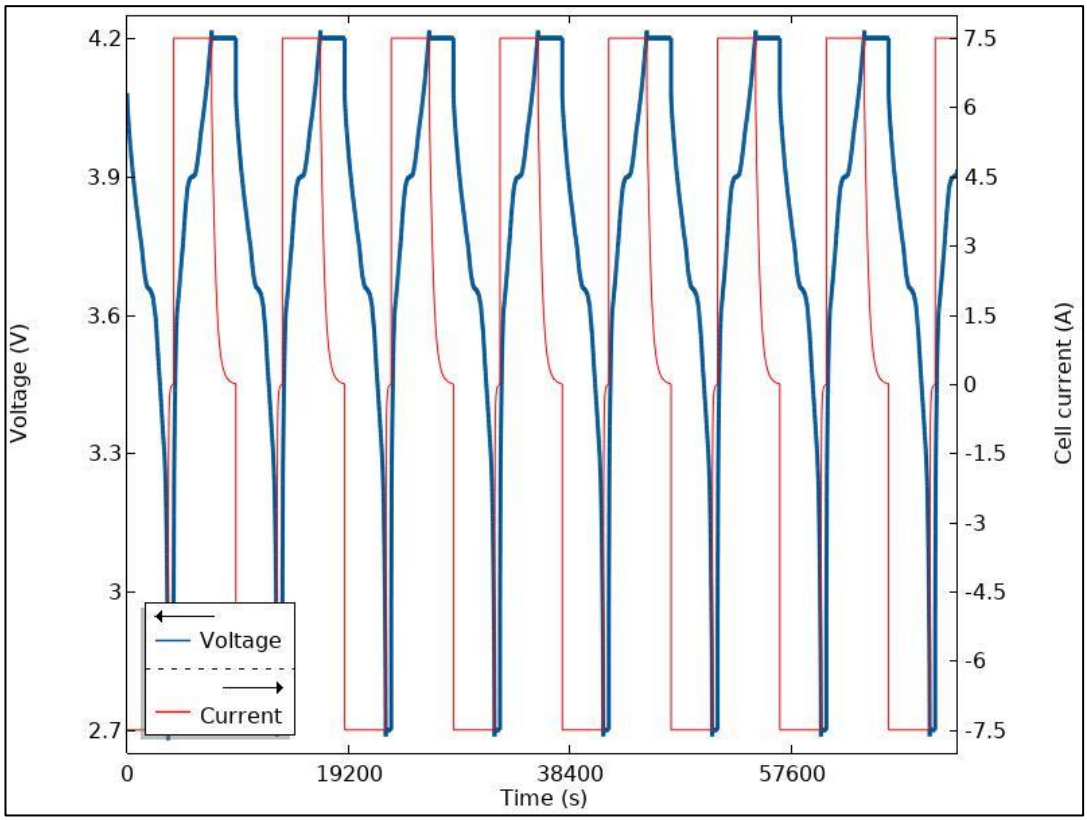

Figure 5.7. Charge-discharge cycle model of the battery.

Furthermore, Figure 5.8. shows the change in overpotential (η) during a period of the test time. As discussed in Chapter 4, while the overpotential is positive value in negative electrode, it is negative value in positive electrode related with equilibrium potentials of the electrodes. As represented in Figure 5.9. also, the electrode reaction source values ($i_{v,tot}$) behaves in parallel with the overpotential values. It is obvious that while the negative electrode is discharging, positive electrode is charging during the discharging process of the battery considering Butler-Volmer kinetics as evaluated in Eq. (4.11).

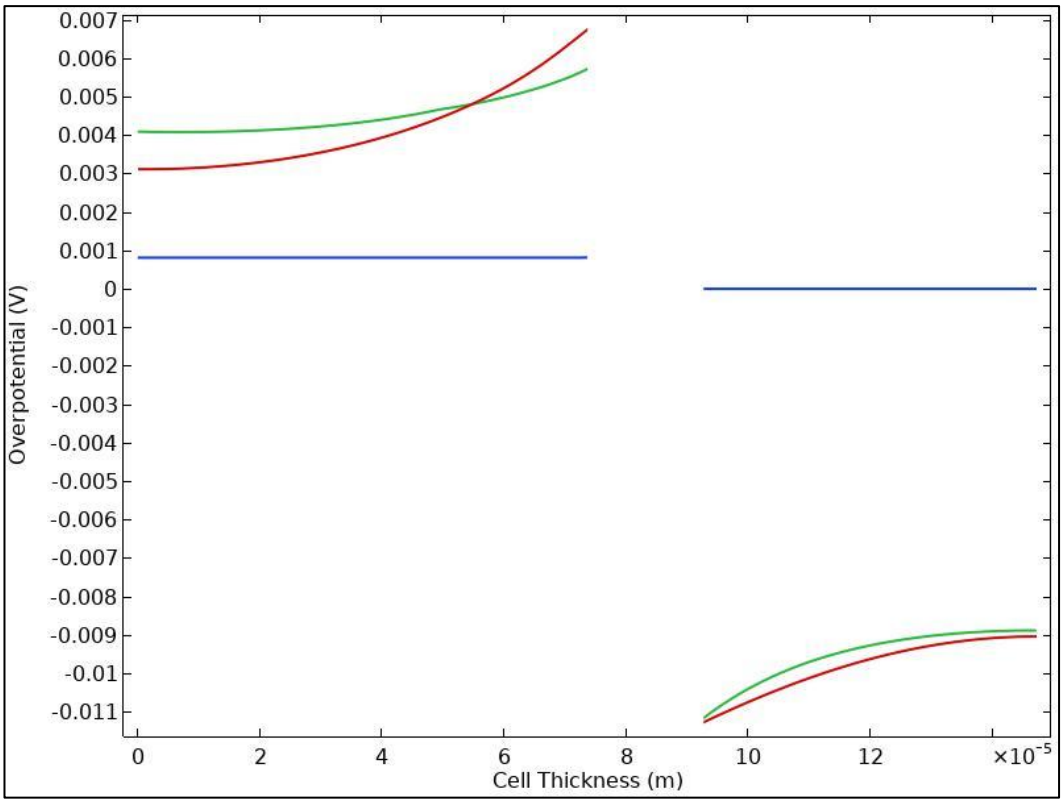

Figure 5.8. Change in overpotential values of electrodes.

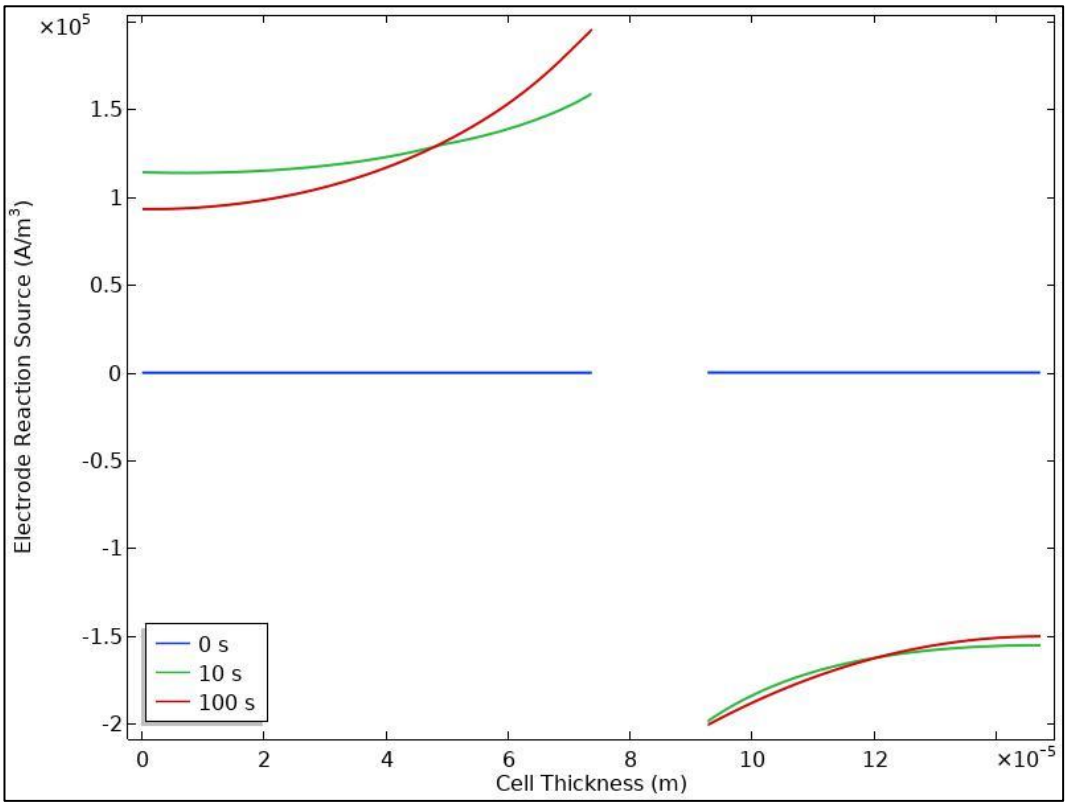

Figure 5.9. Change in electrode reaction source values of electrodes.

In addition, as mentioned before (see Chapter 4) transient analysis of proposed electrode model had been studied. Figure 5.10. shows the change in solid-state concentration values of small and big particles in negative electrode during the discharging process with 1-hour relaxations. The change in concentration during the discharge process associated with the particles' sizes in the electrode. By way of explanation, the mass transport of larger particles is relatively slower as a result of the consideration of non-reacting and partially reacting domains than the smaller ones.

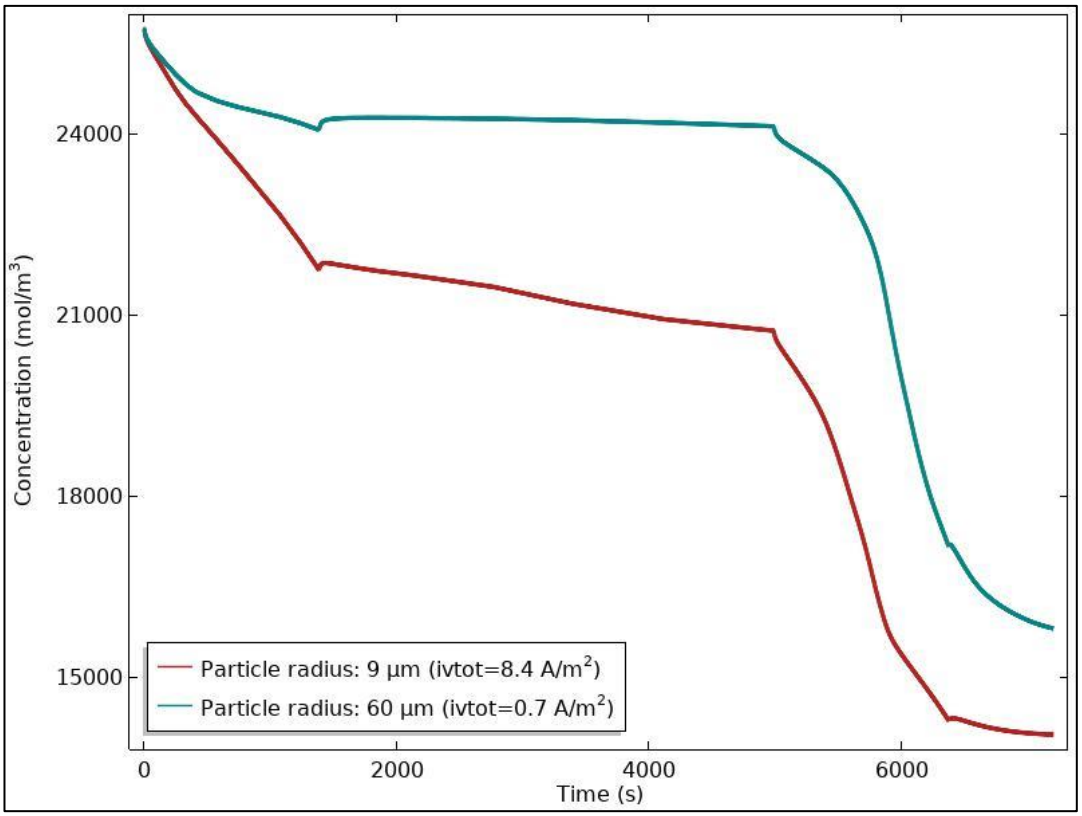

Figure 5.10. The concentration change in negative electrode with respect to particle size.

Besides, Figure 5.11 represents the relation between the change in overpotential and SoC change with respect to thickness of negative electrode. Overpotential of a cell is determined by the equilibrium potential which is also dependent on charge state of the battery. As the particle radius increases, the overpotential is decreasing and while the particle radius decreasing the change in SoC increases.

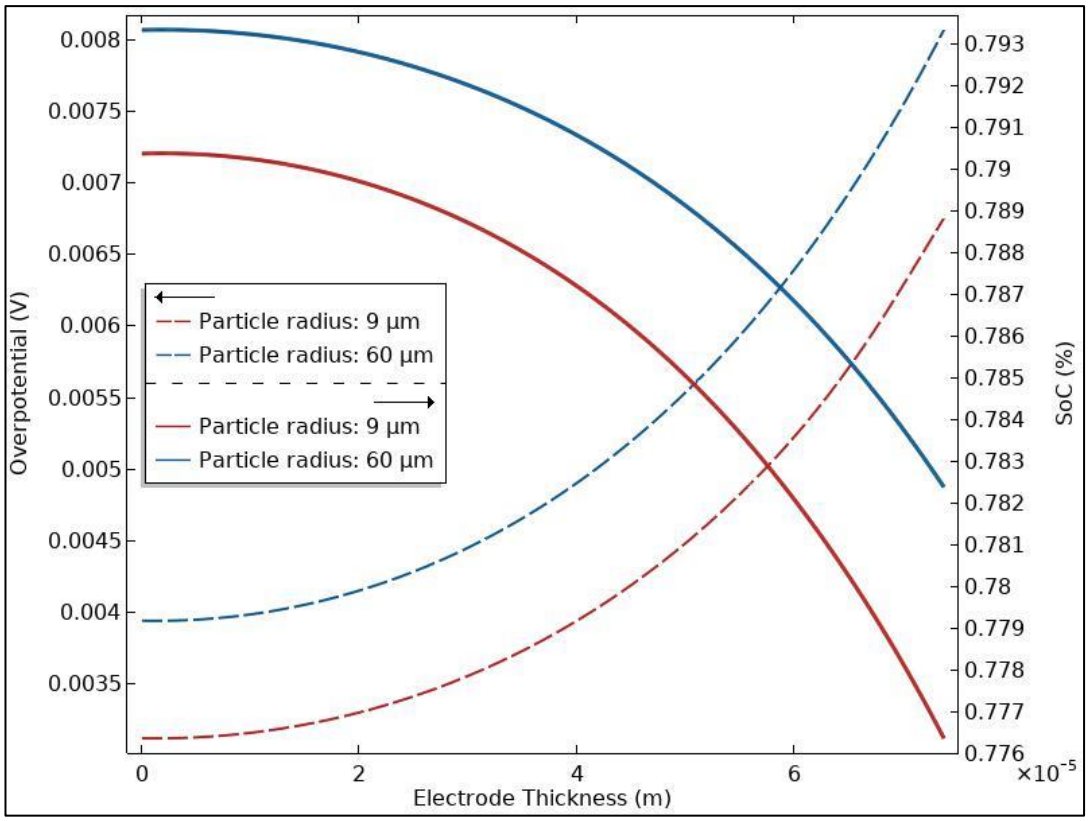

Figure 5.11. Overpotential vs. SoC vs. electrode thickness.

In addition, Figure 5.12. shows the relation between local current density and local current source with respect to thickness of negative electrode. As the particle radius increases, active specific surface area is increasing too. Hence, considering Eq. (4.9) as a result of the fact that active specific surface area is larger in bigger particles, the local current density of big particles is higher than smaller ones'.

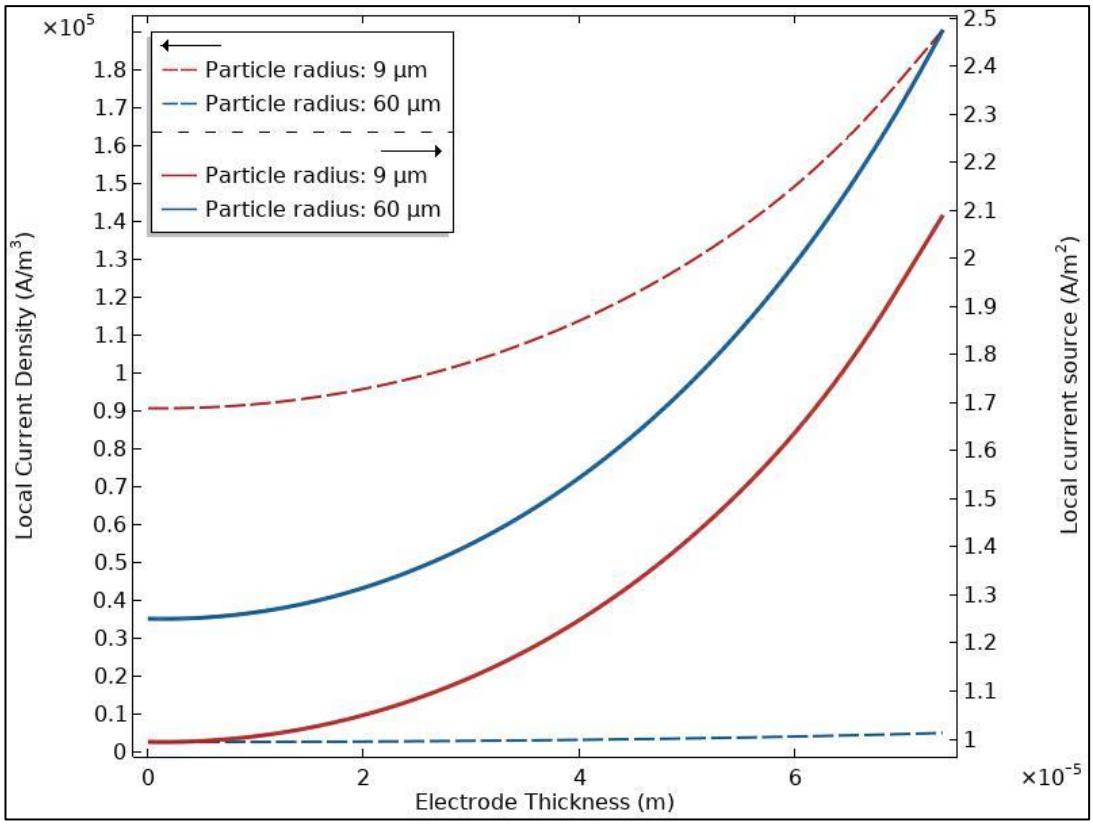

Figure 5.12. Local current density vs. local current source vs. electrode thickness.

6. PHYSICAL INTERPRETATION OF EIS OF LI-ION BATTERIES

One of the main objectives of this study is interpreting the impedance results and identify the parameters' impact on it. As discussed in Chapter 3, EIS measurements of Kokam SLPB pouch type battery was conducted at 25 °C and 100 kHz – 10 mHz frequency range. In this chapter, resultant EIS spectra and the effects of the parameters are represented. Additionally, EIS results of the electrodes are has shown separately.

The frequency response of the battery at 25 °C ambient temperature had shown in Figure 6.1. While the solid line indicates the model result, dashed line represents the experimental result. Inductive behavior of the battery is neglected.

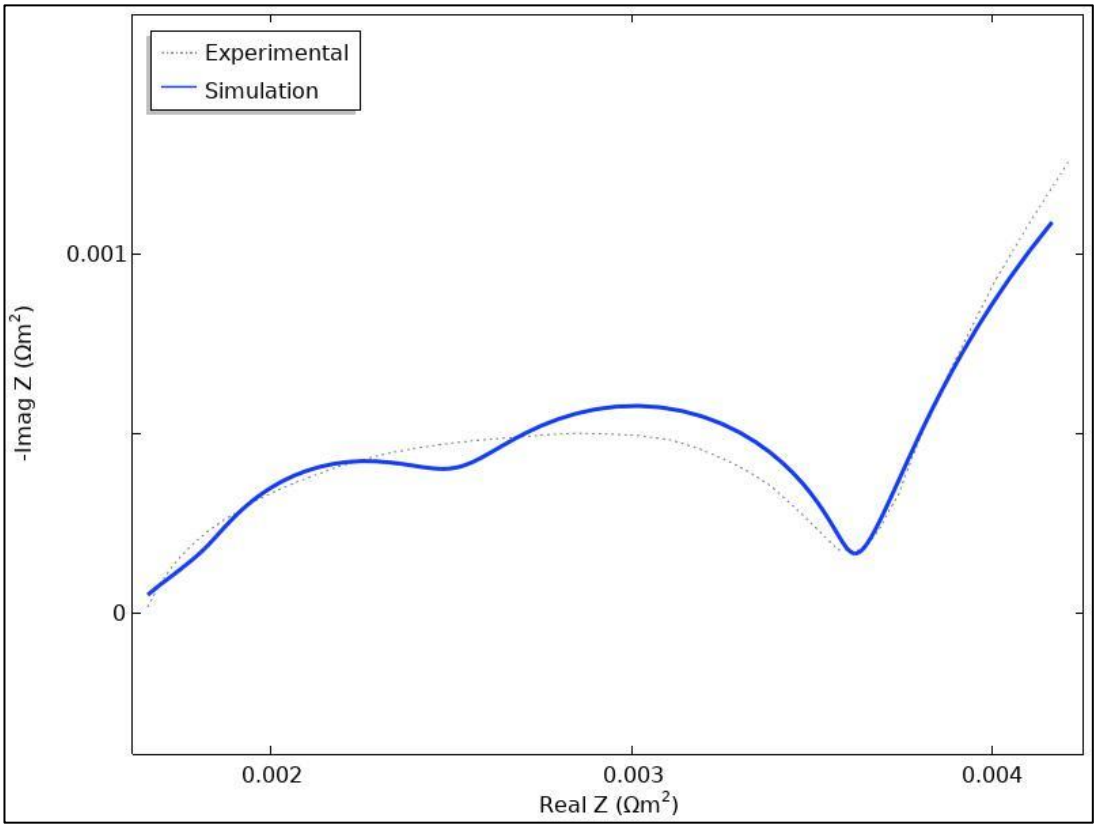

Figure 6.1. Resultant impedance model of the battery.

After the impedance spectra of the cell was obtained, the parameters which are affecting the shape of the curve had been graphically represented. As shown in the figures below, shape of the diffusion tail mostly affected by diffusion coefficients of the negative electrode, positive electrode and the electrolyte. It is observed that the angle of the diffusion tail mostly affected by the electrolyte diffusivity and the frequency response of the diffusion tail mostly associated with the diffusivity of positive electrode.

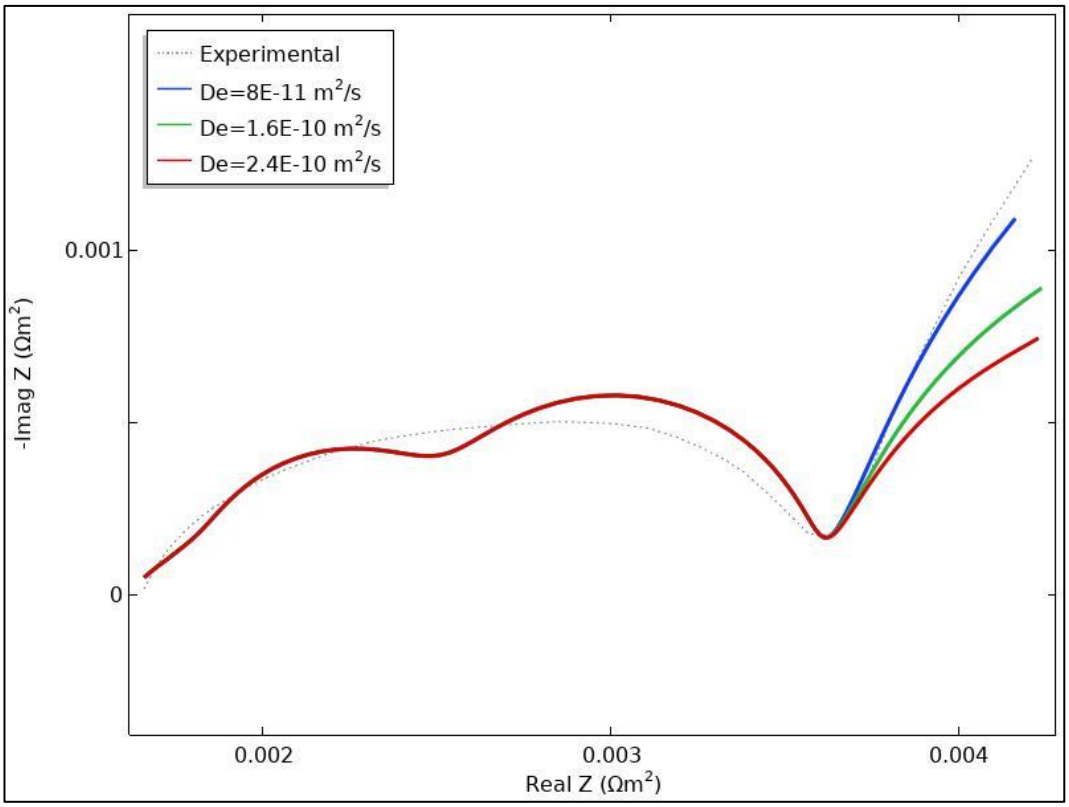

Figure 6.2. The effect of the diffusion coefficient of the electrolyte on Nyquist plot.

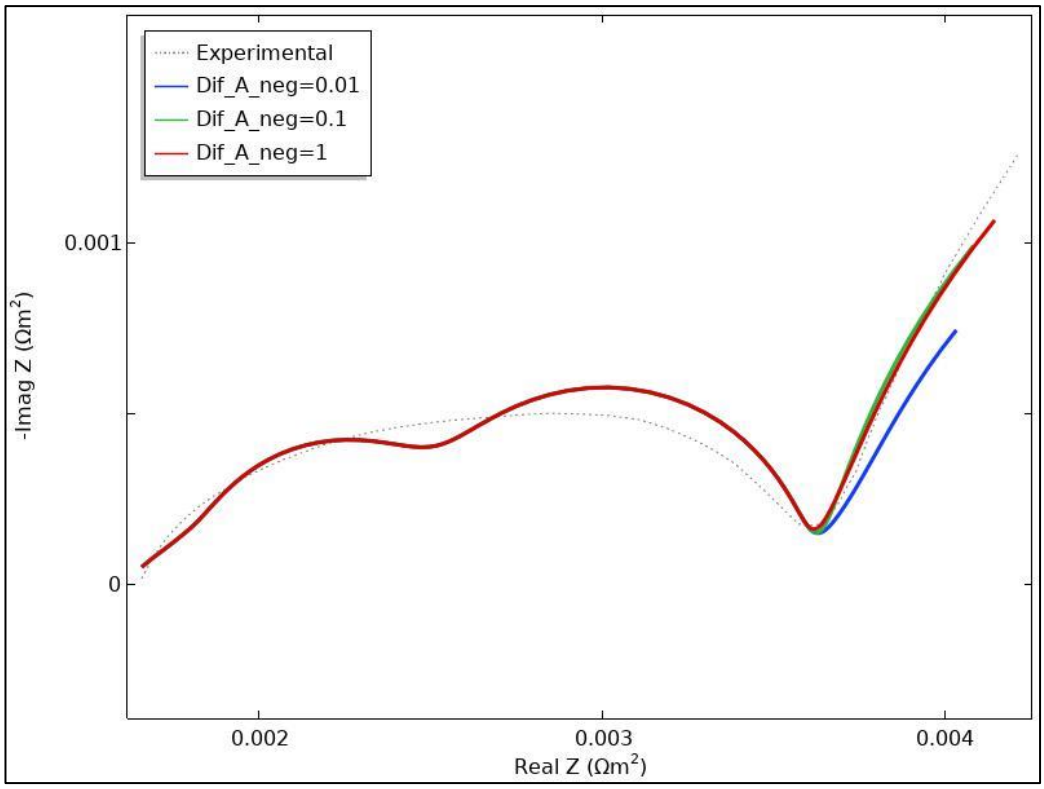

Figure 6.3. The effect of the diffusion coefficient of the negative electrode on Nyquist plot.

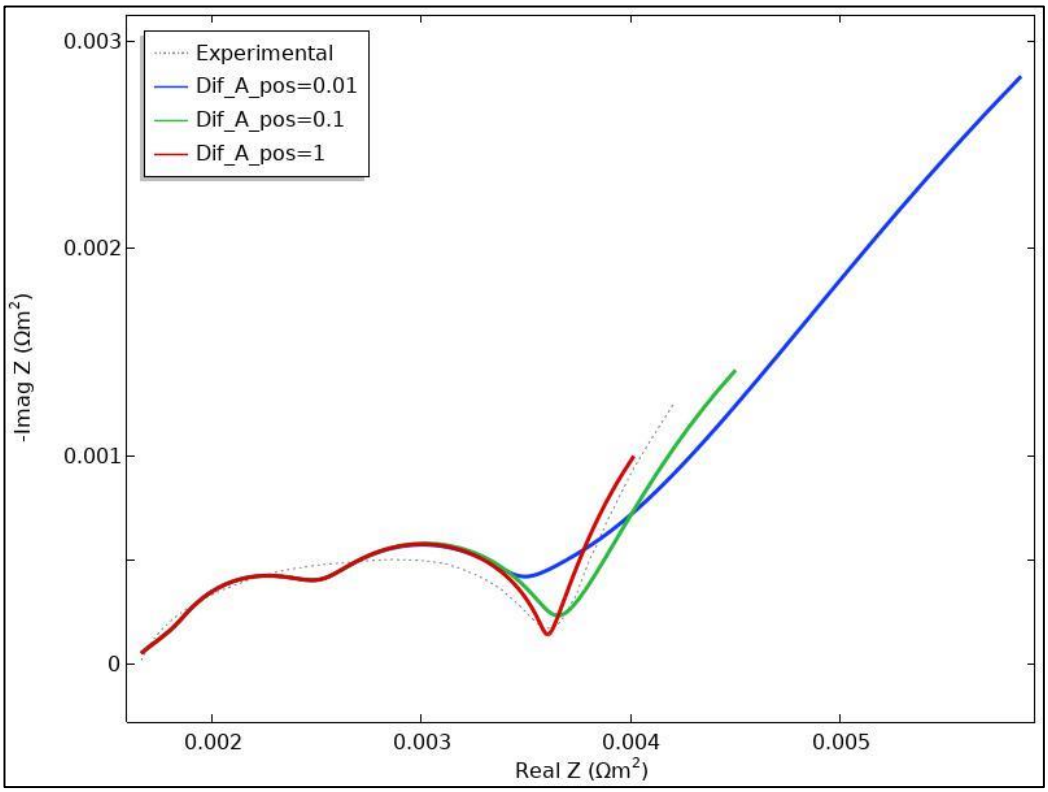

Figure 6.4. The effect of the diffusion coefficient of the positive electrode on Nyquist plot.

Also, it was clearly observed that the change in reaction rate coefficients of the electrodes mostly affect the charge transfer resistance of the battery, as well as the shape of the semi-circles. While the first semicircle is affected by the change of the reaction rate coefficient of negative electrode, it is not affected by the reaction rate coefficient of positive electrode. Thus, as mentioned earlier, it can be concluded that the first semicircle corresponds to the SEI formation in the negative electrode because it is not dependent to the change in charge transfer kinetics.

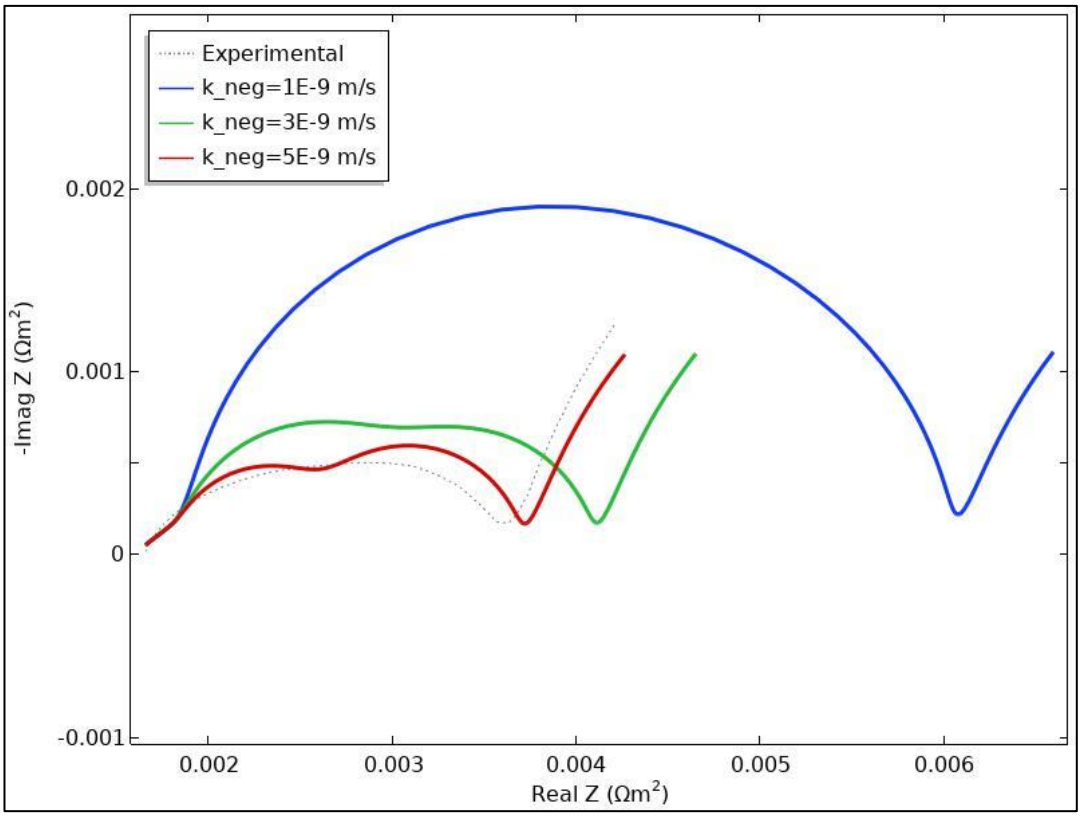

Figure 6.5. The effect of the reaction rate coefficient of the negative electrode on Nyquist plot.

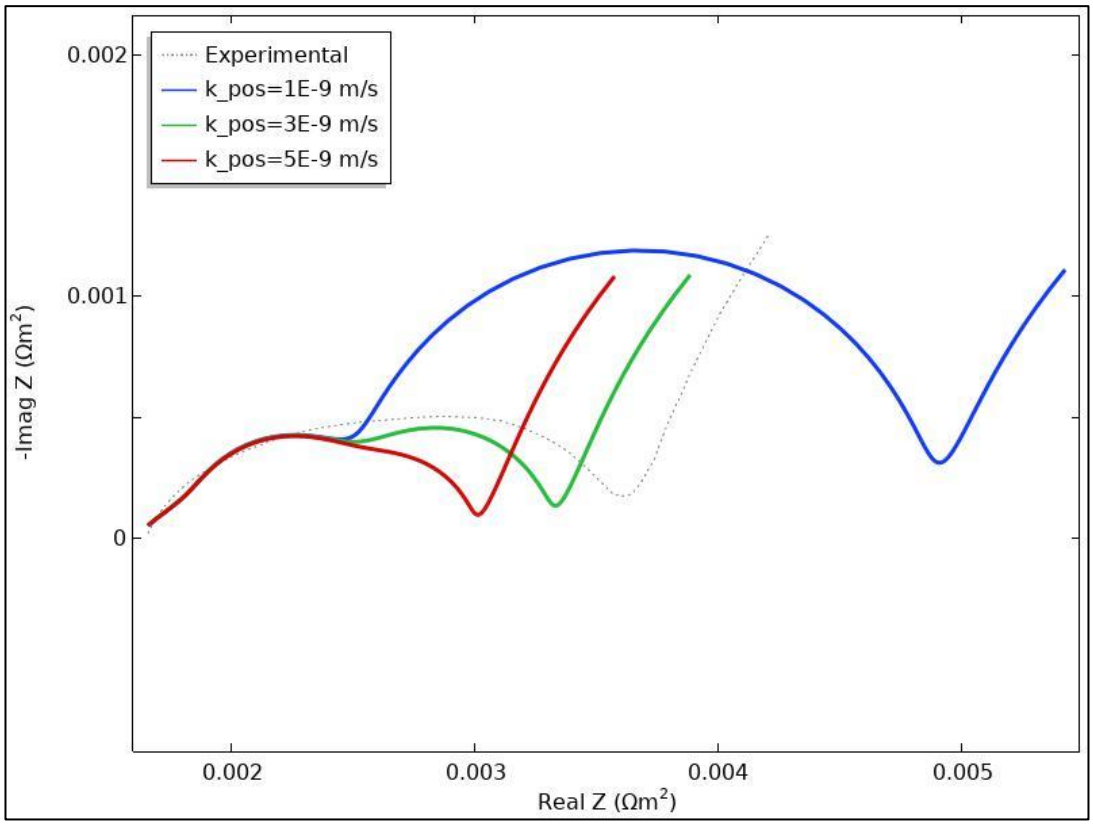

Figure 6.6. The effect of the reaction rate coefficient of the positive electrode on Nyquist plot.

The effects of double layer capacitance values of the electrodes and electronic conductors also represented in the figures below. While the change in DLC value of positive electrode assembling the semicircles, the change in DLC values of the negative electrode and electronic conductors affecting the impedance spectra significantly.

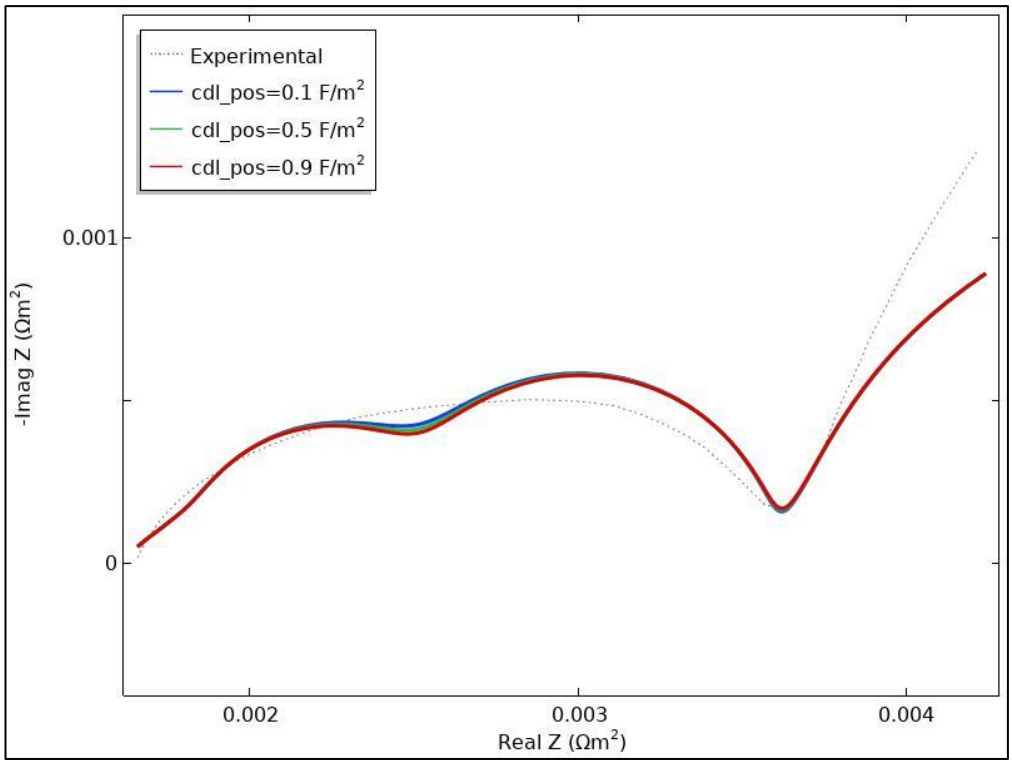

Figure 6.7. The effect of the double-layer capacitance of positive electrode.

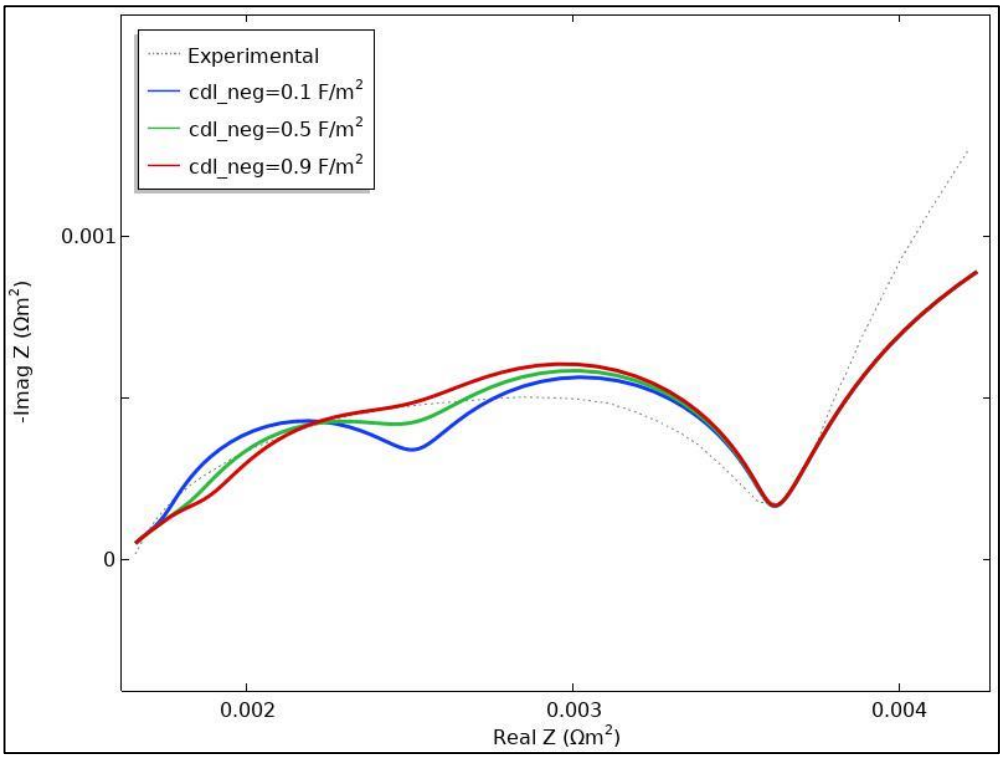

Figure 6.8. The effect of the double-layer capacitance of negative electrode.

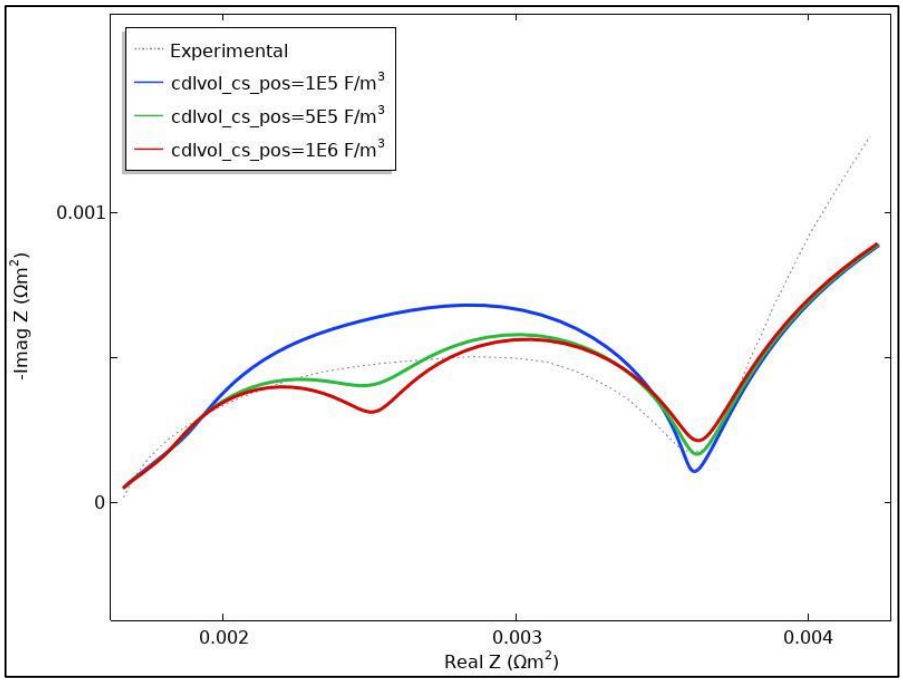

Figure 6.9. The effect of the double-layer capacitance of electronic conductors' in positive electrode.

It is observed that the current collectors' resistance affects the real part of the impedance spectra which results as the increase of the resistance shifts the curve on positive real Z axis. In other words, current collectors' resistance associates with the first intersection point of the impedance data with the real part of a Nyquist plot.

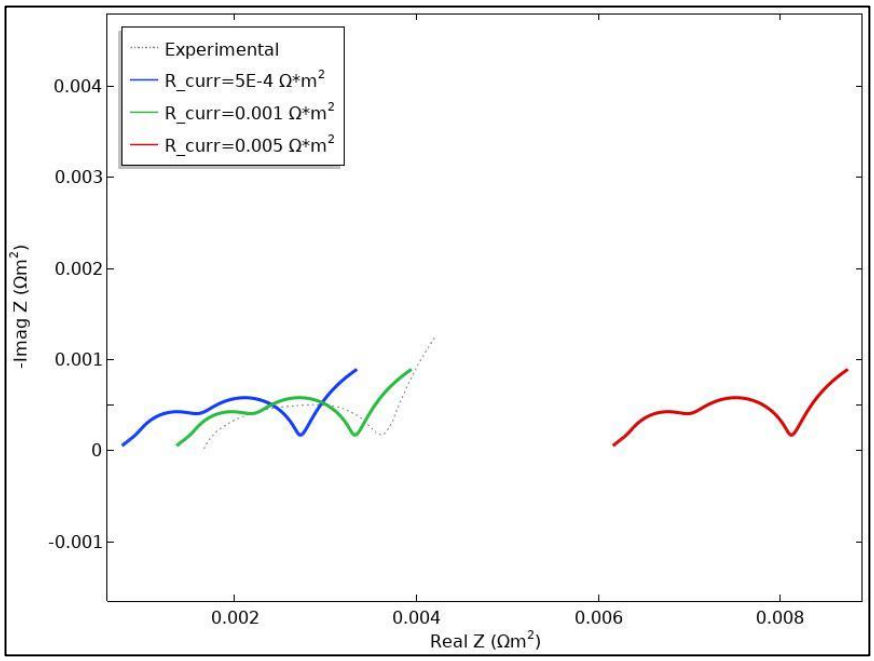

Figure 6.10. The effect of the current collectors' resistance on Nyquist plot.

As discussed earlier, the first semi-circle is associated with the SEI formation in negative electrode. In Figure 6.11., the change in SEI resistance has shown. As the SEI film resistance increases, the first semi-circle enlarges. On the other hand, due to the enlargement of the first semi-circle, the charge transfer resistance is shifting on real Z axis. Hence, to conclude the SEI formation is one of the key factors associated with a poor charge transfer condition.

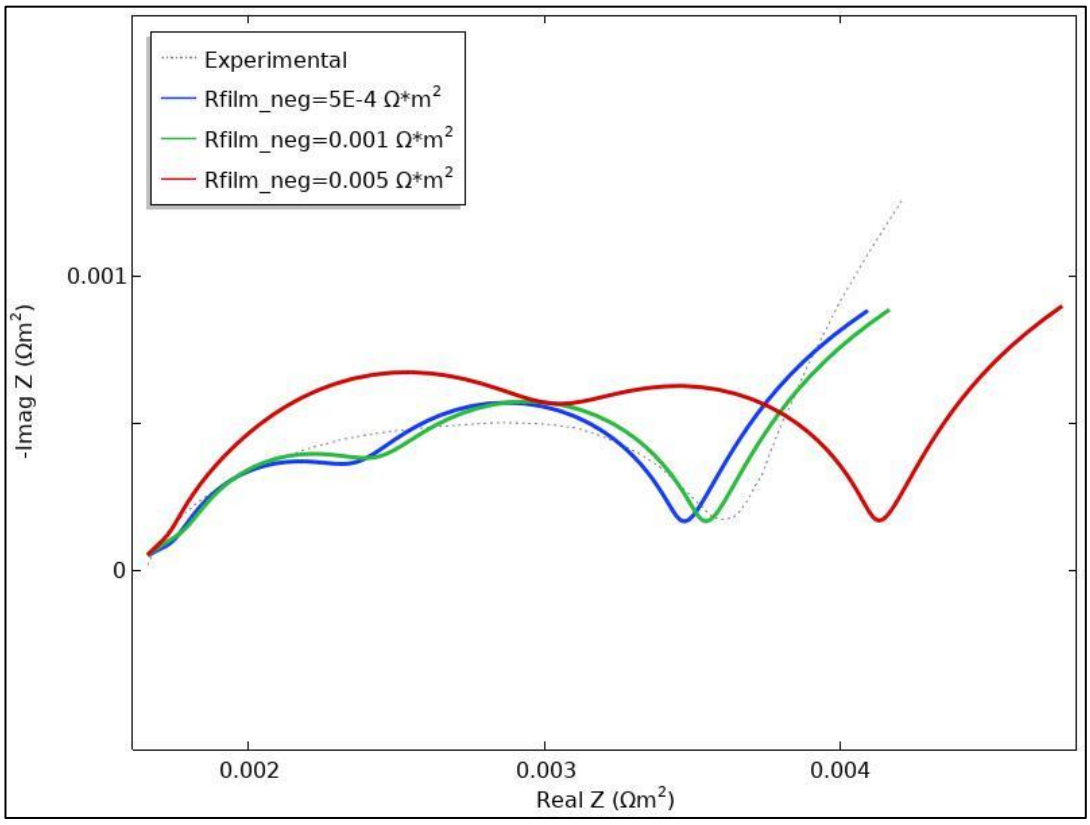

Figure 6.11. The effect of SEI film resistance on Nyquist plot.

The temperature dependence of the battery also represented in Figure 6.12. As the temperature decreases the performance of the battery slightly decreases and charge transfer resistance increases.

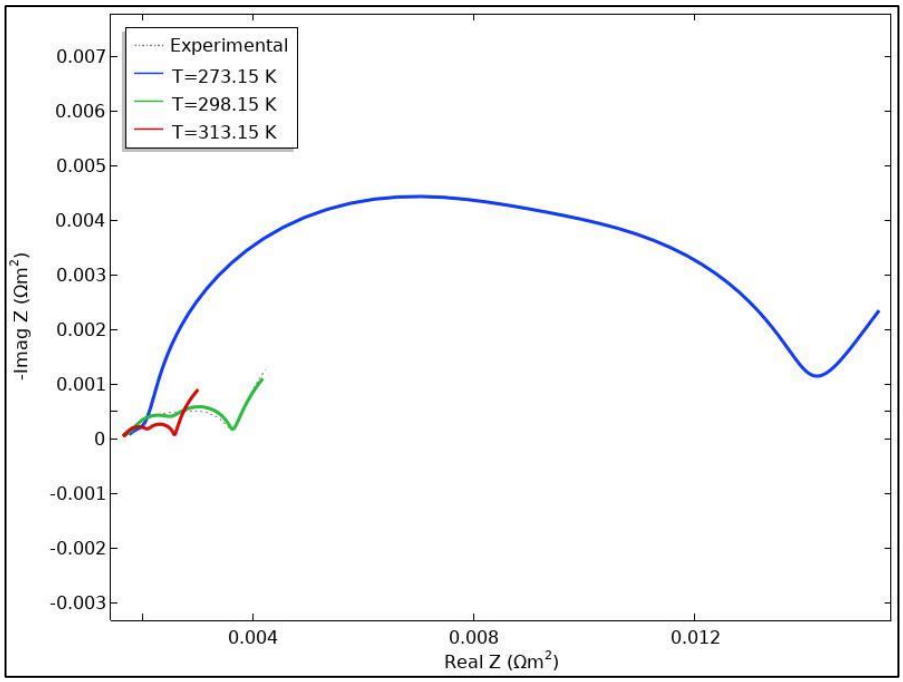

Figure 6.12. Effect of change in ambient temperature on Nyquist diagram.

Lastly, the impedance spectra of positive and negative electrodes have been modeled and represented in Figure 6.13. While positive electrode's charge transfer resistance is greater than the negative electrode the diffusion behavior of both electrodes is differing from each other. While the NMC material's diffusion tail can be observed as FSW, graphite's diffusion tail behaves as FLW.

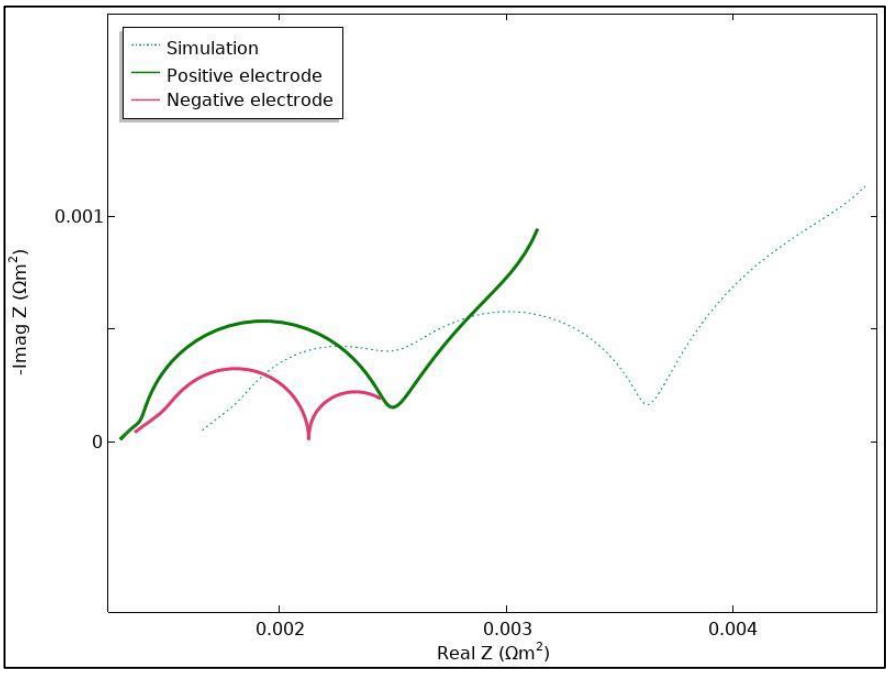

Figure 6.13. Impedance spectra of negative and positive electrodes.

7. FUTURE WORK

As discussed earlier modeling the electrochemical impedance of the energy conversion systems is considerable research field in order to understand the physical properties and their meanings detailed. In this study, a 1-D physical impedance of a battery had been modeled and the results were interpreted.

In order to increase the model accuracy and describe additional parameters which affect ECSs performance directly 2-D model will be studied based on multiscale – multidomain approach. 2-D modeling provides to analyze the temperature gradients, voltage gradients and the effects connection elements between the electrodes. Investigation of those effects would be an important step for understanding complex system dynamics. Besides, after investigation of 2-D dynamics of the battery, consideration of 3-D model would help to identify the battery packing affects.

Moreover, the purposed electrode model will be studied in order to analyze the electrode's performance and characteristics more detailed. Hence, the effects of the particle size distribution could be illuminated with this study.

8. CONCLUSIONS AND OUTLOOK

The importance of evaluating the performance and the physico-chemical behavior of the electrochemical energy conversion systems such as fuel cells, batteries and supercapacitors is projecting many ways to the study groups to develop a new perspective. As discussed in Section 2, it is observed that most of the developed models are not enough to make quantitative predictions about the internal parameters about the electrochemical systems. As a result of this motivation, a battery which is the one of the most common energy storage systems had been studied in this master's thesis by carrying out a novel method.

Firstly, a 1-D porous electrode theory based physico-chemical study of a 7.5 Ah commercially available lithium-ion battery had been developed with the integration of the measurement parameters into the model in order to investigate the dynamical behavior of discharge characteristics. The parameters which affect the discharge curve strongly had been identified with a sensitivity analysis by applying one of the numerical analysis, which is forward difference method. The results obtained by sensitivity analysis showed us, the parameters related with charge transfer kinetics, mass transport and diffusion behavior have affected the polarization curve strongly of the studied battery. Therefore, the optimization process had been employed in order to increase the accuracy of the model of transient behavior of the battery. In addition, by minimizing the objective function i.e. root-mean-square error of the simulation and the experimental data, also by identifying the lower and upper limits of the most sensitive five parameters had been resulted in good accuracy in optimization process. It seems that discharge curve after employing SNOPT method with proper boundary conditions can provide prediction of the parameters of designed LIB accurately and leads to develop new interpretation techniques for the parameter identification in practice.

Secondly, the temperature dependent characteristics of the transient response of the battery had been evaluated. Thus, activation energies of the temperature dependent parameters had been considered and integrated to the model with Arrhenius relationship. According to simulation results, capacity fade is observed as the temperature lowering. The analyses showed that the rate of inactive part of the positive electrode has got a significant effect on temperature-dependent capacity fade of LIBs.

That means, in lower-temperature operating conditions, the fraction of nonreacting particles are increasing during the discharge process and the charge-transfer resistance increasing.

Finally, the battery had been modeled in frequency domain with multiscale – multidomain approach and the model results were compared to the experimental impedance results so that to develop a method for identifying the physical meanings of the parameters and to draw conclusions about the performance of a designed cell. The impedance of the electrodes separately had been represented and the influence of the parameters shown in this study. In addition, it was observed that although studied 1-D model had got good results, in order to increase the accuracy and analyze the effects which cannot be observed in one-dimensional space such as temperature gradient and voltage gradient on impedance measurements 2-D and 3-D models of the battery should be developed.

Additionally, investigation of particle size of the electrodes had been considered and developed a novel strategy for electrode modeling which consists of three separated domains. While for large particles the first domain corresponds to non-reacting particles and the second domain corresponds to partially reacting particles, for small particle size third domain had been treated as reacting particles. The results and proposed model had been represented. Moreover, further studies based on this approach would be a step to analyze comprehensive electrode dynamics.

REFERENCES

[1] Ruhe C. H. W., (1973) , "Statistical Review.", JAMA: The Journal of the American Medical Association, 225 (3), 299–306.

[2] Goss R. M., (1983) , "BP statistical review of world energy 1982.", (June),.

[3] Badwal S. P. S., Giddey S. S., Munnings C., Bhatt A. I., & Hollenkamp A. F., (2014) , "Emerging electrochemical energy conversion and storage technologies.", Frontiers in Chemistry, 2 (SEP), 1–28.

[4] Ch J. P. E. N., (2020) , "各 種 試 験 結 果.", 1–2.

[5] Mehta V. & Cooper J. S., (2003) , "Review and analysis of PEM fuel cell design and manufacturing.", Journal of Power Sources, 114 (1), 32–53.

[6] Peighambardoust S. J., Rowshanzamir S., & Amjadi M., (2010) , "Review of the proton exchange membranes for fuel cell applications.", International Journal of Hydrogen Energy, 35 (17), 9349–9384.

[7] van den Oosterkamp P. F., (2006) , "Critical issues in heat transfer for fuel cell systems.", Energy Conversion and Management, 47 (20), 3552–3561.

[8] Yıldırım Y., (2011) , "Zonguldak karaelmas üniversitesi çevre mühendisliği ders notları.", ÇEV 346 Yakıt Pilleri Ders Notları, 156 315–322.

[9] Collins D. H., (1985) , "Modern batteries. An introduction to electrochemical power sources.", Journal of Power Sources, 14 (4), 331–332.

[10] Piernas Muñoz M. J. & Castillo Martínez E., (2018) , "Introduction to batteries.", SpringerBriefs in Applied Sciences and Technology, (December), 1–8.

[11] Ransitions E. N. T., (2010) , "Energy Transitions - History, Requirements, Prospects (2010) by Vaclav Smil.",.

[12] Miao Y., Hynan P., Von Jouanne A., & Yokochi A., (2019) , "Current li-ion battery technologies in electric vehicles and opportunities for advancements.", Energies, 12 (6), 1–20.

[13] Nathan A. J. & Scobell A., (2012) How China sees America. .

[14] Mousavi G. S. M. & Nikdel M., (2014) , "Various battery models for various simulation studies and applications.", Renewable and Sustainable Energy Reviews, 32 477–485.

[15] Kirn Y. H. & Ha H. D., (1997) , "Design of interface circuits with electrical battery models.", IEEE Transactions on Industrial Electronics, 44 (1), 81–86.

[16] Valenciaga F., Puleston P. F., Battaiotto P. E., & Mantz R. J., (2000) , "Passivity/sliding mode control of a stand-alone hybrid generation system.", IEE Proceedings: Control Theory and Applications, 147 (6), 680–686.

[17] Dürr M., Cruden A., Gair S., & McDonald J. R., (2006) , "Dynamic model of a lead acid battery for use in a domestic fuel cell system.", Journal of Power Sources, 161 (2), 1400–1411.

[18] Cun J. P., Fiorina J. N., Fraisse M., & Mabboux H., (1996) Experience of a UPS company in advanced battery monitoring. in: INTELEC, Int. Telecommun. Energy Conf., pp. 646–653.

[19] Appelbaum J. & Weiss R., (1982) Electrical Model of the Lead-Acid Battery. in: INTELEC, Int. Telecommun. Energy Conf., pp. 304–307.

[20] Zhan C. J., Wu X. G., Kromlidis S., Ramachandaramurthy V. K., Barnes M., Jenkins N., et al., (2003) , "Two electrical models of the lead-acid battery used in a dynamic voltage restorer.", IEE Proceedings: Communications, 150 (2), 175–182.

[21] Salameh Z. M., Casacca M. A., & Lynch W. A., (1992) , "A mathematical model for lead-acid batteries.", IEEE Transactions on Energy Conversion, 7 (1), 93–98.

[22] Masoum M. A. S., Badejani S. M. M., & Fuchs E. F., (2004) , "Microprocessor-controlled new class of optimal battery chargers for photovoltaic applications.", IEEE Transactions on Energy Conversion, 19 (3), 599–606.

[23] Chen M. & Rincón-Mora G. A., (2006) , "Accurate electrical battery model capable of predicting runtime and I-V performance.", IEEE Transactions on Energy Conversion, 21 (2), 504–511.

[24] Tremblay O., Dessaint L. A., & Dekkiche A. I., (2007) A generic battery model for the dynamic simulation of hybrid electric vehicles. in: VPPC 2007 - Proc. 2007 IEEE Veh. Power Propuls. Conf., pp. 284–289.

[25] Tremblay O. & Dessaint L. A., (2009) , "Experimental validation of a battery dynamic model for EV applications.", 24th International Battery, Hybrid and Fuel Cell Electric Vehicle Symposium and Exhibition 2009, EVS 24, 2 930–939.

[26] Prieto R., Oliver J. A., Reglero I., & Cobos J. A., (2009) Generic battery model based on a parametric implementation. in: Conf. Proc. - IEEE Appl. Power Electron. Conf. Expo. - APEC, pp. 603–607.

[27] Alavi S. M. M., Birkl C. R., & Howey D. A., (2015) , "Time-domain fitting of battery electrochemical impedance models.", Journal of Power Sources, 288 345–352.

[28] Ho C., (1980) , "Application of A-C Techniques to the Study of Lithium Diffusion in Tungsten Trioxide Thin Films.", Journal of The Electrochemical Society, 127 (2), 343.

[29] Xia H., Lu L., & Ceder G., (2006) , "Li diffusion in LiCoO2 thin films prepared by pulsed laser deposition.", Journal of Power Sources, 159 (2), 1422–1427.

[30] Zhang S. S., Xu K., & Jow T. R., (2004) , "Electrochemical impedance study on the low temperature of Li-ion batteries.", Electrochimica Acta, 49 (7), 1057–1061.

[31] Zhang S. S., Xu K., & Jow T. R., (2006) , "EIS study on the formation of solid electrolyte interface in Li-ion battery.", Electrochimica Acta, 51 (8–9), 1636–1640.

[32] He B. L., Dong B., & Li H. L., (2007) , "Preparation and electrochemical properties of Ag-modified TiO2 nanotube anode material for lithium-ion battery.", Electrochemistry Communications, 9 (3), 425–430.

[33] Mirzaeian M. & Hall P. J., (2010) , "Characterizing capacity loss of lithium oxygen batteries by impedance spectroscopy.", Journal of Power Sources, 195 (19), 6817–6824.

[34] Zhang Y. & Wang C.-Y., (2009) , "Cycle-Life Characterization of Automotive Lithium-Ion Batteries with LiNiO[sub 2] Cathode.", Journal of The Electrochemical Society, 156 (7), A527.

[35] Piret H., Granjon P., Guillet N., & Cattin V., (2016) , "Tracking of electrochemical impedance of batteries.", Journal of Power Sources, 312 60–69.

[36] Wang L., Shinohara T., & Zhang B. P., (2012) , "Electrochemical behaviour of AZ61 magnesium alloy in dilute NaCl solutions.", Materials and Design, 33 (1), 345–349.

[37] Piao T., (1999) , "Intercalation of Lithium Ions into Graphite Electrodes Studied by AC Impedance Measurements.", Journal of The Electrochemical Society, 146 (8), 2794.

[38] Cheah Y. L., Gupta N., Pramana S. S., Aravindan V., Wee G., & Srinivasan M., (2011) , "Morphology, structure and electrochemical properties of single phase electrospun vanadium pentoxide nanofibers for lithium ion batteries.", Journal of Power Sources, 196 (15), 6465–6472.

[39] Levi M. D., Lu Z., & Aurbach D., (2001) , "Application of finite-diffusion models for the interpretation of chronoamperometric and electrochemical impedance responses of thin lithium insertion V2O5 electrodes.", Solid State Ionics, 143 (3–4), 309–318.

[40] Huang J. S., Yang L., Liu K. Y., & Tang Y. F., (2010) , "Synthesis and characterization of Li3V(2 - 2x/3)Mgx(PO4)3/C cathode material for lithium-ion batteries.", Journal of Power Sources, 195 (15), 5013–5018.

[41] Gao P., Li Y., Liu H., Pinto J., Jiang X., & Yang G., (2012) , " Improved High Rate Capacity and Lithium Diffusion Ability of LiNi 1/3 Co 1/3 Mn 1/3 O 2 with Ordered Crystal Structure .", Journal of The Electrochemical Society, 159 (4), A506–A513.

[42] Osaka T., Mukoyama D., & Nara H., (2015) , "Review—Development of Diagnostic Process for Commercially Available Batteries, Especially Lithium Ion Battery, by Electrochemical Impedance Spectroscopy.", Journal of The Electrochemical Society, 162 (14), A2529–A2537.

[43] Zhang H. & Chow M. Y., (2010) Comprehensive dynamic battery modeling for PHEV applications. in: IEEE PES Gen. Meet. PES 2010, pp. 1–6.

[44] Kleinsteinberg B., Klick S., & Sauer D. U., (2020) , "Empirical approach to determine open-circuit voltage of a vanadium-redox-flow battery for models, based on published data for anion-exchange and cation-exchange membranes and temperature dependency.", Journal of Energy Storage, 28 101109.

[45] Doyle M. & Newman J., (1995) , "The use of mathematical modeling in the design of lithium/polymer battery systems.", Electrochimica Acta, 40 (13–14), 2191–2196.

[46] Doyle M., (1993) , "Modeling of Galvanostatic Charge and Discharge of the Lithium/Polymer/Insertion Cell.", Journal of The Electrochemical Society, 140 (6), 1526.

[47] Newman J. S. & Tobias C. W., (1962) , "Theoretical Analysis of Current Distribution in Porous Electrodes.", Journal of The Electrochemical Society, 109 (12), 1183.

[48] De Vidts P., (1997) , "Governing Equations for Transport in Porous Electrodes.", Journal of The Electrochemical Society, 144 (4), 1343.

[49] Lai W. & Ciucci F., (2011) , "Mathematical modeling of porous battery electrodes-Revisit of Newman's model.", Electrochimica Acta, 56 (11), 4369–4377.

[50] Botte G. G., Subramanian V. R., & White R. E., (2000) , "Mathematical modeling of secondary lithium batteries.", Electrochimica Acta, 45 (15–16), 2595–2609.

[51] Ghalkhani M. & Mehrtash M., (2019) , "Modeling the Impedance Characterization of Prismatic Lithium-Ion Batteries.", Procedia Manufacturing, 32 762–767.

[52] Abraham D. P., Kawauchi S., & Dees D. W., (2008) , "Modeling the impedance versus voltage characteristics of LiNi0.8Co0.15Al0.05O2.", Electrochimica Acta, 53 (5), 2121–2129.

[53] Sluyters-Rehbach M., (1994) , "Impedances of electrochemical systems: Terminology, nomenclature and representation part I: Cells with metal electrodes and liquid solutions.", Pure and Applied Chemistry, 66 (9), 1831–1891.

[54] Xie Y., Li J., & Yuan C., (2014) , "Mathematical modeling of the electrochemical impedance spectroscopy in lithium ion battery cycling.", Electrochimica Acta, 127 266–275.

[55] Ogata K. & Hall P. P., (2004) , "System Dynamics Fourth Edition.",.

[56] Ghosh G., Locham K. K., Garg R., & Sarwal D., (2002) Clinical evaluation of acute respiratory distress and chest wheezing in infants: A few practical difficulties [4] (multiple letters). .

[57] Jeerage K. M., Noble R. D., & Koval C. A., (2007) Investigation of an aqueous lithium iodide/triiodide electrolyte for dual-chamber electrochemical actuators. .

[58] Westerhoff U., Kroker T., Kurbach K., & Kurrat M., (2016) , "Electrochemical impedance spectroscopy based estimation of the state of charge of lithium-ion batteries.", Journal of Energy Storage, 8 244–256.

[59] Fernández Pulido Y., Blanco C., Anseán D., García V. M., Ferrero F., & Valledor M., (2017) , "Determination of suitable parameters for battery analysis by Electrochemical Impedance Spectroscopy.", Measurement: Journal of the International Measurement Confederation, 106 1–11.

[60] Beelen H. P. G. J., Raijmakers L. H. J., Donkers M. C. F., Notten P. H. L., & Bergveld H. J., (2015) , "An improved impedance-based temperature estimation method for li-ion batteries.", IFAC-PapersOnLine, 28 (15), 383–388.

[61] Ovejas V. J. & Cuadras A., (2018) , "Impedance characterization of an LCO-NMC/graphite cell: Ohmic conduction, sei transport and charge-transfer phenomenon.", Batteries, 4 (3),.

[62] Momma T., Matsunaga M., Mukoyama D., & Osaka T., (2012) , "Ac impedance analysis of lithium ion battery under temperature control.", Journal of Power Sources, 216 304–307.

[63] Huet F., (1998) , "A review of impedance measurements for determination of the state-of-charge or state-of-health of secondary batteries.", Journal of Power Sources, 70 (1), 59–69.

[64] Samadani E., Farhad S., Scott W., Mastali M., Gimenez L. E., Fowler M., et al., (2015) , "Empirical modeling of lithium-ion batteries based on electrochemical impedance spectroscopy tests.", Electrochimica Acta, 160 169–177.

[65] Brown S., Mellgren N., Vynnycky M., & Lindbergh G., (2008) , "Impedance as a Tool for Investigating Aging in Lithium-Ion Porous Electrodes.", Journal of The Electrochemical Society, 155 (4), A320.

[66] Choi W., Shin H. C., Kim J. M., Choi J. Y., & Yoon W. S., (2020) , "Modeling and applications of electrochemical impedance spectroscopy (Eis) for lithium-ion batteries.", Journal of Electrochemical Science and Technology, 11 (1), 1–13.

[67] Oldenburger M., Bedürftig B., Gruhle A., Grimsmann F., Richter E., Findeisen R., et al., (2019) , "Investigation of the low frequency Warburg impedance of Li-ion cells by frequency domain measurements.", Journal of Energy Storage, 21 (June 2018), 272–280.

[68] Jossen A., (2006) , "Fundamentals of battery dynamics.", Journal of Power Sources, 154 (2), 530–538.

[69] Xu J., Mi C. C., Cao B., & Cao J., (2013) , "A new method to estimate the state of charge of lithium-ion batteries based on the battery impedance model.", Journal of Power Sources, 233 277–284.

[70] Kokam Co. L., (2017) , "Kokam Li-ion / Polymer Cell.", 1.

[71] Zhao Y., Patel Y., Hunt I. A., Kareh K. M., Holland A. A., Korte C., et al., (2017) , "Preventing lithium ion battery failure during high temperatures by externally applied compression.", Journal of Energy Storage, 13 296–303.

[72] Panchal S., Dincer I., Agelin-Chaab M., Fraser R., & Fowler M., (2016) , "Experimental temperature distributions in a prismatic lithium-ion battery at varying conditions.", International Communications in Heat and Mass Transfer, 71 35–43.

[73] Chiu K. C., Lin C. H., Yeh S. F., Lin Y. H., Huang C. S., & Chen K. C., (2014) , "Cycle life analysis of series connected lithium-ion batteries with temperature difference.", Journal of Power Sources, 263 75–84.

[74] Wang Z., Liu K., Liu J., Luo Q., & Ma C., (2017) , "Influence of the charging and discharging of the 18650 lithium-ion battery thermal runaway.", Journal of Loss Prevention in the Process Industries, (December 2016), 0–1.

[75] Kim G.-H., Smith K., Lee K.-J., Santhanagopalan S., & Pesaran A., (2011) , "Multi-Domain Modeling of Lithium-Ion Batteries Encompassing Multi-Physics in Varied Length Scales.", Journal of The Electrochemical Society, 158 (8), A955.

[76] Franco A. A., Rucci A., Brandell D., Frayret C., Gaberscek M., Jankowski P., et al., (2019) , "Boosting Rechargeable Batteries R&D by Multiscale Modeling: Myth or Reality?", Chemical Reviews, 119 (7), 4569–4627.

[77] Whitaker S., (2009) , "Derivation and application of the Stefan-Maxwell equations.", Revista Mexicana de Ingeniera Quimica, 8 (3), 213–243.

[78] Ecker M., Tran T. K. D., Dechent P., Käbitz S., Warnecke A., & Sauer D. U., (2015) , "Parameterization of a Physico-Chemical Model of a Lithium-Ion Battery.", Journal of The Electrochemical Society, 162 (9), A1836–A1848.

[79] Einstein A., (1905) , "Über die von der molekularkinetischen Theorie der Wärme geforderte Bewegung von in ruhenden Flüssigkeiten suspendierten Teilchen.", Annalen Der Physik, 322 (8), 549–560.

[80] Gill P. E., Murray W., & Saunders M. A., (2005) , "SNOPT: An SQP algorithm for large-scale constrained optimization.", SIAM Review, 47 (1), 99–131.

BIOGRAPHY

Ongun Bora SABAN was born in Bartın, August 15, 1993. After graduating from Zonguldak Atatürk Anatolian High School, started to study his bachelor's degree on mechanical engineering in Middle East Technical University Northern Cyprus Campus in 2011, then he had taken his graduation from Bartın University Mechanical Engineering Department in 2018. He has been working at Gebze Technical University Mechanical Engineering Department as a research assistant recently.

APPENDICES

Appendix A:

Kokam SLBP Small Cell Technology Specifications

Table A1: Kokam SLPB small cell technology specifications.

SLPB Small Cell

Type	Model	Capacity (Ah)	Dimension(mm)			AC-IR (mΩ)	Weight (g)	Discharge Rate C-rate(C)		Energy Density (Wh/kg)	Chemistry
			W	L	T			Continuous	Pulse		
3~5Ah	SLPB8043128H	3.2	43	128	7.8	5	84	20	40	141	HP NMC
	SLPB526495	3.3	64.5	95.5	5.4	15	67	2	3	182	HE NMC
	SLPB8643128H5	3.6	43	129	8.8	3	101	30	50	132	HP NMC
	SLPB11543140H5	5	43	142.5	11.7	3	132	30	50	140	HP NMC
	SLPB050106100	5	107	102	5.9	5	120	2	5	154	HE NMC
	SLPB50106100	5	107	102	5.9	5	140	5	8	151	HE NMC
5~10 Ah	SLPB776495	5.3	64.5	95.5	7.8	8	102	2	3	192	HE NMC
	SLPB75106100	7.5	107	102	7.9	4	165	5	8	173	HE NMC
	SLPB68106100	8	107	102	7.25	3.6	160	2	3	185	HE NMC
	SLPB7570180	9.6	82	183	7.6	3.5	215	2	3	165	HE NMC
10~20Ah	SLPB98106100	10	107	102	10	4	210	2	3	176	HE NMC
	SLPB55205130H	11	207	137	5.6	1.6	280	8	10	145	HP NMC
	SLPB7570270	15	82	272	7.7	2.5	317	2	3	175	HE NMC
	SLPB75106205	16	107	209	7.8	3.8	340	5	8	174	HE NMC
	SLPB78205130H	16	207	137	7.8	1.1	406	8	15	146	HP NMC

Kokam Battery Properties

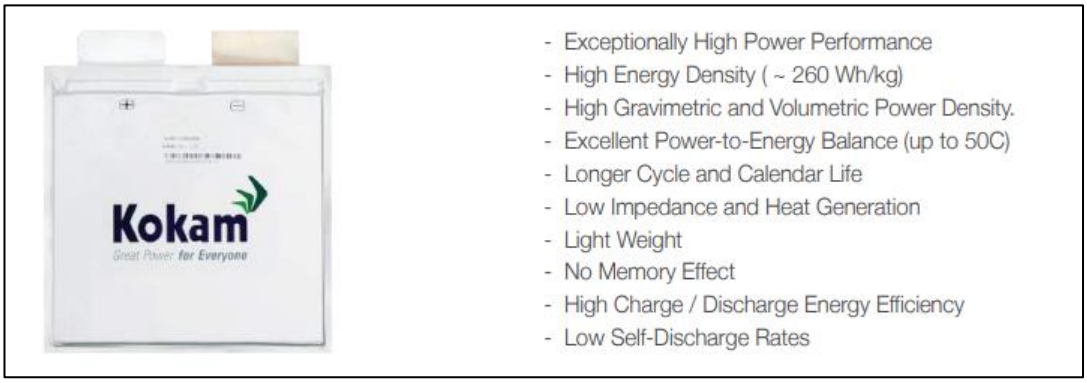

Figure A1: Kokam battery properties.

Appendix B:

Sensitivity Analysis Excel Sheet

	A	B	C	D	E	F	G	H	I	J	K	L	M	N	O	P	Q	R	S	T	U	V	W
1					Every 100 seconds electric potential vs time (V-t) data has taken.																		
2		Original		De	Forward Diff.		Ds_pos	Forward Diff.		Ds_neg	Forward Diff.		rp_pos	Forward Diff.		rp_neg	Forward Diff.		epsl_sep	Forward Diff.		epsl_pos	Forward Diff.
3	0	4,10290744	0	4,102907632	9,60996E 07	0	4,10290744	0	0	4,10290744	0	0	4,098979372	0,019640338	0	4,096073887	0,034167765	0	4,102945142	0,00018851	0	4,102220086	0,000859192
4	100	4,04164935	100	4,044860478	0,016055643	100	4,04164935	0	100	4,04164935	0	100	4,035759894	0,029447281	100	4,035001395	0,033239772	100	4,041775102	0,000628761	100	4,040177993	0,001839195
5	200	4,008851304	200	4,012272774	0,01710735	200	4,008851304	4,88498E 14	200	4,008851304	0	200	4,003053015	0,028991445	200	4,00225176	0,032997722	200	4,008980858	0,000647771	200	4,007853304	0,0012475
6	300	3,982092036	300	3,985750958	0,01829461	300	3,982092036	0	300	3,982092036	4,88498E 14	300	3,976410387	0,028408248	300	3,975619832	0,032361022	300	3,982221416	0,0006469	300	3,979021313	0,003838405
7	400	3,948793223	400	3,952584563	0,018956703	400	3,948793223	0	400	3,948793223	0	400	3,94310924	0,028419911	400	3,942459595	0,031668139	400	3,948922673	0,000647252	400	3,941838889	0,008692917
8	500	3,91116028	500	3,914827432	0,018335759	500	3,91116028	0	500	3,91116028	0	500	3,905305705	0,028272878	500	3,904795957	0,031821617	500	3,911290169	0,000649442	500	3,902667226	0,010616318
9	600	3,877652139	600	3,881086547	0,017172038	600	3,877652139	0	600	3,877652139	0	600	3,872066135	0,027930022	600	3,871176O1	0,032380646	600	3,877781972	0,000649162	600	3,873357032	0,005368884
10	700	3,851334821	700	3,854837748	0,017514632	700	3,851334821	0	700	3,851334821	0	700	3,845787981	0,027734202	700	3,844907O1	0,032139059	700	3,851464058	0,000646182	700	3,847621389	0,00464179
11	800	3,826891991	800	3,83050847	0,018082394	800	3,826891991	0	800	3,826891991	0	800	3,821359399	0,02766296	800	3,820538891	0,031765499	800	3,827021054	0,000645313	800	3,823078937	0,004766318
12	900	3,805283406	900	3,808795871	0,017562323	900	3,805283406	0	900	3,805283406	0	900	3,799796213	0,027435966	900	3,79871878	0,032823128	900	3,805412435	0,000645145	900	3,801723413	0,004449991
13	1000	3,785462328	1000	3,788993236	0,017654544	1000	3,785462328	0	1000	3,785462328	0	1000	3,780017892	0,02722218	1000	3,778991509	0,032354095	1000	3,785591231	0,000644518	1000	3,782305701	0,003945783
14	1100	3,767909309	1100	3,771414109	0,017524001	1100	3,767909309	0	1100	3,767909309	0	1100	3,762490373	0,027094679	1100	3,7614000B5	0,032546118	1100	3,768038106	0,000643987	1100	3,76506495	0,003555448
15	1200	3,751990861	1200	3,755352021	0,016805801	1200	3,751990861	0	1200	3,751990861	0	1200	3,746537167	0,027268472	1200	3,745519764	0,032355488	1200	3,752119567	0,000643527	1200	3,748943172	0,003809612
16	1300	3,73673277	1300	3,740271925	0,017695773	1300	3,73673277	0	1300	3,73673277	0	1300	3,73140387	0,026644502	1300	3,730416115	0,031583274	1300	3,736861353	0,000642915	1300	3,733620334	0,003890545
17	1400	3,722631032	1400	3,72614556	0,017572638	1400	3,722631032	0	1400	3,722631032	4,88498E 14	1400	3,717288007	0,026715124	1400	3,715991837	0,033195976	1400	3,722759336	0,00064152	1400	3,719715202	0,003644788
18	1500	3,710093002	1500	3,713424981	0,016659894	1500	3,710093002	4,88498E 14	1500	3,710093002	0	1500	3,704483404	0,028047987	1500	3,703801407	0,031457974	1500	3,710221991	0,000644949	1500	3,706974506	0,00389812
19	1600	3,69824897	1600	3,70198524	0,018681348	1600	3,69824897	0	1600	3,69824897	0	1600	3,692848568	0,027002012	1600	3,691955631	0,031466695	1600	3,698377891	0,000644607	1600	3,69472625	0,0044034
20	1700	3,686758127	1700	3,690596626	0,019192493	1700	3,686758127	0	1700	3,686758127	0	1700	3,681295661	0,027312328	1700	3,680571419	0,030933539	1700	3,686887288	0,000645805	1700	3,683011894	0,004682792
21	1800	3,677423673	1800	3,681344389	0,019603577	1800	3,677423673	0	1800	3,677423673	0	1800	3,671951778	0,027359476	1800	3,671382412	0,030206305	1800	3,677553229	0,000647781	1800	3,674244414	0,003974074
22	1900	3,670927459	1900	3,674815399	0,019439697	1900	3,670927459	0	1900	3,670927459	0	1900	3,665356494	0,027854826	1900	3,664723805	0,031018269	1900	3,671057519	0,000650301	1900	3,667885625	0,003802293
23	2000	3,664778103	2000	3,668853756	0,020378265	2000	3,664778103	0	2000	3,664778103	0	2000	3,659327953	0,027250751	2000	3,658397058	0,031905225	2000	3,664908514	0,000652052	2000	3,660952289	0,004782268
24	2100	3,65607386	2100	3,660056616	0,01991378	2100	3,65607386	0	2100	3,65607386	0	2100	3,650731357	0,026712514	2100	3,649420429	0,033267154	2100	3,656204031	0,000650855	2100	3,650832365	0,006551869
25	2200	3,644002556	2200	3,647852626	0,019250349	2200	3,644002556	5,10703E 14	2200	3,644002556	5,10703E 14	2200	3,638646449	0,026780535	2200	3,637153269	0,034246434	2200	3,644132428	0,000649359	2200	3,637838035	0,007705652
26	2300	3,630274766	2300	3,634519866	0,0212255	2300	3,630274766	0	2300	3,630274766	0	2300	3,624907182	0,026837921	2300	3,623450918	0,03411924	2300	3,630404741	0,000649877	2300	3,62397134	0,007879282
27	2400	3,614826735	2400	3,619231237	0,022022509	2400	3,614826735	0	2400	3,614826735	0	2400	3,609338286	0,027442244	2400	3,607949222	0,034387567	2400	3,614956605	0,000649352	2400	3,607206678	0,009525071
28	2500	3,596259805	2500	3,600810126	0,022751606	2500	3,596259805	0	2500	3,596259805	0	2500	3,590698946	0,027804294	2500	3,589254477	0,03502664	2500	3,596390753	0,000654743	2500	3,586606188	0,012067022
29	2600	3,572208284	2600	3,576677375	0,022345456	2600	3,572208284	4,88498E 14	2600	3,572208284	4,88498E 14	2600	3,56646636	0,028709618	2600	3,565086542	0,035608712	2600	3,572338364	0,000650401	2600	3,55888892	0,016649205
30	2700	3,540166261	2700	3,544585462	0,022096008	2700	3,540166261	0	2700	3,540166261	0	2700	3,534282604	0,029418283	2700	3,532869075	0,03648593	2700	3,540296472	0,000651057	2700	3,522723394	0,021803583
31	2800	3,500283803	2800	3,504240048	0,019781227	2800	3,500283803	5,10703E 14	2800	3,500283803	0	2800	3,494429204	0,029272995	2800	3,492833519	0,037251418	2800	3,500414105	0,000651511	2800	3,481374706	0,023636371
32	2900	3,461502679	2900	3,465288673	0,018929967	2900	3,461502679	0	2900	3,461502679	0	2900	3,455506533	0,029980733	2900	3,45385981	0,038214347	2900	3,461633097	0,000652091	2900	3,443581069	0,022402013
33	3000	3,425717944	3000	3,429255524	0,017687904	3000	3,425717944	5,10703E 14	3000	3,425717944	5,10703E 14	3000	3,419608379	0,030547824	3000	3,417846927	0,039355084	3000	3,425848066	0,00065061	3000	3,408900536	0,02102176
34	3100	3,392217235	3100	3,396289196	0,020359808	3100	3,392217235	9,99201E 14	3100	3,392217235	9,99201E 14	3100	3,385888982	0,031641262	3100	3,384159391	0,040289221	3100	3,39234536	0,000640627	3100	3,373164251	0,023816123
35	3200	3,352615775	3200	3,357303773	0,02343999	3200	3,352615775	9,99201E 14	3200	3,352615775	9,99201E 14	3200	3,346334748	0,031405139	3200	3,344397185	0,041092953	3200	3,352745339	0,000647818	3200	3,321666273	0,038686878
36	3300	3,285733388	3300	3,28992255	0,020945807	3300	3,285733388	9,99201E 14	3300	3,285733388	9,99201E 14	3300	3,2793112	0,032110941	3300	3,277152648	0,042903699	3300	3,285866575	0,000665933	3300	3,231680901	0,067565609
37	3400	3,176728052	3400	3,180782622	0,020272846	3400	3,176728052	4,88498E 14	3400	3,176728052	4,88498E 14	3400	3,170162292	0,032828804	3400	3,167756914	0,044855691	3400	3,176858935	0,000654412	3400	3,088418076	0,110387471
38	3500	3,011241101	3500	3,01508409	0,019214945	3500	3,011241101	6,99441E 13	3500	3,011241101	4,996E 13	3500	3,004400893	0,03420104	3500	3,00190396	0,046685704	3500	3,011354352	0,000566256	3500	2,843559549	0,20960194
39	3600	2,687322279	3600	2,691361594	0,020196577	3600	2,687322279	8,01581E 13	3600	2,687322279	1,70086E 12	3600	2,693778757	0,032282389	3600	2,699318652	0,059981864	3600	2,68746645	0,000720857	3600	2,687290933	3,91819E 05
40				ERROR	0,690724726		ERROR	2,14939E-12		ERROR	2,79776E-12		ERROR	1,051692123		ERROR	1,30815898		ERROR	0,02350216		ERROR	0,690048769

Figure B1.1: Sensitivity analysis calculation.

	X	Y	Z	AA	AB	AC	AD	AE	AF	AG	AH	AI	AJ	AK	AL	AM	AN	AO	AP	AQ	AR	AS	AT	AU	AV	AW	AX
1																											
2		epsl_neg	Forward Diff.		Inactive_pos	Forward Diff.		Inactive_neg	Forward Diff.		utilization	Forward Diff.		Csei	Forward Diff.		Ks_pos	Forward Diff.		Ks_neg	Forward Diff.		k_neg	Forward Diff.		k_pos	Forward Diff.
3	0	4,102609117	0,001491612	0	4,101969471	0,004689845	0	4,102554327	0,001765564	0	4,130694502	0,013893531	0	4,102879009	0,000142153	0	4,102908	4,98094E 07	0	4,10291	3,29946E 06	0	4,10362092	0,071348505	0	4,1032493	0,028489535
4	100	4,04257724	0,00463945	100	4,039555062	0,010471436	100	4,042057304	0,002039771	100	4,071903151	0,015126901	100	4,041481864	0,000837427	100	4,041649	5,0871E 07	100	4,04165	3,58775E 06	100	4,04234217	0,06928253	100	4,0421442	0,041236595
5	200	4,009333568	0,002411321	200	4,007070367	0,008904682	200	4,008836522	7,39071E 05	200	4,034463076	0,012805886	200	4,008811041	0,000201317	200	4,008851	5,01867E 07	200	4,00885	3,61721E 06	200	4,00953882	0,06875149	200	4,0093467	0,041281869
6	300	3,982810834	0,003593987	300	3,977930334	0,02080851	300	3,982350534	0,001292488	300	4,003709443	0,010808703	300	3,981847803	0,001221167	300	3,982092	4,73404E 07	300	3,98209	3,3638E 06	300	3,98276177	0,066973554	300	3,9825896	0,041461685
7	400	3,951892859	0,015498184	400	3,940520987	0,041361176	400	3,950963872	0,010853246	400	3,976165459	0,013686118	400	3,948131565	0,00330829	400	3,948793	4,76377E 07	400	3,94879	2,95747E 06	400	3,94944546	0,065223899	400	3,9493061	0,042743206
8	500	3,916719776	0,027797476	500	3,901366693	0,048967937	500	3,915116776	0,019782475	500	3,94135475	0,015097235	500	3,910207596	0,004763424	500	3,91116	4,8957E 07	500	3,91116	2,95036E 06	500	3,91181778	0,06574978	500	3,9116765	0,043020053
9	600	3,882058069	0,022029651	600	3,872471657	0,025902411	600	3,880591005	0,014694329	600	3,904535671	0,013441766	600	3,871163788	0,002441755	600	3,877652	4,82988E 07	600	3,87765	3,83049E 06	600	3,87832816	0,067602221	600	3,8781227	0,039215428
10	700	3,852520097	0,005926375	700	3,846697595	0,023186131	700	3,851856006	0,002605924	700	3,872552785	0,010608982	700	3,85114034	0,000972405	700	3,851335	4,8047E 07	700	3,85134	3,58036E 06	700	3,85200229	0,066747268	700	3,8517934	0,038218197
11	800	3,82791539	0,005116994	800	3,822269117	0,02311437	800	3,827303041	0,002055251	800	3,846605988	0,009856999	800	3,826743553	0,00074219	800	3,826892	4,89501E 07	800	3,82689	3,49472E 06	800	3,8275529	0,066091283	800	3,8273607	0,039061187
12	900	3,806106276	0,004114348	900	3,800729975	0,022767156	900	3,805533559	0,001250767	900	3,822679076	0,008697835	900	3,805137257	0,000730743	900	3,805284	4,87901E 07	900	3,80528	3,69445E 06	900	3,80595632	0,067291833	900	3,8057713	0,040657575
13	1000	3,786001888	0,002697801	1000	3,781450997	0,020056652	1000	3,785511661	0,000246669	1000	3,801588895	0,008063284	1000	3,785420317	0,000210052	1000	3,785462	4,86973E 07	1000	3,78546	3,79188E 06	1000	3,78613472	0,067239395	1000	3,7859405	0,039851426
14	1100	3,767761815	0,000737467	1100	3,764279279	0,018150148	1100	3,767494195	0,002075567	1100	3,782060358	0,007075525	1100	3,767849732	0,000297883	1100	3,767909	4,87841E 07	1100	3,76791	3,27745E 06	1100	3,76857344	0,066412904	1100	3,7683181	0,03406223
15	1200	3,751868892	0,000609845	1200	3,748155315	0,019177733	1200	3,751576322	0,002072694	1200	3,764878207	0,006443673	1200	3,75200157	5,35467E 05	1200	3,751991	4,88156E 07	1200	3,75199	3,32769E 06	1200	3,7526584	0,066753602	1200	3,75241	0,034928115
16	1300	3,736904171	0,000857006	1300	3,732720057	0,020063563	1300	3,736554074	0,000893482	1300	3,749134961	0,006201096	1300	3,736694123	0,000193236	1300	3,736733	4,89103E 07	1300	3,73673	3,76067E 06	1300	3,73740516	0,06723882	1300	3,7372266	0,044435864
17	1400	3,722612658	9,18679E 05	1400	3,718743227	0,019439026	1400	3,722360813	0,001351096	1400	3,734019478	0,005694223	1400	3,722433077	0,000989776	1400	3,722631	5,03998E 07	1400	3,72263	4,724E 06	1400	3,72330258	0,067154835	1400	3,7230769	0,03715277
18	1500	3,710373064	0,001400312	1500	3,706144473	0,019742646	1500	3,709635485	0,002287582	1500	3,720317783	0,005112391	1500	3,710069241	0,000118802	1500	3,710093	4,93362E 07	1500	3,71009	2,19499E 06	1500	3,71074377	0,065076701	1500	3,7102997	0,01722343
19	1600	3,698694754	0,002228919	1600	3,693932503	0,021582336	1600	3,69820817	0,000204	1600	3,70755884	0,004654935	1600	3,698103338	0,000728158	1600	3,698249	4,94728E 07	1600	3,69825	2,87022E 06	1600	3,69889406	0,064509246	1600	3,6986998	0,037571306
20	1700	3,687647731	0,004448017	1700	3,682301988	0,022280695	1700	3,686946517	0,000941949	1700	3,696021371	0,004631622	1700	3,686547135	0,00105496	1700	3,686758	5,31738E 07	1700	3,68676	2,04742E 06	1700	3,68738723	0,062910723	1700	3,6872043	0,037181812
21	1800	3,678675432	0,006258796	1800	3,673568789	0,019274422	1800	3,677879861	0,002280938	1800	3,684713843	0,003645085	1800	3,677057492	0,001830908	1800	3,677424	7,623E 07	1800	3,67742	2,5978E 06	1800	3,67804045	0,061677974	1800	3,6779894	0,047142397
22	1900	3,672314866	0,006937034	1900	3,667126057	0,019007013	1900	3,671446502	0,002595216	1900	3,676150346	0,002611443	1900	3,670536129	0,00195665	1900	3,670928	6,46178E 07	1900	3,67093	1,88767E 06	1900	3,67156164	0,063417599	1900	3,6714163	0,040739344
23	2000	3,666314581	0,007682388	2000	3,6599987	0,023897015	2000	3,665453055	0,003374759	2000	3,669796055	0,002508976	2000	3,664300943	0,002385804	2000	3,664778	6,62701E 07	2000	3,66478	2,18954E 06	2000	3,66543148	0,065338074	2000	3,6652219	0,036979307
24	2100	3,657887947	0,009070433	2100	3,649639496	0,03217182	2100	3,657064972	0,00495556	2100	3,663381555	0,003653847	2100	3,655477717	0,002980716	2100	3,656074	4,04652E 07	2100	3,65607	2,71653E 06	2100	3,65676372	0,068986191	2100	3,6565257	0,037650503
25	2200	3,645881208	0,009393259	2200	3,636613759	0,036943986	2200	3,645073166	0,005353051	2200	3,654059496	0,00502847	2200	3,643304275	0,003491404	2200	3,644003	2,61239E 07	2200	3,644	3,49324E 06	2200	3,64471878	0,071622277	2200	3,6444436	0,036752891
26	2300	3,631745333	0,007352834	2300	3,622628581	0,038230927	2300	3,630976963	0,003510983	2300	3,641465372	0,005595303	2300	3,629706529	0,002841188	2300	3,630275	3,75322E 07	2300	3,63028	3,00164E 06	2300	3,63098703	0,071226366	2300	3,6307361	0,038443938
27	2400	3,616212567	0,006929159	2400	3,605725799	0,045504681	2400	3,615406926	0,002900956	2400	3,627623365	0,006398315	2400	3,614235186	0,002957747	2400	3,614827	1,37592E 07	2400	3,61483	1,9908E 06	2400	3,61554807	0,072133874	2400	3,6153011	0,039529067
28	2500	3,59763918	0,006896878	2500	3,584864131	0,05697837	2500	3,596863623	0,00301909	2500	3,61160496	0,007672577	2500	3,595646993	0,003064061	2500	3,59626	1,07815E 06	2500	3,59626	3,71168E 06	2500	3,59699388	0,073407696	2500	3,5967633	0,041960822
29	2600	3,573707684	0,007497001	2600	3,556837763	0,076852604	2600	3,57290138	0,00346548	2600	3,592320085	0,010055901	2600	3,571489459	0,003594126	2600	3,572208	9,1781E 07	2600	3,57221	1,2265E 06	2600	3,57295836	0,075007508	2600	3,5727295	0,043432482
30	2700	3,541529876	0,006818077	2700	3,520374275	0,098959931	2700	3,54073958	0,002866595	2700	3,566852313	0,013343026	2700	3,539373039	0,003966107	2700	3,540166	6,73822E 07	2700	3,54017	1,33076E 06	2700	3,54092908	0,07628217	2700	3,5406452	0,039910826
31	2800	3,501675874	0,006960354	2800	3,479110318	0,105867425	2800	3,50088431	0,0030002534	2800	3,533302887	0,016509542	2800	3,499380583	0,004516097	2800	3,500284	3,92929E 07	2800	3,50028	2,56222E 06	2800	3,50106661	0,078280731	2800	3,5007805	0,041388959
32	2900	3,462812033	0,00654677	2900	3,441417511	0,100425839	2900	3,462069313	0,002833167	2900	3,492750883	0,015624102	2900	3,460519436	0,004916216	2900	3,461503	5,20957E 07	2900	3,4615	2,99955E 06	2900	3,46230889	0,080621089	2900	3,4620081	0,042114551
33	3000	3,426688094	0,00485075	3000	3,406775328	0,094713078	3000	3,426089802	0,001859293	3000	3,454609127	0,014445592	3000	3,424763705	0,004771194	3000	3,425718	4,70572E 07	3000	3,42572	3,27623E 06	3000	3,42655008	0,083214121	3000	3,4262261	0,042346878
34	3100	3,393205725	0,004942449	3100	3,370592212	0,108125114	3100	3,392468022	0,001253936	3100	3,419414157	0,013598461	3100	3,391033863	0,005916857	3100	3,392217	2,52123E 06	3100	3,39222	1,81926E 06	3100	3,39305877	0,084153556	3100	3,3926699	0,037720384
35	3200	3,354542191	0,009632078	3200	3,317426631	0,17594572	3200	3,353397899	0,0039106618	3200	3,385657623	0,016520924	3200	3,350358805	0,01128485	3200	3,352615	1,490556 06	3200	3,35262	1,76931E 06	3200	3,35347992	0,086414611	3200	3,3532344	0,05154926
36	3300	3,289119667	0,016931392	3300	3,225456541	0,301384235	3300	3,287806182	0,010363971	3300	3,34333566	0,028801136	3300	3,28028514	0,027241238	3300	3,285734	2,91512E 06	3300	3,28573	5,89401E 06	3300	3,28664533	0,091193864	3300	3,2862495	0,043007828
37	3400	3,180824642	0,02048295	3400	3,078926846	0,489006033	3400	3,179437538	0,013547429	3400	3,269172119	0,046222033	3400	3,166989245	0,048694037	3400	3,176728	3,93024E 07	3400	3,17673	1,48025E 06	3400	3,17768073	0,095267645	3400	3,1773554	0,052279502
38	3500	3,014337165	0,015480321	3500	2,807517987	1,018615566	3500	3,013505503	0,011322011	3500	3,150102453	0,069430676	3500	2,996641876	0,072996123	3500	3,011236	2,48183E 05	3500	3,01123	3,43565E 05	3500	3,01219718	0,095607654	3500	3,0114368	0,016311112
39	3600	2,686878877	0,002217009	3600	2,686966211	0,001780341	3600	2,683817954	0,017521622	3600	2,973127326	0,142902523	3600	2,68890308	0,007904008	3600	2,687326	2,02836E 05	3600	2,68733	3,14938E 05	3600	2,68841771	0,109543495	3600	2,6877691	0,037238663
40		ERROR	0,268570566		ERROR	3,234350574		ERROR	0,166423971		ERROR	0,596468637		ERROR	0,236316614		ERROR	6,85908E-05		ERROR	0,000170168		ERROR	2,705755087		ERROR	1,444290994

Figure B1.1: Sensitivity analysis calculation. (Continue)

	AY	AZ	BA	BB	BC	BD	BE	BF	BG	BH	BI	BJ	BK	BL	BM	BN	BO	BP	BQ	BR	BS	BT	BU	BV	BW	BX	BY	BZ	CA	CB
1																														
2	aA_pos		Forward Diff.	aA_neg		Forward Diff.	aC_pos		Forward Diff.	aC_neg		Forward Diff.	cdlvol_cs_pos		Forward Diff.	cdl_pos		Forward Diff.	Rfilm_neg		Forward Diff.	R_curr		Forward Diff.	cl_0		Forward Diff.	tor_pos		Forward Diff.
3	0	4,101271	0,008180481	0	4,0998635	0,015219601	0	4,1010959	0,009057947	0	4,0993	0,018187643	0	4,10301861	0,000555871	0	4,10291	6,251E 10	0	4,102906313	5,63323E 06	0	4,10290744	0	0	4,102905	1,21868E 05	0	4,1027338	0,000868212
4	100	4,039182	0,012335765	100	4,0387373	0,014560404	100	4,0390655	0,012919366	100	4,0381	0,01770366	100	4,04165032	4,85965E 06	100	4,04165	2,99494E 11	100	4,041648193	5,7817E 06	100	4,04164935	0	100	4,0417488	0,000497383	100	4,0410966	0,002763504
5	200	4,006448	0,012016384	200	4,0059777	0,014367888	200	4,0063585	0,012464145	200	4,0053	0,017622945	200	4,00885071	2,96378E 06	200	4,00885	1,94249E 10	200	4,008850144	5,80125E 06	200	4,0088513	0	200	4,0089536	0,000511708	200	4,0082607	0,002953134
6	300	3,979742	0,01174919	300	3,9792843	0,014038851	300	3,9796701	0,012109727	300	3,9786	0,017246257	300	3,98207857	6,73136E 05	300	3,98209	1,72795E 09	300	3,982090912	5,62447E 06	300	3,98209204	0	300	3,9822005	0,000542257	300	3,9814255	0,003332585
7	400	3,946397	0,011980876	400	3,9460585	0,013673646	400	3,9463424	0,012254125	400	3,9454	0,016868364	400	3,94879177	7,25168E 06	400	3,94879	4,50251E 10	400	3,94879214	5,41492E 06	400	3,94879322	0	400	3,9489009	0,000538317	400	3,9481801	0,003065381
8	500	3,908789	0,011858893	500	3,9084296	0,013653518	500	3,9087529	0,012036845	500	3,9078	0,017021303	500	3,91115949	3,95803E 06	500	3,91116	3,0955E 10	500	3,911159176	5,52476E 06	500	3,91116028	0	500	3,9112665	0,000531099	500	3,9105506	0,003048546
9	600	3,875313	0,01169804	600	3,8748166	0,014177878	600	3,8752941	0,011790365	600	3,8741	0,017925333	600	3,8776535	6,80072E 06	600	3,87765	2,84994E 11	600	3,877650982	5,78648E 06	600	3,87765214	0	600	3,8777589	0,000533899	600	3,8770267	0,003127392
10	700	3,849011	0,011620406	700	3,8486169	0,01358941	700	3,8490093	0,011627757	700	3,8479	0,017383636	700	3,85133621	6,96306E 06	700	3,85133	5,4512E 12	700	3,851333672	5,7461E 06	700	3,85133482	0	700	3,8514401	0,000526348	700	3,8507105	0,003121844
11	800	3,824576	0,011582275	800	3,8242436	0,013241729	800	3,8245914	0,011503156	800	3,8235	0,017101285	800	3,82689367	8,40811E 06	800	3,82689	2,77001E 11	800	3,826890857	5,66965E 06	800	3,82689199	0	800	3,8269955	0,000517479	800	3,8262814	0,003053204
12	900	3,802979	0,011521803	900	3,8026055	0,013389673	900	3,8030117	0,011358289	900	3,8018	0,017521996	900	3,80528494	7,65275E 06	900	3,80528	5,79981E 12	900	3,80528224	5,82791E 06	900	3,80528341	0	900	3,805387	0,000517902	900	3,8046686	0,003073794
13	1000	3,783167	0,011475931	1000	3,7828064	0,013279493	1000	3,783216	0,011231579	1000	3,7819	0,017571777	1000	3,78546319	4,29192E 06	1000	3,78546	3,20988E 11	1000	3,785461157	5,8514E 06	1000	3,78546233	0	1000	3,7855651	0,000513613	1000	3,7848477	0,003073335
14	1100	3,765616	0,011466259	1100	3,7652747	0,013172954	1100	3,7656815	0,011139173	1100	3,7644	0,017517003	1100	3,76790889	2,11441E 06	1100	3,76791	1,39149E 10	1100	3,767908156	5,76496E 06	1100	3,76790931	0	1100	3,7680111	0,000508974	1100	3,7672962	0,003065786
15	1200	3,749698	0,011462276	1200	3,7493279	0,013314585	1200	3,7497809	0,011049865	1200	3,7484	0,017854843	1200	3,75199068	9,23627E 07	1200	3,75199	1,219E 10	1200	3,751989705	5,78184E 06	1200	3,75199086	0	1200	3,7520924	0,000507755	1200	3,7513789	0,003059618
16	1300	3,734442	0,011455795	1300	3,7341959	0,012684505	1300	3,7345415	0,010956585	1300	3,7333	0,01739606	1300	3,73673528	1,25576E 05	1300	3,73673	8,71503E 11	1300	3,73673161	5,79792E 06	1300	3,73673277	0	1300	3,7368343	0,000507884	1300	3,7361229	0,003049444
17	1400	3,720351	0,011402456	1400	3,7198959	0,013675816	1400	3,7204677	0,010816512	1400	3,7189	0,018620129	1400	3,72264392	6,44253E 05	1400	3,72263	1,1187E 09	1400	3,722629893	5,69736E 06	1400	3,72263103	4,884988E 14	1400	3,722731	0,000500025	1400	3,7220434	0,002938143
18	1500	3,707767	0,011631006	1500	3,7074309	0,013310509	1500	3,7079023	0,010953367	1500	3,7065	0,017996838	1500	3,71008463	4,18687E 05	1500	3,71009	8,88749E 10	1500	3,710091901	5,50462E 06	1500	3,710093	0	1500	3,7101925	0,000497487	1500	3,7094903	0,003013325
19	1600	3,695928	0,011604511	1600	3,6957376	0,012556991	1600	3,6960825	0,010832538	1600	3,6948	0,017434823	1600	3,69825051	7,67517E 06	1600	3,69825	9,37006E 11	1600	3,698247905	5,32703E 06	1600	3,69824897	0	1600	3,6983493	0,0005017	1600	3,6976525	0,002982571
20	1700	3,684409	0,011745516	1700	3,6843359	0,012111117	1700	3,684584	0,010870836	1700	3,6834	0,016939409	1700	3,68675626	9,32974E 06	1700	3,68676	7,15544E 08	1700	3,686757103	5,12075E 06	1700	3,68675813	0	1700	3,6868511	0,000464936	1700	3,6862225	0,002678232
21	1800	3,675021	0,012014514	1800	3,6749828	0,012204455	1800	3,6752216	0,011010441	1800	3,6741	0,016707516	1800	3,67743062	3,47244E 05	1800	3,67742	5,17114E 06	1800	3,677422532	5,70361E 06	1800	3,67742367	0	1800	3,6775094	0,000428554	1800	3,6769653	0,00229162
22	1900	3,668505	0,012111262	1900	3,6684768	0,012253346	1900	3,6687352	0,010961491	1900	3,6675	0,017347571	1900	3,67092914	8,41981E 06	1900	3,67093	1,54632E 06	1900	3,670926391	5,33874E 06	1900	3,67092746	0	1900	3,6710159	0,000442282	1900	3,6704383	0,002445857
23	2000	3,662376	0,012009994	2000	3,6622254	0,012763579	2000	3,6626149	0,0108159	2000	3,6611	0,018263115	2000	3,66478096	1,42698E 05	2000	3,66478	4,80413E 06	2000	3,664776903	6,00296E 06	2000	3,6647781	0	2000	3,6648845	0,000532014	2000	3,6641523	0,003128786
24	2100	3,653728	0,011730205	2100	3,6534463	0,013137914	2100	3,6539834	0,010452085	2100	3,6522	0,01912754	2100	3,65607509	6,13736E 06	2100	3,65607	8,84849E 07	2100	3,656072769	5,45286E 06	2100	3,65607386	0	2100	3,6561916	0,00058886	2100	3,6553479	0,003630019
25	2200	3,641614	0,011943701	2200	3,6413063	0,013481137	2200	3,6418796	0,010614608	2200	3,64	0,020162668	2200	3,64400277	1,0629E 06	2200	3,644	3,26926E 06	2200	3,644001542	5,07031E 06	2200	3,64400256	5,10703E 14	2200	3,644124	0,000607254	2200	3,6432427	0,003799218
26	2300	3,627869	0,012031133	2300	3,6276194	0,013276791	2300	3,6281675	0,01053638	2300	3,6263	0,020092915	2300	3,63027639	8,12308E 06	2300	3,63027	6,49356E 08	2300	3,630273364	5,62846E 06	2300	3,63027477	0	2300	3,630401	0,000631122	2300	3,6294708	0,004020015
27	2400	3,612339	0,012440279	2400	3,6121486	0,013390519	2400	3,6126601	0,010833236	2400	3,6107	0,020392951	2400	3,61482609	3,23817E 06	2400	3,61483	1,20523E 05	2400	3,61482605	3,4225E 06	2400	3,61482673	0	2400	3,6149549	0,000641064	2400	3,6139952	0,004157839
28	2500	3,593698	0,012810351	2500	3,5935538	0,013530044	2500	3,594092	0,010839071	2500	3,5921	0,020971935	2500	3,59626435	2,2713E 05	2500	3,59626	2,15584E 05	2500	3,596258004	9,00609E 06	2500	3,5962598	0	2500	3,5963999	0,000700453	2500	3,5953615	0,004491375
29	2600	3,569595	0,01306738	2600	3,5695273	0,013404793	2600	3,5699781	0,01115078	2600	3,5679	0,021728432	2600	3,57220731	4,86565E 06	2600	3,57222	4,33615E 05	2600	3,572208324	2,01279E 07	2600	3,57220828	9,99201E 14	2600	3,5723434	0,000675654	2600	3,5713558	0,004262513
30	2700	3,537418	0,013740656	2700	3,5374324	0,013669387	2700	3,5378643	0,011509701	2700	3,5357	0,022469469	2700	3,54016622	2,05448E 07	2700	3,54017	1,80659E 05	2700	3,540166599	1,35365E 06	2700	3,54016626	4,884988E 14	2700	3,5402947	0,000642383	2700	3,5393311	0,00417576
31	2800	3,497527	0,013785099	2800	3,4975124	0,013857157	2800	3,4980013	0,011412575	2800	3,4957	0,023134784	2800	3,50028726	1,72652E 05	2800	3,50028	1,55925E 06	2800	3,500282739	5,32129E 06	2800	3,5002838	5,10703E 14	2800	3,500386	0,000511006	2800	3,4996237	0,003300557
32	2900	3,458638	0,014321952	2900	3,4586869	0,014079002	2900	3,4591683	0,011672042	2900	3,4567	0,024134752	2900	3,46150622	1,77E 05	2900	3,4615	1,47658E 06	2900	3,461501519	5,80139E 06	2900	3,46150268	4,884988E 14	2900	3,4616175	0,000574114	2900	3,460874	0,003143186
33	3000	3,422769	0,014746781	3000	3,4228614	0,014282521	3000	3,4233407	0,011886401	3000	3,4206	0,025342025	3000	3,4257212	1,6294E 05	3000	3,42572	5,53864E 07	3000	3,42571684	5,51717E 06	3000	3,42571794	5,10703E 14	3000	3,4258253	0,000536978	3000	3,425071	0,003234677
34	3100	3,389105	0,015563131	3100	3,3894086	0,014043073	3100	3,3897338	0,012417302	3100	3,387	0,026303082	3100	3,39221269	2,2711E 05	3100	3,39223	8,07125E 05	3100	3,392218793	7,79282E 06	3100	3,39221723	1,5099E 13	3100	3,3922115	2,84515E 05	3100	3,3914488	0,003842215
35	3200	3,349499	0,015582221	3200	3,34984	0,013879063	3200	3,3501206	0,012475945	3200	3,3472	0,02700905	3200	3,35261572	2,67481E 07	3200	3,35263	8,99852E 05	3200	3,352616845	5,34796E 06	3200	3,35261578	1,9984E 13	3200	3,352819	0,001016255	3200	3,3520278	0,002940044
36	3300	3,282392	0,016707989	3300	3,2828184	0,014574785	3300	3,283185	0,012741907	3300	3,2799	0,029037278	3300	3,28574186	4,23451E 05	3300	3,2857	0,000145606	3300	3,285730689	1,34965E 05	3300	3,28573339	9,992001E 14	3300	3,2859686	0,001176186	3300	3,2851905	0,002714309
37	3400	3,173296	0,017161144	3400	3,1739509	0,013885848	3400	3,1741266	0,013007335	3400	3,1705	0,031367507	3400	3,17673013	1,03762E 05	3400	3,17672	2,18853E 05	3400	3,17672986	9,03775E 06	3400	3,17672805	1,4877E 13	3400	3,1769514	0,001116903	3400	3,1761894	0,002693439
38	3500	3,007637	0,018019902	3500	3,0085488	0,013461477	3500	3,0081037	0,015687027	3500	3,0045	0,033944167	3500	3,01116049	0,00040303	3500	3,01118	0,000307904	3500	3,011280578	0,000197386	3500	3,0112411	1,449995E 12	3500	3,0113795	0,000692177	3500	3,0105643	0,003384026
39	3600	2,683862	0,017300022	3600	2,6828243	0,022489679	3600	2,6827526	0,022848265	3600	2,6987	0,057100127	3600	2,68737421	0,000259637	3600	2,67533	0,059940697	3600	2,680083665	0,036193072	3600	2,68732228	1,70086E 12	3600	2,6795332	0,03894547	3600	2,6738596	0,067313354
40		ERROR	0,47387558		ERROR	0,50968314		ERROR	0,437844668		ERROR	0,790550187		ERROR	0,001708614		ERROR	0,060701235		ERROR	0,036591609		ERROR	4,15001E-12		ERROR	0,059218134		ERROR	0,18123686
41																														

Figure B1.1: Sensitivity analysis calculation. (Continue)

CC	CD	CE	CF	CG	CH	CI	CJ	CK
tor_neg		Forward Diff.	*tor_sep*		Forward Diff.	*lonc*		Forward Diff.
0	4,1027073	0,001000865	0	4,1028809	0,000132562	0	4,103085844	0,000892021
100	4,0410879	0,002807196	100	4,0415638	0,000427602	100	4,041817522	0,000840861
200	4,0082576	0,002968753	200	4,0087628	0,000442517	200	4,009020029	0,000843623
300	3,9814145	0,00338752	300	3,9820037	0,000441723	300	3,982274958	0,000914609
400	3,948095	0,003490866	400	3,948705	0,000441203	400	3,948986041	0,000964094
500	3,9104871	0,003365914	500	3,9110719	0,000441843	500	3,911344407	0,000920634
600	3,8770848	0,002836537	600	3,8775635	0,000443304	600	3,877818276	0,000830683
700	3,8507284	0,003031959	700	3,8512464	0,000441896	700	3,851508919	0,000870488
800	3,8262729	0,003095608	800	3,8268038	0,000440965	800	3,8270686	0,000883045
900	3,8047236	0,002799265	900	3,8051952	0,000440888	900	3,805449602	0,000830979
1000	3,7848907	0,002858201	1000	3,7853741	0,000441082	1000	3,78563002	0,000838465
1100	3,7672842	0,003125304	1100	3,7678211	0,000440825	1100	3,768085595	0,000881431
1200	3,7513749	0,00307998	1200	3,7519028	0,000440374	1200	3,752165171	0,000871549
1300	3,7361711	0,002808547	1300	3,7366448	0,000439999	1300	3,736902497	0,000848635
1400	3,722086	0,00272515	1400	3,7225432	0,000439145	1400	3,722790527	0,000797474
1500	3,709293	0,004000001	1500	3,7100048	0,000441032	1500	3,710289343	0,000981704
1600	3,6974908	0,003790951	1600	3,6981609	0,000440548	1600	3,698444828	0,00097929
1700	3,6858621	0,004480175	1700	3,68667	0,00044063	1700	3,686966597	0,001042351
1800	3,676552	0,004358166	1800	3,6773355	0,000440642	1800	3,677630167	0,001032469
1900	3,6700161	0,004557024	1900	3,6708393	0,000440965	1900	3,67113489	0,001037156
2000	3,6639272	0,004254295	2000	3,6646898	0,000441617	2000	3,664991179	0,001065378
2100	3,6553625	0,003556792	2100	3,6559856	0,000441216	2100	3,65627421	0,001001748
2200	3,6433879	0,003073445	2200	3,6439143	0,000441167	2200	3,644190168	0,000938061
2300	3,629527	0,003738693	2300	3,6301863	0,000442225	2300	3,630489397	0,001073155
2400	3,6140528	0,00386981	2400	3,6147384	0,000441893	2400	3,615046548	0,001099068
2500	3,5954672	0,003963272	2500	3,5961708	0,000445007	2500	3,596490391	0,001152932
2600	3,5715195	0,003443697	2600	3,5721198	0,000442443	2600	3,572423299	0,001075076
2700	3,5393894	0,003884158	2700	3,5400777	0,000442858	2700	3,540380939	0,001073389
2800	3,4994982	0,003928211	2800	3,5001954	0,000441858	2800	3,500481571	0,000988839
2900	3,4607961	0,00353278	2900	3,4614144	0,000441583	2900	3,461702589	0,00099955
3000	3,4250487	0,00334601	3000	3,4256298	0,000440795	3000	3,425900121	0,000910888
3100	3,3911489	0,005341912	3100	3,3921303	0,000434648	3100	3,392337249	0,000600073
3200	3,3516074	0,005041837	3200	3,3525287	0,000435397	3200	3,352970254	0,001772393
3300	3,2850135	0,00359937	3300	3,285644	0,000446784	3300	3,286072309	0,001694602
3400	3,1760429	0,003425669	3400	3,1766398	0,000441087	3400	3,177045627	0,001587874
3500	3,010371	0,004350702	3500	3,0111617	0,000396942	3500	3,011467741	0,0011332
3600	2,6807943	0,032640122	3600	2,6872254	0,000484309	3600	2,687693269	0,001854949
	ERROR	0,159558759		ERROR	0,016001575		ERROR	0,038122735

Figure B1.1: Sensitivity analysis calculation. (Continue)

$$Forward\ Difference = \frac{f(x+h) - f(x)}{h}$$

The most sensitive parameters	Value
inactive_pos	3,234350574
k_pos	2,705755087
k_neg	1,444290994
rp_neg	1,30815898
rp_pos	1,051692123

Figure B1.2: Sensitivity analysis results.